BILINGUAL PUBLISHING GROUP

Journal of Atmospheric Science Research

Volume 6 • Issue 2 • April 2023 ISSN 2630-5119(Online)

BILINGUAL PUBLISHING GROUP

Editor-in-Chief

Dr. Qiang Zhang
Beijing Normal University, China

Dr. José Francisco Oliveira Júnior
Federal University of Alagoas (UFAL), Maceió, Alagoas, Brazil

Dr. Jianhui Bai
Institute of Atmospheric Physics, Chinese Academy of Sciences, China

Editorial Board Members

Alexander Kokhanovsky, Germany
Fan Ping, China
Svetlana Vasilivna Budnik, Ukraine
S. M. Robaa, Egypt
Daniel Andrade Schuch, Brazil
Nicolay Nikolayevich Zavalishin, Russian Federation
Isidro A. Pérez, Spain
Lucille Joanna Borlaza, France
Che Abd Rahim Bin Mohamed, Malaysia
Mengqian Lu, China
Sheikh Nawaz Ali, India
ShenMing Fu, China
Nathaniel Emeka Urama, Nigeria
Thi Hien To, Vietnam
Prabodha Kumar Pradhan, India
Tianxing Wang, China
Zhengqiang Li, China
Haider Abbas Khwaja, United States
Kuang Yu Chang, United States
Wen Zhou, China
Mohamed El-Amine Slimani, Algeria
Xiaodong Tang, China
Perihan Kurt-Karakus, Turkey
Anning Huang, China
Olusegun Folarin Jonah, United States
Pallav Purohit, Austria
Pardeep Pall, Canada
Service Opare, Canada
Donglian Sun, United States
Jian Peng, United Kingdom
Vladislav Vladimirovich Demyanov, Russian Federation
Chuanfeng Zhao, China
Jingsong Li, China
Suleiman Alsweiss, United States
Ranis Nail Ibragimov, United States
Raj Kamal Singh, United States
Lei Zhong, China
Chenghai Wang, China
Lichuan Wu, Sweden
Naveen Shahi, South Africa
Hassan Hashemi, Iran
David Onojiede Edokpa, Nigeria
Maheswaran Rathinasamy, India
Zhen Li, United Kingdom
Anjani Kumar, India
Netrananda Sahu, India
Aisulu Tursunova, Kazakhstan
Hirdan Katarina de Medeiros Costa, Brazil
Masoud Rostami, Germany
Barbara Małgorzata Sensuła, Poland

Volume 6 Issue 2 • April 2023 • ISSN 2630-5119 (Online)

Journal of Atmospheric Science Research

Editor-in-Chief

Dr. Qiang Zhang
Dr. José Francisco Oliveira Júnior
Dr. Jianhui Bai

BILINGUAL PUBLISHING GROUP

BILINGUAL PUBLISHING GROUP

Volume 6 | Issue 2 | April 2023 | Page1-82

Journal of Atmospheric Science Research

Contents

Articles

1 **Wavelet Analysis of Average Monthly Temperature New Delhi 1931-2021 and Forecast until 2110**
Peter Mazurkin

21 **Investigating the Effects of Madden-Julian Oscillation on Climate Elements of Iran (1980-2020)**
Kourosh Mohammadpour, Zahra Hejazizadeh, Hooshang Ghaemi, Mohammad Salighe

33 **Crucial, But not Systematically Investigated: Rock Glaciers, the Concealed Water Reservoirs of the Himalayas: An Opinion**
Sheikh Nawaz Ali, Pratima Pandey

42 **The Possibilities of Using the Minimax Method to Diagnose the State of the Atmosphere**
Elena S. Andreeva

50 **Rainfall and Temperature Variations in a Dry Tropical Environment of Nigeria**
David O. Edokpa, Precious N. Ede, Bridget E. Diagi, Susan I. Ajiere

58 **Formation and Transport of a Saharan Dust Plume in Early Summer**
Habib Senghor, Abdou L. Dieng, Moussa Gueye, Cheikh A. Diop, Mariane D. Kane, Amadou T. Gaye

75 **Co-designed Practical Use of Probabilistic Climate Advisories among Smallholder Farmers: A Balance between Confidence and Caution**
Mary Mwangi, Evans Kituyi, Gilbert Ouma

BILINGUAL PUBLISHING GROUP

Journal of Atmospheric Science Research
https://journals.bilpubgroup.com/index.php/jasr

ARTICLE

Wavelet Analysis of Average Monthly Temperature New Delhi 1931-2021 and Forecast until 2110

Peter Mazurkin

Volga State University of Technology, Yoshkar-Ola, the Republic of Mari El, 424000, Russia

ABSTRACT

The identification method in the CurveExpert-1.40 software environment revealed asymmetric wavelets of changes in the average monthly temperature of New Delhi from 1931 to 2021. The maximum increment for 80 years of the average monthly temperature of 5.1 °C was in March 2010. An analysis of the wave patterns of the dynamics of the average monthly temperature up to 2110 was carried out. For forecasting, formulas were adopted containing four components, among which the second component is the critical heat wave of India. The first component is the Mandelbrot law (in physics). It shows the natural trend of decreasing temperature. The second component increases according to the critical law. The third component with a correlation coefficient of 0.9522 has an annual fluctuation cycle. The fourth component with a semi-annual cycle shows the influence of vegetation cover. The warming level of 2010 will repeat again in 2035-2040. From 2040 the temperature will rise steadily. June is the hottest month. At the same time, the maximum temperature of 35.1 °C in 2010 in June will again reach by 2076. But according to the second component of the heat wave, the temperature will rise from 0.54 °C to 16.29 °C. The annual and semi-annual cycles had an insignificant effect on the June temperature dynamics. Thus, the identification method on the example of meteorological observations in New Delhi made it possible to obtain summary models containing a different number of components. The temperature at a height of 2 m is insufficient. On the surface, according to space measurements, the temperature reaches 55 °C. As a result, in order to identify more accurate asymmetric wavelets for forecasting, the results of satellite measurements of the surface temperature of India at various geographical locations of meteorological stations are additionally required.

Keywords: New Delhi; Average monthly temperature; Waves of behavior; 1931-2021; Sum of wavelets; Verification; Forecasts up to 2110

*CORRESPONDING AUTHOR:
Peter Matveevich Mazurkin, Volga State University of Technology, Yoshkar-Ola, the Republic of Mari El, 424000, Russia; Email: kaf_po@mail.ru

ARTICLE INFO
Received: 31 January 2023 | Revised: 20 February 2023 | Accepted: 22 February 2023 | Published Online: 28 February 2023
DOI: https://doi.org/10.30564/jasr.v6i2.5447

CITATION
Mazurkin, P., 2023. Wavelet Analysis of Average Monthly Temperature New Delhi 1931-2021 and Forecast until 2110. Journal of Atmospheric Science Research. 6(2): 1-20. DOI: https://doi.org/10.30564/jasr.v6i2.5447

COPYRIGHT
Copyright © 2023 by the author(s). Published by Bilingual Publishing Group. This is an open access article under the Creative Commons Attribution-NonCommercial 4.0 International (CC BY-NC 4.0) License. (https://creativecommons.org/licenses/by-nc/4.0/).

1. Introduction

Our opinion is that we don't understand much about climate dynamics. Contradictory climatic processes of warming or cooling occur at different points on the earth's landmass. In India, for example, due to the strong influence of the Himalayas and monsoons from the Indian Ocean, global warming is indeed observed.

There is only one reason for this—for 4000 years of the evolution of Indian civilization, rich natural forests and large swamps have completely disappeared.

The farmers of India have always been at war with the forests. They had to win land plots in the forests for crops [1]. Based on descriptive statistics from a large number of statistical samples, Kumar et al. [2] clearly conclude that deforestation is the main cause of global warming and climate change. The problem of climate change is difficult to fight because it is too late to do anything. Our opinion is that we don't understand much about climate dynamics.

By 2050, parts of India and Pakistan are predicted to experience heat waves with a probability exceeding 60% per year. The seriousness of the problem is so great, notes the Times of India (March 9), that it is proposed to consider the organization of mass "climate migration" as one of the measures.

The Indian Meteorological Department (IMD) writes in its annual report on the country's climate that 2021 was not only the fifth warmest year since 1901. But in the last decade, that is, in the period 2012-2021, it was also the warmest on record. In addition, 11 of the 15 warmest years on record were between 2007 and 2021. Rising average temperatures in India may have an increasing cascading effect on extreme weather events [3].

Abnormally high temperatures due to heat waves can be fatal to humans and animals. Temperatures are rising across India, with a trend toward a decrease in the frequency of cold waves [4].

The climate of India due to the relief is very diverse. Four types of it are distinguished on the territory: Dry tropical, humid tropical, subequatorial monsoon and high mountain. In the north, the Himalayas fence off the cold Asian winds, and in the northwest, a significant territory is occupied by the Thar Desert, which attracts warm, humid monsoons. Monsoons determine the characteristics of the climate throughout India [5].

Time series of global or regional surface air temperatures are important for climate change studies [6]. At the same time, the sun heats the earth's surface unevenly. The equator receives more heat, the poles of the planet are smaller. As a result, the temperature gradient is one of the main forces that drive the ocean and the atmosphere of the planet. In the tropics, the climate system receives energy, and in temperate and polar latitudes it gives it away [7].

The energy of solar radiation absorbed by the earth's surface, as well as the thermal radiation of the earth's surface itself from the inside, is ejected into space through the atmospheric transparency window, the ejection depends on variations in the area of cloud cover. However [8], an increase in the area of cloud cover in the lower layers of the atmosphere will simultaneously lead to both a decrease and an increase in temperature. Because of this, the energy balance of the earth before and after an increase in the area of cloudiness by 2% will remain almost at a zero level.

To understand long-term climate fluctuations, Bhargawa and Singh [3] analyzed data over a period of 40 years (1978-2018) on 10 climatic parameters that affect climate dynamics. The results showed that the strongest global climate change occurred by the end of 2018 compared to natural variability in the late 1970s.

According to Slama [10], global warming is still considered to be related to the cause of CO_2 emissions. Directly and at the same time instantly affecting the heating of the surrounding air is the heat released by fossil fuels. Anthropogenic heat is estimated at 17415 1010 kWh/year; this heat causes an increase in temperature by an average of 0.122 °C per year, or 12.2 °C per century.

In the article [11] Ullah et al. note that mountain ecosystems are considered sensitive indicators of global warming; even small variations in tempera-

ture can lead to significant shifts in the local climate. The main causes are greenhouse gases and deforestation. Appropriate policies are needed to conserve forests, wildlife, prevent hunting, control pollution, increase plantations, awareness, control regional climate change, etc.

The purpose of the article is to identify asymmetric wavelets of the average monthly temperature in New Delhi from 1931 to 2021 by the identification method [8-12], then analyze the wave patterns of the climate and make tentative forecasts of the average monthly temperature until 2110.

2. Materials and methods

The assumption of M. Milankovich about the constancy of the albedo of the earth's surface during the interglacial periods was replaced in the article [18]. The new hypothesis assumes that anomalies in the mean annual temperature of the surface layer of the atmosphere are associated with interannual changes in the planetary albedo and thermal inertia of the earth's hydrosphere. In another article [18], Zavalishin considered two hypotheses of modern warming on the planet: natural and anthropogenic. The work proved that the hypothesis of natural warming is much more probable than the hypothesis of warming due to anthropogenic influence. At the same time, it was shown that the displacement of the sun from the center of mass of the solar system directly affects the temperature of the surface atmosphere in various synoptic regions of Eurasia.

We will not rush to identify causal relationships in warming in India according to the New Delhi weather station, but we will show stable patterns that are revealed in the dynamics of the average monthly temperature for 1931-2021.

A series of average monthly surface temperatures according to the New Delhi meteorological station was taken from the site http://www.pogodaiklimat.ru/history/42182.htm (Accessed 22.04.2022).

Table 1 gives a fragment of average monthly temperatures in New Delhi from the initial data array for identifying asymmetric wavelets.

January 1, 1931 ($\tau = 0$) is taken as the beginning of the time reference (years) according to the dynamic series of average monthly temperatures. For each month of the year, its specific time is taken according to the expression (Year 1931) + month / 12. Here, the calculation of the month is taken as follows: January = 1; February = 2 etc. Then, from January 1931 to December 2021, the time has passed in 91 years, in connection with this, the indicative forecast can be made for the forecast horizon equal to the basis of the forecast according to the weather station, that is, until 2021 + 91 = 2112. Our calculations were performed until 2110.

Table 1 gives a fragment from the data array of the New Delhi meteorological station of the average monthly temperature of the surface air layer at a height of 2 m. In this complete table, there are 91 × 12 = 1092 values of the average monthly temperature without gaps. Then the representativeness of the dynamic series is 100%.

Table 2 compares the warmest monthly average temperature in 91 years in 2010 with the start of registration at the New Delhi weather station in 1931 (**Figure 1**), as well as the latest 2021 with the same start.

Warming in descending order of average monthly temperature occurred in March (5.1), February (3.5), April (3.0), November (2.2), October (1.6), and May (1.6). Cooling compared to 1931 occurred in August (–0.2), July and September (–0.3), December (–0.5), June (–0.6) and January (–1.7). If the difference in average monthly temperatures in 1931 was equal to 35.1 – 15.2 = 19.9 °C, then in 2010 it became equal to 34.7 – 13.7 = 21.0 °C. At the same time, the maximum shifted from June 1931 to May 2010.

However, in 2021, the maximum average monthly temperature returned again, as in 1931, to the month of June. As can be seen from the data in **Table 2**, in 2010 the temperature maximum shifted to May. At the same time, the difference in the average monthly temperature in June 2021, compared to January, became equal to 32.4 – 12.9 = 19.5 °C. Such a drop in 1931 was equal to 35.1 – 15.4 = 19.7 °C. At the same time, in March, the temperature increase in 2010 occurred by 5.1 °C compared to 1931, and in 2021 this difference decreased to 3.8 °C.

Table 1. Average monthly air temperature data (°C) in New Delhi for 1931-2021.

Year	January		…	July		…	December	
	Time τ	Temper. t		Time τ	Temper. t		Time τ	Temper. t
1931	0.083	15.4	…	0.583	31.7	…	1	15.5
1932	1.083	15.6	…	1.583	31.7	…	2	14.7
1933	2.083	12.3	…	2.583	29.4	…	3	15.8
…	…	…	…	…	…	…	…	…
2019	88.083	14.1	…	88.583	32.0	…	89	13.2
2020	89.083	13.7	…	89.583	31.5	…	90	15.2
2021	90.083	12.9	…	90.583	31.5	…	91	14.5

Table 2. Average monthly temperatures in New Delhi.

Month	1931	2010	Δt, °C	1931	2021	Δt, °C
Jan	15.4	13.7	–1.7	15.4	12.9	–2.5
Feb	15.2	18.7	3.5	15.2	18.6	3.4
Mar	21.2	26.3	5.1	21.2	25.0	3.8
Apr	29.7	32.7	3.0	29.7	28.6	–1.1
May	33.1	34.7	1.6	33.1	30.4	–2.7
Jun	35.1	34.5	–0.6	35.1	32.4	–2.7
Jul	31.7	31.4	–0.3	31.7	31.5	–0.2
Aug	30.3	30.1	–0.2	30.3	30.9	0.6
Sep	28.6	28.3	–0.3	28.6	29.0	0.4
Oct	25.3	26.9	1.6	25.3	26.0	0.7
Nov	19.1	21.3	2.2	19.1	18.8	–0.3
Dec	15.5	15	–0.5	15.5	14.5	–1.0

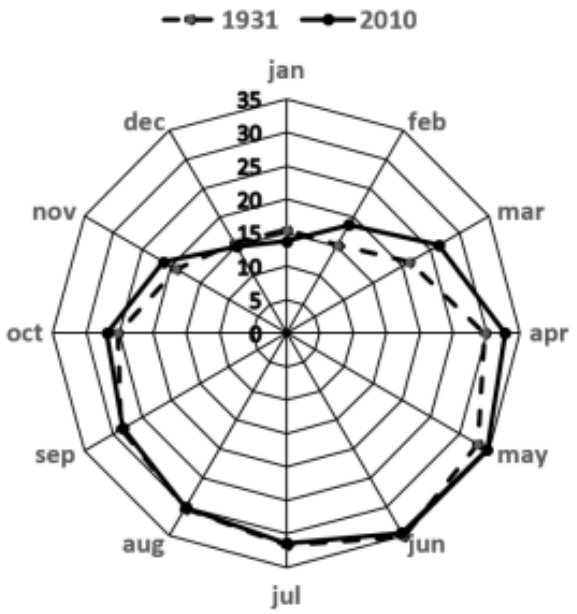

Figure 1. Charts of average monthly temperatures in New Delhi.

From the data of **Table 2** and **Figure 1**, it can be seen that the temperature increment sharply decreased in May (from 1.6 to –2.7 °C). Thus, the average monthly temperature clearly shows the oscillatory perturbation of the regional climate. Other meteorological parameters also influence the process of oscillatory climate adaptation to the local geophysical conditions of New Delhi.

The maximum increment for 80 years of average monthly temperature in New Delhi at 5.1 °C was in March 2010 (**Figure 2**).

As can be seen from **Figure 2**, the 2021 average monthly temperature increment chart is inside the 2010 increment chart. Only August and September increased their increment by 2021 compared to 2010. Then it turns out that, in comparison with the data on the average annual temperature [12], the changes in the average monthly temperature are more informative.

Oscillations (the so-called asymmetric wavelet signals), as the sum of the quanta of the behavior of

the surface air layer at a height of 2 m at the New Delhi weather station, in the general case, are written by the formula [12-16] of the general form of oscillatory adaptation.

$$y = \sum_{i=1}^{m} y_i \text{ , } y_i = A_i \cos(\pi x / p_i - a_{8i}) \text{ , } \quad A_i = a_{1i} x^{a_{2i}} \exp(-a_{3i} x^{a_{4i}}) \text{ , } \quad p_i = a_{5i} + a_{6i} x^{a_{7i}} \tag{1}$$

where y is the dependent factor, i is the number of the (1), m is the number of a component in the (1), x is the influencing factor, $a_1 ... a_8$ are the parameters of the model (1) that take numerical values during structural and parametric identification program environment CurveExpert-1.40 (URL: http://www.curveexpert.net/) according to statistical data, A_i is the amplitude (half) of the wavelet (axis y), p_i is the half-period of oscillation (axis x).

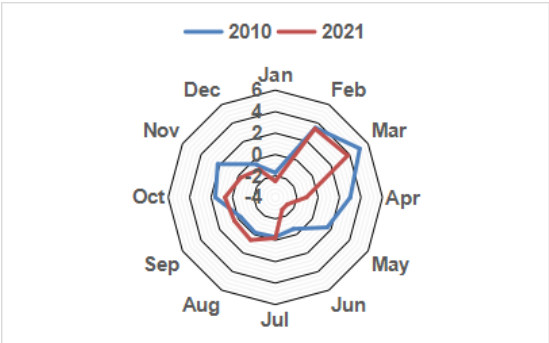

Figure 2. Diagram of monthly average temperature increments in New Delhi.

According to formula (1) with two ***fundamental physical constants*** e (the Napier number or the number of time) and π (the Archimedes number or the number of space), a series of ***quantized wavelet signals*** is formed. In our example, these are the behavioral quanta of the mean monthly temperature. The concept of a wavelet allows one to abstract from the physical meaning of statistical series and consider their additive decomposition into components (behavior quanta). The general equation is obtained as a sum of wavelets.

A signal is a material carrier of information. And we understand information as a ***measure of interaction***. A signal can be generated, but it is not required to receive it. A signal can be any physical process or part of it. It turns out that the change in the set of unknown signals has long been known, for example, through a series of measurements (**Table 1**). However, there are still no models of the distributions of the average annual temperature in dynamics and the influence of the geographical coordinates of city centers on temperature change.

The amplitude $y = A$ at $a_2 = 0$ and $a_4 = 1$ turns into the Laplace law (in mathematics), Mandelbrot (in physics), Zipf-Pearl (in biology) and Pareto (in econometrics). A trend is formed when the oscillation period a_5i tends to infinity. Most often, the trend is formed from two members of the formula (1).

3. Results and discussion

The time series of mean annual [8] and mean monthly temperatures at the New Delhi meteorological station from 1931 to 2021 turned out to be relatively complex in their changes. But at the same time, these series are more informative in comparison with other cities in Europe and Asia for understanding regional climate changes.

The first scenario of conditional forecasting for future orientation up to 2110 was carried out according to the model (1) containing four components. Then, with additional asymmetric infinite-dimensional wavelets, model (1) included the sum of 12 components. The third scenario contained 16 more wavelets for 91 mean monthly temperature values for August. At the same time, in the third scenario of the tentative forecast for the future, a total of 28 components of model (1) was revealed.

The average monthly temperature is a physical quantity that is a measure of the monthly average kinetic energy of the translational movement of molecules, in our case, air molecules in the surface layer at a height of 2 m above the land surface at the New Delhi weather station. Therefore, the average monthly temperature is a continuous physical quantity, the initial series of values of which should not be subjected to transformations. However, averaging over a month is quite acceptable due to the influence of the moon's circulation around our planet on the earth's climate. But at the same time, groupings by time intervals for the artificial summing up of numerical data under linear models are

categorically unacceptable.

The linear method is universal in all four quadrants of the rectangular coordinate system. Therefore, in the identification method, the linear formula is used as the beginning of the modeling process in the CurveExpert-1.40 software environment to identify a non-linear trend. In its final form, the trend contains clearly non-linear formulas, and wavelets cannot be obtained from linear equations at all.

3.1 Wavelets of New Delhi monthly average temperature dynamics

Features of CurveExpert-1.40 software environment

The method of identifying the sum of asymmetric wavelets (1) was carried out sequentially by the residuals from the previous pattern, that is, as the previous stable pattern is revealed, the point residuals on the graph already show the possibility of continuing the identification process.

At the same time, the arithmetic mean of the average monthly temperature in New Delhi for 91 years and 12 months, equal to 25.14 °C, was taken at the beginning of the simulation. The standard deviation of this arithmetic mean is 6.7593 °C. In this case, the correlation coefficient as a measure of adequacy is equal to 0.

Then a two-term trend was revealed (**Figure 3**), containing two regularities. The first component is the Mandelbrot law (in physics) $y = a\exp(-bx)$ of the exponential decrease in the mean monthly temperature. The same law is known in mathematics as the Laplace law, in biology-Zipf-Pearl, in econometrics-Pareto. This exponential formula shows the natural trend from 1931 to 2021 of a slow decrease in the average monthly temperature. Such a natural reason for the decline is the cosmic cold that endlessly surrounds the planet Earth. Therefore, with any oscillatory perturbations of the global climate in the earth's atmosphere, the planet will eventually cool down in billions of years.

The second and subsequent components of the general model (1) show changes in the average monthly temperature depending on planetary, including regional, primarily anthropogenic influences. As is known [17,18], the variability of natural warming due to the influence of the sun is more probable in comparison with the anthropogenic impact.

Therefore, the second component of the trend for New Delhi for 91 years increases according to the power mathematical function $y = ax^b$. But it turned out that the influence of the Himalayas gives an increase in the average monthly temperature even according to the law of "double" growth according to the formula of the anomalous biotechnical [12-16] law of prof. P.M. Mazurkin $y = ax^b \exp(cx^d)$. Here, the negative sign of the activity of inhibition of the increase in the parameter received a positive value $\pm c$, therefore, the product of two laws of growth was formed-power law and according to the modified Mandelbrot law under the condition $d \neq 1$. Then the trend has grown over time and it is necessary to take geo-technological measures to eliminate the second, and even the first, component of the trend.

The trend is always a special case of an asymmetric wavelet (1) provided that the half-period of oscillations is many times greater than the measurement time interval, in our case 91 years.

The correlation coefficient of the two-component trend is only 0.0198, which seems to be very negligible in terms of the level of adequacy. But it turned out that even with 28 components of the dynamics, the influence of the second component of the trend is the most significant.

The first wobble, with a correlation coefficient of 0.9522, is an infinite-dimensional wavelet, meaning it starts much earlier than 1931 and will continue well beyond 2021. This infinity is provided by the amplitude, which decreases with time according to the Mandelbrot law. Therefore, a distinctive feature of the annual cyclicity is the continuous decrease in the amplitude of fluctuations, which will favorably affect the regional climate of India.

The second oscillation with a semi-annual cycle is typical not only for air temperature, but also for the concentrations of various greenhouse gases, especially for CO_2. For carbon dioxide, it was assumed that the cycles of half a year are influenced by the vegetation cover of both hemispheres of the earth.

Apparently, the vegetation cover (grass + shrubs + trees) of India for 4000 years has been severely depleted by people for the needs of agriculture.

The second wavelet with a correlation coefficient of 0.8203, which is much higher than the strong coupling level of 0.7, has an increasing amplitude according to our modified Mandelbrot law of exponential growth.

All these four components were identified together in the CurveExpert-1.40 software environment.

Four components of the general mathematical regularity

According to the computational capabilities of the CurveExpert-1.40 software environment, the main of which is the list of identifiers alphabetically in the English language by the first 19 letters, **Table 3** shows the parameters of the model (1) with five significant digits, and **Figure 4** shows a graph of the general pattern.

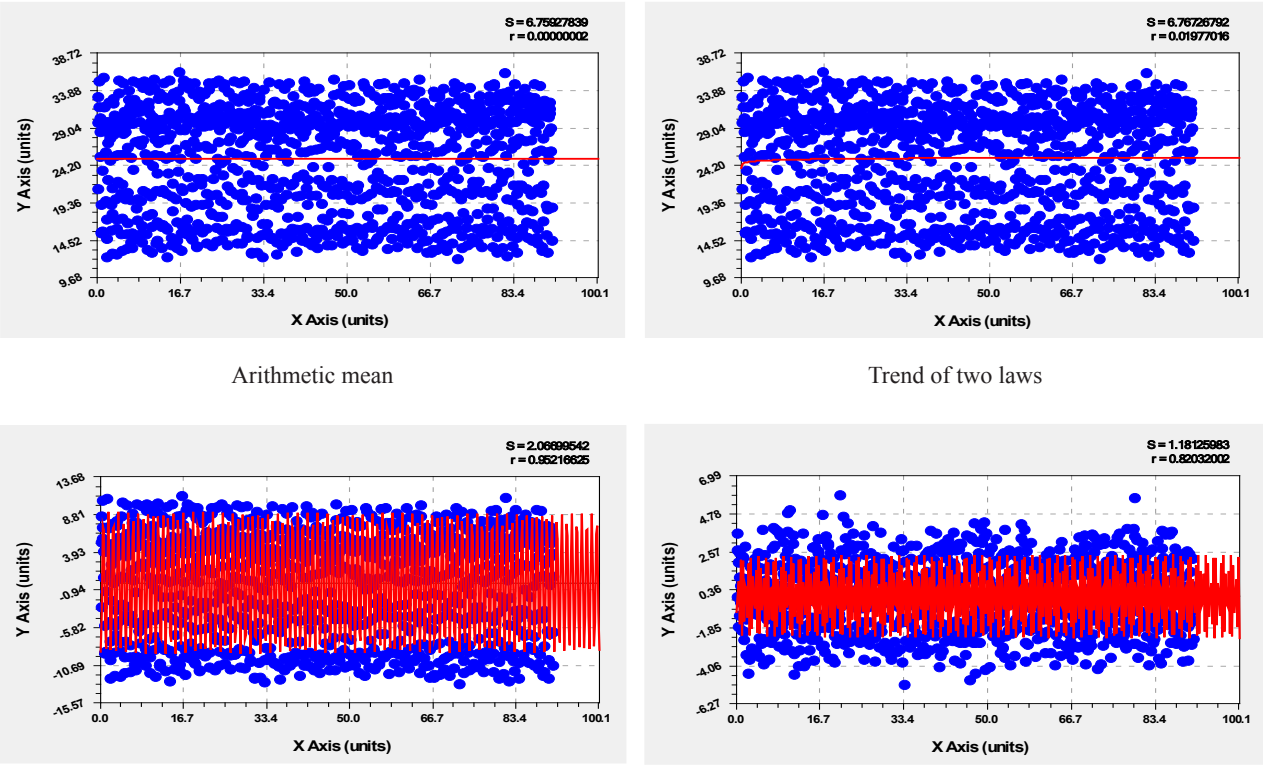

Arithmetic mean

Trend of two laws

Oscillation with a period of an annual cycle

Fluctuation with a period of a semi-annual cycle

Figure 3. Dynamics of the average monthly temperature in New Delhi for 1931-2021 according to the computational capabilities in the CurveExpert-1.40 software environment (in the upper right corner: S standard deviation; r correlation coefficient).

Table 3. Dynamics of average monthly temperatures in New Delhi for 1931-2021.

i	**Asymmetric wavelet** $y_i = a_{1i}x^{a_{2i}}\exp(-a_{3i}x^{a_{4i}})\cos(\pi x(a_{5i}+a_{6i}x^{a_{7i}})-a_{8i})$								Coef. correl. r
	Amplitude (half) oscillation				Half cycle oscillation			Shift	
	a_{1i}	a_{2i}	a_{3i}	a_{4i}	a_{5i}	a_{6i}	a_{7i}	a_{8i}	
1	23.99317	0	0.0031983	1	0	0	0	0	0.9847
2	0.70194	0.38093	–0.014504	0.84550	0	0	0	0	
3	–9.20090	0	0.00025230	1	0.5	0	0	0.33219	
4	1.18494	0	–0.65220	0.021793	0.25	0	0	4.37689	

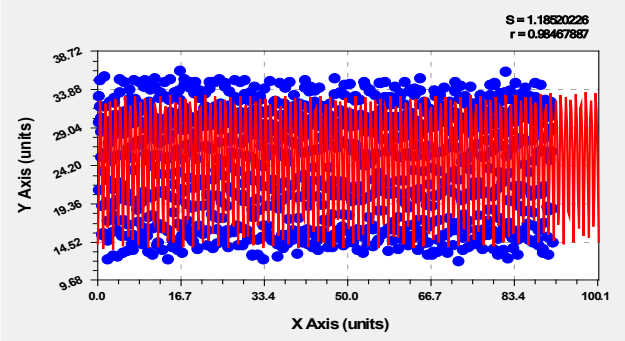

Figure 4. Graph of the general mathematical regularity of the four components of the average monthly temperature in New Delhi for 1931-2021.

The correlation coefficient of 0.9847 relates a composite pattern of four components in terms of the level of adequacy to a super strong (0.95 or more) factorial relationship. The other wave components of the model (1) will sequentially appear on the residuals, so the level of adequacy will increase.

The exponential growth activity for the fourth component of the pattern is 0.65220, which is a very high value. However, the rate of temperature increase at the New Delhi meteorological station is very small and amounts to only 0.021793. Such parameters of the law of growth are still encouraging that experts will find ways to reduce the average monthly temperature in the future.

Distribution of the relative error of the four-component model

The number of points n (pieces) distributed in intervals of 1 °C of the relative error [Δ] (°C) of the model (1) with the parameters from **Table 3** is given in **Table 4**. The relative error varies from +22 to –23%, which is within the margin of error of ± 30% acceptable for environmental studies.

Then the error changes according to the Gauss law (**Figure 5**) with additions in the form of four wavelets in the form of a five-term equation.

$$n = n_1 + n_2 + n_3 + n_4 + n_5 \quad (2)$$

$$n_1 = 81.19311\exp(-0.017123([\Delta]+0.054267)^2),$$

$$n_2 = A_1\cos(\pi([\Delta]+30)/p_1 + 0.31110),$$

$$A_1 = -4.17162\cdot 10^{-128}([\Delta]+30)^{99.98851}\exp(-0.012693([\Delta]+30)^{2.38818}),$$

$$p_1 = 2.15178,$$

$$n_3 = A_2\cos(\pi([\Delta]+30)/p_2 - 2.95272),$$

$$A_2 = -5.30474\cdot 10^{-86}([\Delta]+30)^{85.67795}\exp(-2.91956([\Delta]+30)^{1.01269}),$$

$$p_2 = 0.81791 + 0.0090604([\Delta]+30)^{1.01094},$$

$$n_4 = A_3\cos(\pi([\Delta]+30)/p_3 - 0.39260),$$

$$A_3 = 3.03395\cdot 10^{-26}([\Delta]+30)^{23.90826}\exp(-0.57596([\Delta]+30)^{1.048237}),$$

$$p_3 = 3.90251 + 0.00011685([\Delta]+30)^{2.23048},$$

$$n_5 = A_4\cos(\pi([\Delta]+30)/p_4 - 0.43605),$$

$$A_4 = 3.62160\cdot 10^{-9}([\Delta]+30)^{7.36654}\exp(-0.0021021([\Delta]+30)^{2.20851}),$$

$$p_4 = 0.063641 + 0.046264([\Delta]+30)^{0.74578}.$$

The normal distribution law (Gaussian law), together with even one with a wavelet, barks a very high level of adequacy (more than 0.95) with a correlation coefficient of 0.9558.

Table 4. Distribution of the relative error of the model from Table 3.

Interval [Δ], °C	Qty *n*, pcs	Interval [Δ], °C	Qty *n*, pcs	Interval [Δ], °C	Qty *n*, pcs	Interval [Δ], °C	Qty *n*, pcs	Interval [Δ], °C	Qty *n*, pcs
22	1	10	6	3	89	–4	64	–11	7
16	2	9	15	2	80	–5	58	–12	7
15	4	8	19	1	99	–6	39	–13	7
14	5	7	34	0	0	–7	46	–14	1
13	3	6	44	–1	80	–8	26	–15	3
12	9	5	59	–2	93	–9	17	–16	3
11	2	4	70	–3	80	–10	16	–23	3

3.2 General formula (1) for the average monthly temperature with 12 components

Additional components of the model (1)

Subsequently, the identification method was used to build up asymmetric components from four components to reach 12 (**Table 5**) pieces. The first four components can be placed together in the CurveExpert-1.40 software environment (**Table 3**), and the remaining components of the general model (1) were identified individually.

This method of sequential modeling makes it possible to achieve a level of adequacy in terms of the correlation coefficient up to 1. The modeling is completed after reaching the residuals from the last component to the modeling error, which is less than the temperature measurement error.

From a physical point of view, each component is a separate quantum of climate behavior at a given point on the earth. The sum of wavelets (1) characterizes the oscillatory climate adaptation to the influence of many different factors. The high quantum certainty of the behavior of the average monthly temperature makes it possible to decompose the dynamic series into behavior quanta to a level where the modeling error becomes even less than the measurement error of 0.05 °C.

However, in this case, many components will have a correlation coefficient much less than the 0.1 level. Such correlation coefficients (less than 0.3) are not taken into account at all in the existing mathematical statistics. In **Table 5**, we stopped the process of wavelet identification at the level of adequacy by the correlation coefficient of 0.0580.

Analysis of graphs of average monthly temperature

As can be seen from the graphs in **Figures 6 and 7**, the length of the oscillation graphs, even for infinite-dimensional wavelets, is different.

It can be seen from the data in **Table 5** that almost all additional perturbation waves obey the Mandelbrot law. But at the same time, part of the oscillations increases, and the other part decreases, in amplitude. It is necessary to identify cause-and-effect relationships for oscillations decreasing in amplitude.

As a result, the atmosphere of New Delhi shows a violent wave reaction over time. Therefore, it is necessary to analyze more carefully those fluctuations that have a decline in amplitude in the future.

12-component model error distribution

With an increase in the number of wavelets in the general model (1), the relative modeling error gradually decreases.

The number of points n in the dynamic series of residuals is distributed without gaps. Due to the relatively small error of modeling by the general equation (1) with 12 components, the temperature interval was also taken equal to 1 °C. Then the permissible relative error $[\Delta]$ (°C) of the model (1) with the parameters from **Table 5**, after the 12th component, is given in **Table 6**.

The relative error is in the range of 23 to –19% (**Figure 8**).

Then the error changes according to the Gauss law with additional fluctuations in the form of a general equation:

$$n = 100.11057\exp(-0.022609([\Delta]-0.076252)^2) + 7.69774 \div 10^{-18}([\Delta]+25)^{17.213023}\exp(-0.33399([\Delta]+25)^{1.15822}) \times \cos(\pi([\Delta]+25)/(3.02798-1.40488([\Delta]+25))+2.80420)) \quad (3)$$

The normal distribution law (Gaussian law) is observed with adequacy in terms of the correlation coefficient of 0.9891. An additional wavelet showing the oscillatory adaptation of the mean monthly temperature also gives the value of the correlation coefficient of 0.6190. As a result, the overall adequacy of the relative error after the 12th component in the sum (1) will be equal to 0.9936.

Comparison of models with four and 12 components

Table 7 shows comparative data on the relative error of two quantized models - with four and 12 components (**Figure 9**).

From the data in **Table 7**, it can be seen that August has the smallest error for both models. Then it turns out that it is quite possible to perform forecasting only on the basis of a model of four components.

Table 5. Dynamics of average monthly temperatures in New Delhi for 1931-2021.

i	**Asymmetric wavelet** $y_i = a_{1i}x^{a_{2i}}\exp(-a_{3i}x^{a_{4i}})\cos(\pi x(a_{5i}+a_{6i}x^{a_{7i}})-a_{8i})$								Coef. correl. r
	Amplitude (half) oscillation				Half cycle oscillation			Shift	
	a_{1i}	a_{2i}	a_{3i}	a_{4i}	a_{5i}	a_{6i}	a_{7i}	a_{8i}	
5	–0.77866	0	0.049759	1	1.54931	0.19297	1.28120	4.11672	0.1178
6	0.11383	0	–0.00021302	1.92174	6.46965	0.0023525	1.52916	1.38105	0.1195
7	–0.00046760	0	–6.29355	0.0052852	5.32375	–4.74250	–0.18477	4.52957	0.1733
8	0.17311	0	0.00021873	1	2.50208	0.0025872	1.09110	1.82138	0.1057
9	0.13799	0	–0.0063418	1	1.65259	–0.0018465	1.00690	–4.28053	0.1171
10	–0.33772	0	0.038165	1	0.84645	0.0058586	1.49887	2.65045	0.0787
11	0.25699	0	0.024305	1	0.75658	–0.00033547	1	0.11626	0.0733
12	–0.17091	0	0.015905	1	1.03886	–0.00036249	1	–1.91769	0.0580

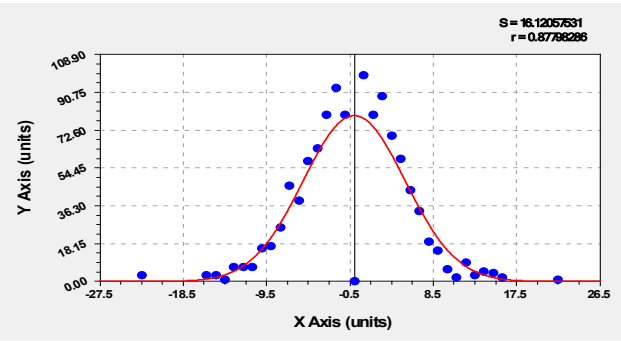

Gauss's law of normal distribution

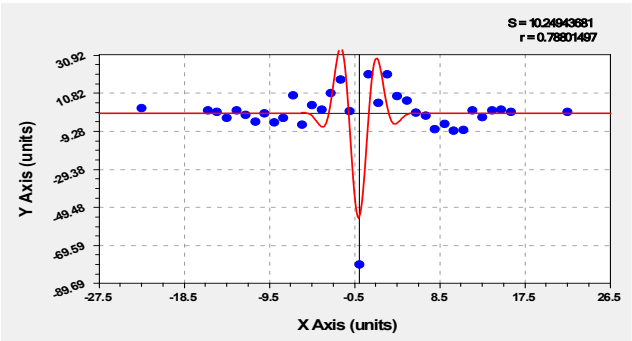

Asymmetric wavelet

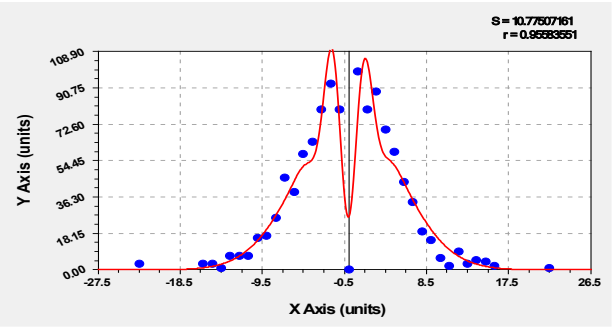

Gauss law and wavelet

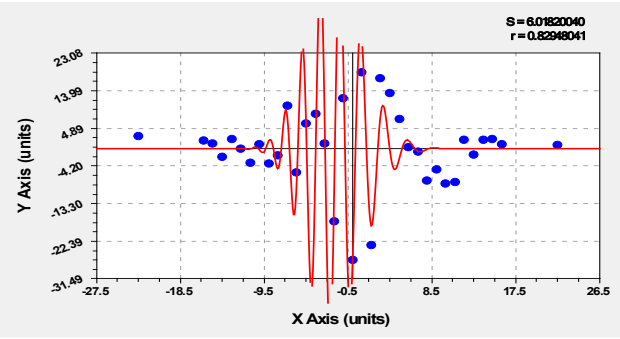

The second oscillation of the model error

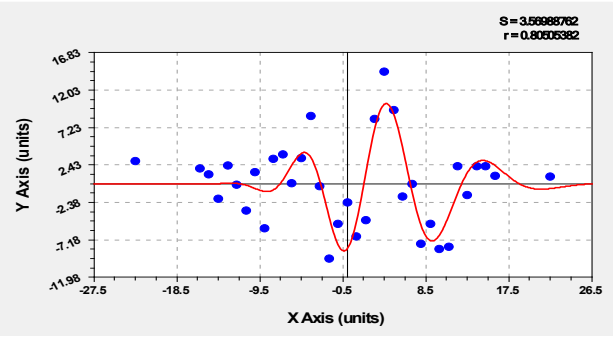

The third oscillation of the model error

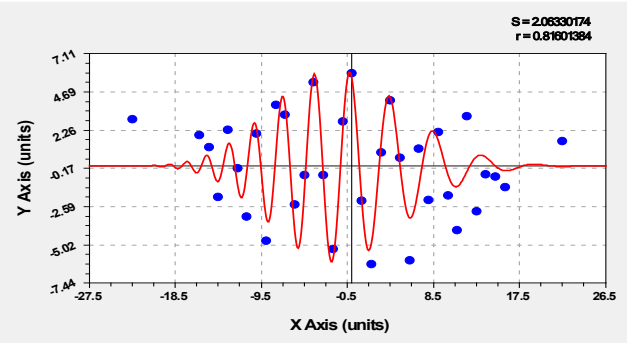

Fourth swing of model error

Figure 5. Graphs of the relative error of the five-component model.

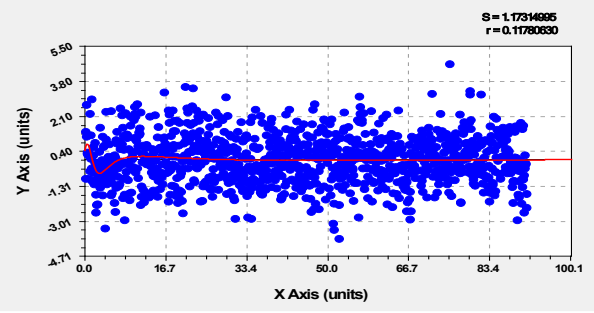

Fifth component

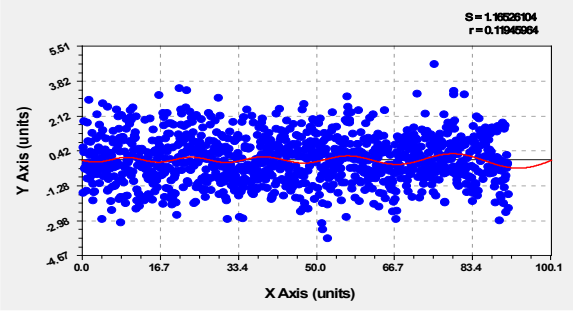

The sixth component of the model

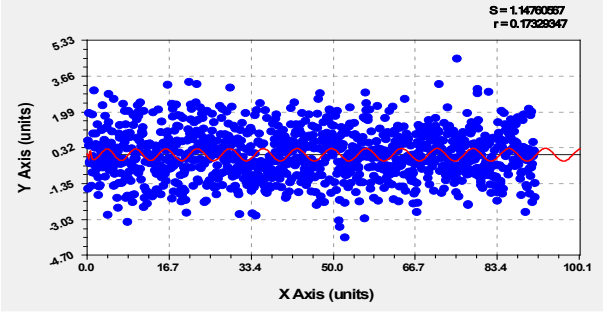

Seventh component

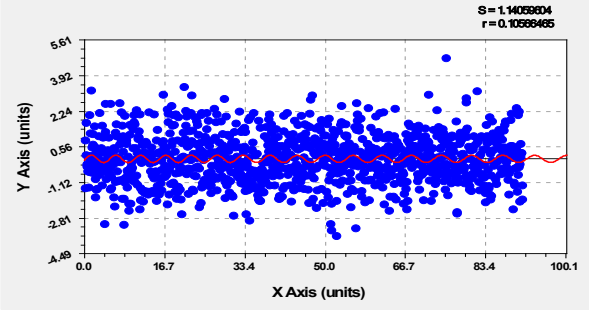

Eighth component

Figure 6. New Delhi monthly average temperature by additional components.

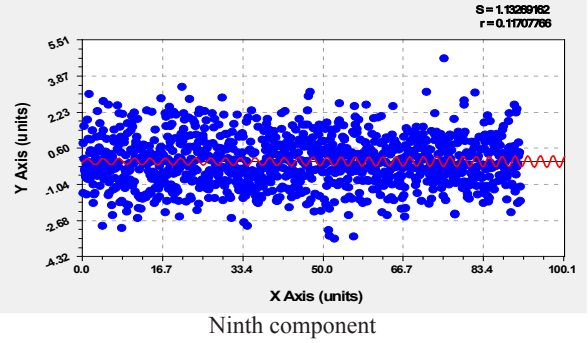

Ninth component

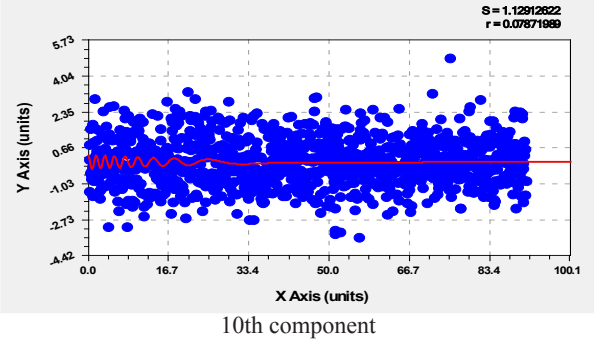

10th component

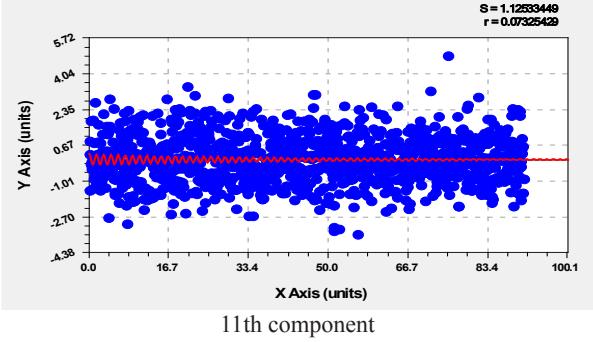

11th component

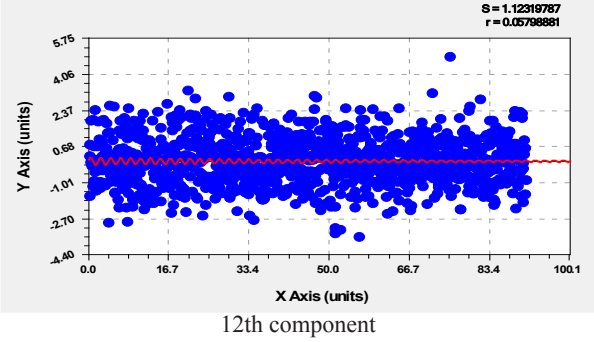

12th component

Figure 7. New Delhi monthly average temperature by latest components.

Table 6. Distribution of model error after the 12th component.

Interval [Δ], °C	Qty *n*, pcs	Interval [Δ], °C	Qty *n*, pcs	Interval [Δ], °C	Qty *n*, pcs	Interval [Δ], °C	Qty *n*, pcs	Interval [Δ], °C	Qty *n* , pcs
23	1	10	5	3	87	–5	55	–12	13
17	1	9	10	2	85	–6	48	–13	3
15	4	8	25	1	92	–7	35	–14	1
14	1	7	33	–1	107	–8	17	–15	3
13	3	6	46	–2	80	–9	19	–17	1
12	8	5	51	–3	80	–10	7	–18	1
11	6	4	84	–4	67	–11	11	–19	2

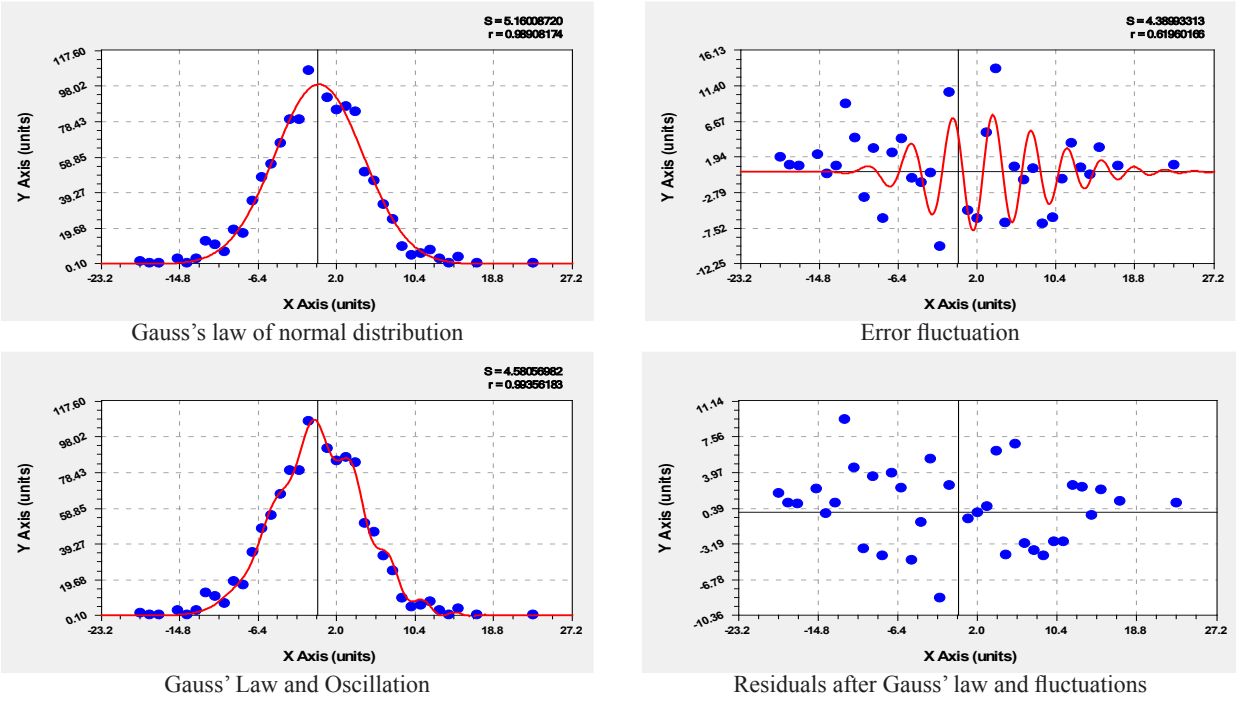

Gauss's law of normal distribution

Error fluctuation

Gauss' Law and Oscillation

Residuals after Gauss' law and fluctuations

Figure 8. Graph of the relative error distribution after the 12th wavelet.

Table 7. Relative error of models, %.

Month	Model contains	
	4 comp	12 comp
Jan	5.69	5.26
Feb	5.91	5.92
Mar	5.15	4.83
Apr	4.28	3.80
May	3.46	3.18
Iun	3.63	3.57
Jul	3.26	3.10
Aug	2.66	2.51
Sep	2.73	2.81
Oct	2.72	2.71
Nov	3.52	3.30
Dec	4.35	4.82

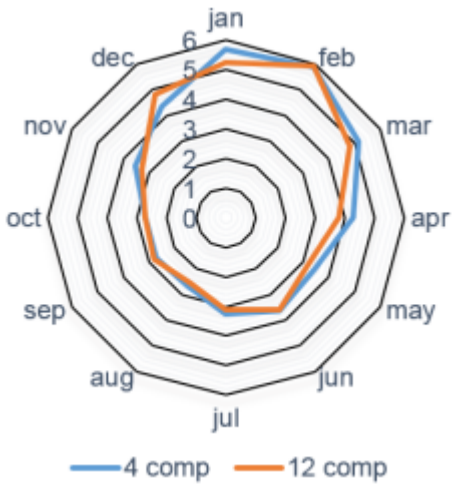

Figure 9. Graphs of comparison of the relative error of models.

At the same time, the critical thermal wave (increasing the second component in **Table 3**) is in this model and, therefore, a further increase in the number of wavelets becomes unjustified. If there were a supercomputer, then the joint identification of all possible components is possible. Such a technique can give a change in the second component of the critical thermal wave.

Then, for further modeling by identifying formula (1) from the data in **Table 1**, we will accept only a part of the array for August.

3.3 General formula (1) for the average monthly temperature for August

The structure of the general model for August 1931-2021

Table 8 shows the following components of model (1) for additional 16 components. Surprisingly, each month gives a lot of additional quanta of the behavior of the surface layer of the atmosphere at a height of 2 m in New Delhi.

All 16 wave equations are finite-dimensional wavelets. For them, according to the graphs, it is quite possible to roughly determine the left and right boundaries of the location of the graph on the x-axis.

In this regard, these solitons (solitary waves) seem to appear and then disappear with time. Therefore, apparently, the reasons for the emergence of finite-dimensional wavelets lie in the behavior of the atmosphere itself, as well as space objects located in sectors of the earth's orbit plane for different months. In our opinion, only infinite-dimensional temperature wavelets depend on the cosmic influences of the sun and the planets of the solar system.

Characteristics of dynamics graphs for August

As can be seen from the graphs in **Figure 10**, not all components of model (1) affect the conditional forecast in the near future, but only those that continue in terms of amplitude values in the future. At the end of the dynamic series, new fluctuations may additionally arise, which then, after several months, will continue into the future. It is this circumstance that does not allow making working forecasts for more accurate sums of 12 and 28 components, since models with an increased number of components become too sensitive to the influence of even small (with a correlation coefficient less than 0.1) wavelet signals.

As a result, the physical value of the average monthly (influence of the sun and the moon), as well as the average annual (influence of the sun) temperature, has two contradictory properties.

First, the time series of temperature, which has a high quantum certainty in behavior, allows decomposing up to the measurement error into a large number of asymmetric wavelets. Then it turns out that the average monthly temperature gets a quantum certainty due to the fact that each wavelet separately represents a separate quantum of the behavior of the climate system at the weather station in New Delhi. Note that other meteorological parameters do not have quantum certainty in their behavior.

Secondly, with an increase in the number of components in the general summary model (1), due to the high sensitivity, the predictive ability of the sum of wavelets is gradually lost. Even next year, the calculated average monthly temperature may not coincide with the actual temperature in many respects. In this regard, it turns out to be sufficient for looking into the future, a model of four components according to the parameters given in the values in **Table 3**. And for the New Delhi weather station, the second component becomes the decisive wavelet, which becomes the critical wavelet and characterizes a strongly growing heat wave.

Table 8. Dynamics of average monthly temperatures in New Delhi for 1931-2021 for August.

i	**Asymmetric wavelet** $y_i = a_{1i}x^{a_{2i}}\exp(-a_{3i}x^{a_{4i}})\cos(\pi x(a_{5i}+a_{6i}x^{a_{7i}})-a_{8i})$								Coef. correl. r
	Amplitude (half) oscillation				Half cycle oscillation			Shift	
	a_{1i}	a_{2i}	a_{3i}	a_{4i}	a_{5i}	a_{6i}	a_{7i}	a_{8i}	
13	3.47710e-6	8.50848	0.32835	1	0.36199	1.47479	1.01006	–2.66873	0.4194
14	–1.28535	0.29959	0.088382	1	5.25491	–0.088847	1	–4.18195	0.4925
15	–3.8370e-9	6.10340	0.10093	1.01977	1.55201	0	0	–2.25724	0.2747
16	0.70396	0	0.50141	0.20109	2.00648	–4.5732e-5	1.25112	–0.79170	0.2878
17	8.7308e-27	17.55018	0.18058	1.04346	8.61288	0	0	–5.04691	0.3685
18	–0.0053663	1.14901	0.00015363	1.90943	1.10816	0.045767	0.74931	0.86680	0.4058
19	–9.401e-28	34.44084	8.81058	0.52596	0.99962	0	0	0.57564	0.3583
20	–15908.61	4.04026	12.64317	0.18869	1.25195	0	0	0.037839	0.6217
21	–22.15650	2.24725	6.61109	0.18846	4.16157	0.015145	1.29649	1.72332	0.2660
22	–0.073147	0	–0.00013415	1.96363	2.76671	–0.0011047	1.03183	2.08059	0.2123
23	–3.559e-16	10.56709	0.15209	1.00601	2.57131	–0.0008103	1.20407	–5.84608	0.2477
24	1.8458e-10	7.14673	0.13089	0.99281	1.88417	–0.0005876	1.20551	–2.65356	0.3686
25	2.8793e-19	13.79026	0.25010	0.99909	5.41479	–0.0002402	1.56399	3.76089	0.3858
26	2.87943e-5	3.71815	0.21272	0.83732	1.77738	–0.0003534	1.16645	0.92034	0.3769
27	–1.5177e-6	4.16863	0.0014979	2.13676	5.44870	–0.26388	0.47163	–2.97005	0.2885
28	–0.11530	0.95160	0.050027	1.33562	1.03027	0	0	–2.19074	0.6866

Everything in nature is subject to vibrational adaptation. The air is so changeable that on the surface of the earth there are many fluctuations, first of all, in air temperature. Why can a dynamic series be decomposed into a large set of oscillations? Other meteorological parameters are not amenable to wavelet analysis. We don't know yet. Also, New Delhi is a unique geographic point on earth, the dynamics of the average monthly temperature which is clearly determined by the heat wave in the form of the second critical fluctuation.

This heat wave, in our opinion, has a decisive influence on the productivity of the vegetation cover in India.

A paper by Singh et al. [19] attempts to estimate and predict the impact of climate on crop yields using future temperature predictions in India's agro-climatic zones. It was found that rainfall had a positive effect on the yield of most crops, but not enough to offset the effect of temperature.

Model error distribution for August

With an increase in the number of wavelets up to 28 in model (1), the relative modeling error decreases. At the same time, 91 temperature values remain for August.

The number of points in the dynamic series of residuals after the 28th component is distributed, due to the small modeling error, over the intervals of the average monthly temperature in August every 0.5 °C. Then the permissible relative error $[\Delta]$ (°C) of the 28th component of the model (1) is given in **Table 9**.

The relative error is in the range of 2 to –2%.

Then the error changes according to the Gauss law (**Figure 11**) with one additional oscillation in the form of a general equation.

$$n = 45.09105\exp(-1.25253([\Delta]+0.045182)^2) + 5.95989([\Delta]+2.5)^{1.54256}\exp(-0.46127([\Delta]+2.5)) \times\cos(\pi([\Delta]+2.5)/(1.31852-0.12463([\Delta]+2.5))-1.27987) \quad (4)$$

As can be seen from the graphs of the distribution of residues after model (4), they get almost zero value.

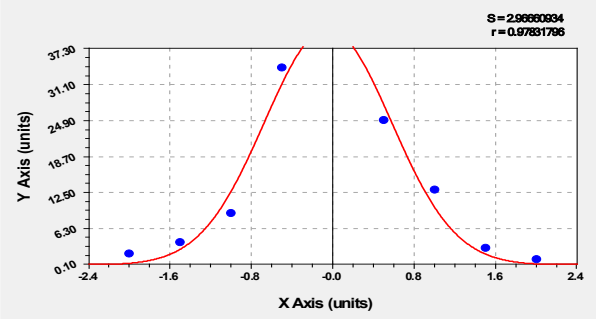

Gauss's law of normal distribution

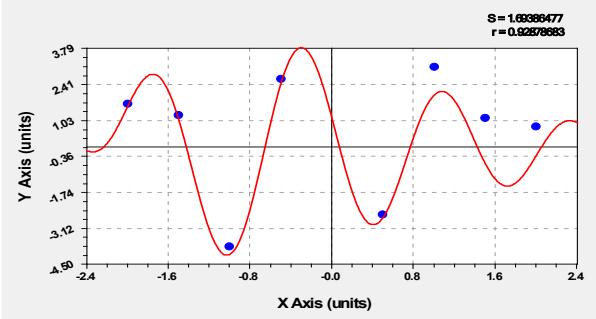

Error fluctuation

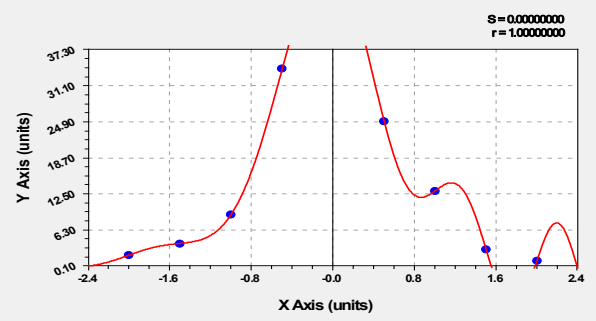

Gauss' Law and Oscillation

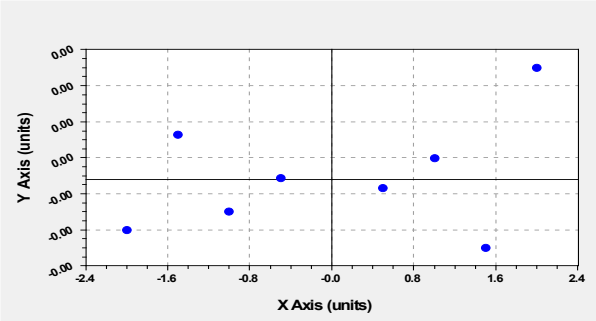

Residuals after Gauss' law and fluctuations

Figure 11. Relative error distribution plots after the 28th wavelet.

4. Forecast for the four-term model until 2110

4.1 New Delhi monthly average temperature forecast

On many examples of modeling by the identification method, it was noticed that with an increase in the number of components, the sensitivity of conditional forecasting increases sharply. Therefore, for orientation to the future, models with several components are sufficient, of which some component is critical, simultaneously identified in the CurveExpert-1.40 software environment with a high overall correlation coefficient (in **Table 3** for a four-term model it is 0.9847).

It can even be argued that if a critical component appears, then the simulation can be immediately stopped.

After identifying the critical heat wave, the forecast for the future is clearly non-obvious due to the fact that there is a quantum uncertainty in the behavior of India, due to the presence and growth of the critical heat wave. Therefore, attention should be paid to understanding the essence of the climate crisis, for example, in comparison with the climate dynamics in Beijing and other large Asian cities. It is important for India to urgently adopt a national reforestation program, as was done in China in 1970 (in the US since 1960).

The forecasting possibilities decrease with the increase in the number of wavelets in the sum (1). Already in the near future, new micro-fluctuations may appear, which can dramatically change the forecast trends in the past. To verify the predictive model, it is enough to wait one year (12 months) to obtain the actual values of the average monthly temperature. Then, a year later, the previously created predictive model is re-identified, containing wavelets for the future. This is how conditional forecasts are refined in the iterative forecasting mode every year.

In **Table 3**, the parameters of model (1) are given with five significant figures. However, in the calculations we used all 11 significant figures.

For example, a model with four components is

written as:

User-Defined Model:

y=a*exp(-b*x)+c*x^d*exp(e*x^f)

-g*exp(-h*x)*cos(pi*x/0.5-i) (5)

+j*exp(k*x^l)*cos(pi*x/0.25-m).

Coefficient Data:

a = 2.39931742757E+001 b = 3.19834420708E-003

c = 7.01935956544E-001 d = 3.80930974140E-001

e = 1.45040504760E-002 f = 8.45501296252E-001

g = 9.20090113775E+000 h= 2.52299200889E-004

i = 3.32186333451E-001 j= 1.18493842254E+000

k = 6.52201603490E-001 l = 2.17933213594E-002

m= 4.37689258906E+000

After calculations in the Excel software environment using formula (5), graphs (**Figure 12**) of the average monthly temperature for each month from 1931 to 2110 were obtained.

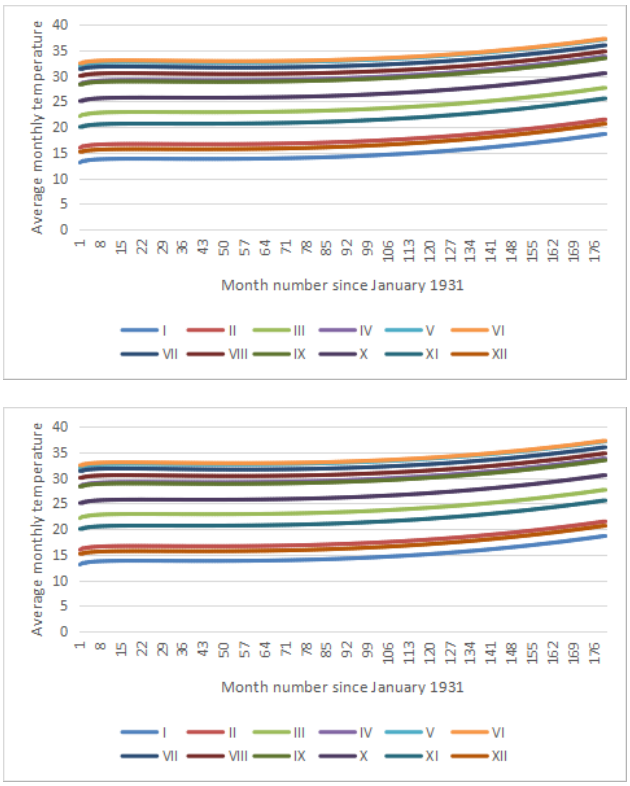

Figure 12. Monthly average temperature forecasts up to 2110.

For all months of each year, there is an increase in the average monthly temperature. The warming level of 2010 will repeat again in 2035-2040. Therefore, a period of 25-30 years since 2010 can be taken as a stage of a slight cooling in India. However, from 2040, the average monthly temperature will steadily increase.

Table 10 shows the temperature values for 12 months.

Table 10. Forecast for the four-component model for all 12 months.

Month	Forecast basis			Forecast horizon			
	1931	2010	2021	2030	2040	2070	2110
Jan	15.4	13.7	12.9	14.46	14.76	16.04	18.72
Feb	15.2	18.7	18.6	17.33	17.62	18.88	21.55
Mar	21.2	26.3	25.0	23.55	23.84	25.08	27.73
Apr	29.7	32.7	28.6	29.76	30.04	31.26	33.86
May	33.1	34.7	30.4	33.16	33.43	34.61	37.18
Jun	35.1	34.5	32.4	33.36	33.62	34.78	37.31
Jul	31.7	31.4	31.5	32.1	32.36	33.51	36.04
Aug	30.3	30.1	30.9	30.86	31.13	32.3	34.85
Sep	28.6	28.3	29.0	29.42	29.69	30.9	33.5
Oct	25.3	26.9	26.0	26.39	26.68	27.94	30.59
Nov	19.1	21.3	18.8	21.38	21.68	22.96	25.66
Dec	15.5	15.0	14.5	16.41	16.71	18.01	20.73

As in 1931, starting from 2021 and beyond, June becomes the hottest month. At the same time, the maximum temperature of 35.1 °C in June will reach only by 2076. For this month, the minimum temperature was: 1936-31.2 °C; 2001-31.1 °C; 2008-30.9 °C. The coldest June was in 2008.

Figure 13 shows a radar chart for three forecast years (2040, 2070 and 2110) compared to 2010. The diagram clearly shows that by month 2110 covers the average monthly temperature of other years.

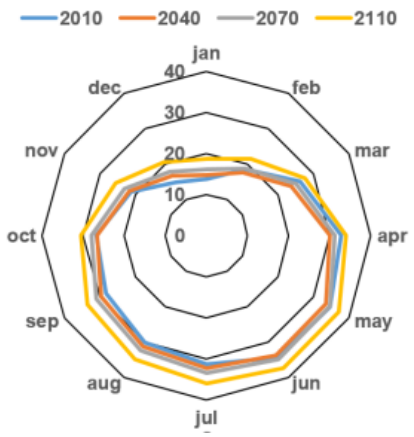

Figure 13. Average monthly temperatures compared to 2010.

Thus, from 2010 to 2076, nature gives the population of India the opportunity to increase the forest area, as well as manage to reduce the average monthly temperature by geo technical measures [12] during this period of time.

4.2 Critical New Delhi heatwaves in June

Further, for hot June, we consider separately the changes in the average monthly temperature over the time interval from 1931 to 2110.

Figure 14 shows graphs for June, built according to formula (5).

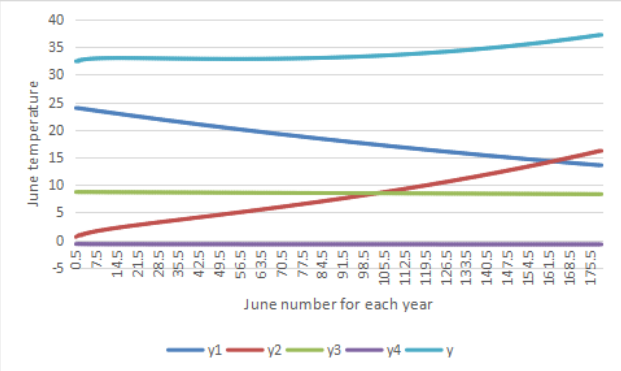

Figure 14. Graphs of the components of the June temperature in New Delhi.

The first component of the influence of cosmic cold from 1931 to 2110 decreases from a temperature of 23.95 to 13.51 °C, that is, a decline in the natural tendency will occur by 23.95 – 13.51 = 10.44 °C. But, for the same period of time in 180 years. According to the second component in the form of an anomalous bio technical law, the average June temperature will increase from 0.54 to 16.29 °C, that is, the increase in heat will be 15.75 °C. This growth was influenced by two major causes: Firstly, the anthropogenic reduction of the vegetation cover of India in favor of agricultural plants; secondly, the strengthening of the geophysical influence of the Himalayas on blocking the winds and isolating the climate of India.

The annual and semi-annual cycles had an insignificant effect on the dynamics of the June temperature. The third component of the annual dynamics gave a decrease in the average monthly temperature from 8.70 to 8.31 °C, that is, over 180 years there will be a decrease in temperature by 0.39 °C. Similarly, according to the fourth component of the semi-annual cycle, the decrease in June temperature will be from –0.74 to –0.81, that is, by only 0.07 °C.

These data show that the revolutions of the earth around the sun and the vegetation cover on the land of both hemispheres of our planet have little effect on the thermal balance of India. The critical thermal wave is created by the second component (5).

5. Conclusions

The wave patterns of the average monthly temperature at the New Delhi meteorological station from 1931 to 2021 revealed by the identification method in the form of a sum of wavelet signals made it possible to give a conditional forecast up to 2110. At the New Delhi meteorological station, the oscillatory adaptation of the local climate according to the average monthly temperature in the near future will far exceed the global warming rates predicted in the IPCC CMIP5 report for the entire land mass of the earth.

At the same time, it should be taken into account that the surface of India heats up to 45 °C in summer, which is a tenth or higher than the air layer at a height of 2 m in a weather station. Temperatures rise even higher on paved roads and concrete urban areas (up to 55 °C [20]).

The maximum increment in 80 years of average monthly temperature in New Delhi of 5.1 °C was in March 2010.

Warming in descending order of average monthly temperature occurred in March (5.1), February (3.5), April (3.0), November (2.2), October (1.6) and May (1.6 °C). Cooling in comparison with 1931 occurred in August (–0.2), July and September (–0.3), December (–0.5), June (–0.6) and January (–1.7 °C). If the difference in average monthly temperatures in 1931 was equal to 19.9 °C, then in 2010 it became equal to 21.0 °C.

At the beginning of the modeling process, the identification of asymmetric wavelet signals revealed a trend containing two regularities. The first compo-

nent is the Mandelbrot law (in physics) of the exponential decrease in the mean monthly temperature. The same law is known in mathematics as the Laplace law, in biology - Zipf-Pearl, in econometrics - Pareto. It shows a natural trend from 1931 to 2021 of a slow decrease in the average monthly temperature. Such a natural cause of decline is the cosmic cold that endlessly surrounds planet Earth. Therefore, with any oscillatory perturbations of the global climate in the earth's atmosphere, the planet will eventually slowly cool down in billions of years.

The second component of the trend for New Delhi for 91 years is growing according to a mathematical power function $y = ax^b$. But it turned out that the influence of the Himalayas gives an increase in the average monthly temperature even according to the law of "double" growth according to the formula of the anomalous biotechnical law $y = ax^b \exp(cx^d)$ of prof. P.M. Mazurkin. Here, the sign of the decreased activity got a positive value $\pm c$, therefore, a product of two growth laws was formed—a power function and a modified Mandelbrot law under the condition $d \neq 1$. The trend has grown over time and it is necessary to take geo-technical measures to eliminate the second component of the trend.

The third component of the four-component model is the first fluctuation with a correlation coefficient of 0.9522, which is an infinite-dimensional wavelet, that is, it starts much earlier than 1931 and continues much further than 2021. This infinity is provided by the amplitude, which decreases with time according to the Mandelbrot law. Therefore, a distinctive feature of the annual cyclicity is the continuous decrease in the amplitude of fluctuations, which will favorably affect the regional climate of India.

The second fluctuation (a fourth component of the summary model) with a semi-annual cyclicity is typical not only for air temperature, but also for the concentrations of various greenhouse gases, especially for CO_2. For carbon dioxide, it was assumed that the cycles of half a year are influenced by the vegetation cover of both hemispheres of the earth. Apparently, the vegetation cover (grass + shrub + trees) of India for 4000 years has been severely depleted by people for the needs of agriculture.

For all months of each year, there is an increase in the average monthly temperature. The level of warming before 2010 will repeat again in 2035-2040. Therefore, a period of 25-30 years can be taken as a stage of a slight cooling in India. However, from 2040, the average monthly temperature will steadily increase. As in 1931, starting from 2021 and beyond, June becomes the hottest month. At the same time, the maximum temperature of 35.1 °C in June will reach only by 2076. For this month, the minimum temperature was: 1936-31.2 °C; 2001-31.1 °C; 2008-30.9 °C. The coldest June was in 2008.

For the hottest of all 12 months of June, the first component of the influence of cosmic cold from 1931 to 2110 decreases from a temperature of 23.95 to 13.51 °C, that is, the decline in the natural tendency will occur by 23.95 – 13.51 = 10.44 °C. But, for the same period of time in 180 years. according to the second component in the form of an anomalous biotechnical law, there will be an increase in the average June temperature from 0.54 to 16.29 °C, that is, an increase in heat will be 15.75 °C. This growth was influenced by two major reasons: Firstly, the anthropogenic reduction of the vegetation cover of India in favor of agricultural plants; secondly, the strengthening of the geophysical influence of the Himalayas on blocking and isolating the climate of India.

The annual and semi-annual cycles had an insignificant effect on the dynamics of the June temperature. The third component of the annual dynamics gave a decrease in the average monthly temperature from 8.70 to 8.31 °C, that is, over 180 years, the temperature will decrease by 0.39 °C. Similarly, according to the fourth component of the semi-annual cycle, the June temperature will decrease from –0.74 to –0.81, that is, by only 0.07 °C.

Conflict of Interest

There is no conflict of interest.

Funding

This research received no external funding.

References

[1] Ancient India [Internet] [cited 2022 Apr 22]. Available from: https://history.wikireading.ru/314323.

[2] Kumar, B., Asad, A.I., Chandraaroy, B., et al., 2019. Perception and knowledge on climate change: A case study of university students in Bangladesh. Journal of Atmospheric Science Research. 2(3). doi: 10.30564/jasr.v2i3.1542.

[3] India Getting Warmer, Hotter: 2021 Fifth Warmest Year Since 1901, Says IMD [Internet] [cited 2022 May 21]. Available from: https://www.business-standard.com/article/current-affairs/india-getting-warmer-hotter-2021-fifth-warmest-year-since-1901-says-imd-122011401133_1.html.

[4] Extreme Heat in India [Internet] [cited 2022 Apr 22]. Available from: https://www.drishtiias.com/daily-updates/daily-news-editorials/heat-extremes-in-india.

[5] Climate of India [Internet] [cited 2022 Apr 22]. Available from: https://fb.ru/article/146454/klimat-indii-osobennosti-klimata-indii.

[6] Li, G.X., Zhou, G., 2016. Comparisons of time series of annual mean surface air temperature for china since the 1900s: Observations, model simulations, and extended reanalysis. Bulletin of the American Meteorological Society. 98(4), 699-711. doi: 10.1175/bams-d-16-0092.1.

[7] Chernokulsky, A., 2022. Замерзнет ли Европа без Гольфстрима? (Russian) [Will Europe freeze without the Gulf Stream?] [Internet] [cited 2022 Mar 13]. Available from: https://zen.yandex.ru/media/nplus1/zamerznet-li-evropa-bez-golfstrima-62028bab5eaa831b62461219?&utm_campaign=dbr&.

[8] Abdussamatov, H.I., 2020. Absence of the impact of the flux of cosmic rays and the cloud cover on the energy balance of the earth. Journal of Atmospheric Science Research. 3(3), 1-7. doi: 10.30564/jasr.v3i3.2129.

[9] Bhargawa, A., Singh, A.K., 2021. Perceiving the trend of terrestrial climate change during the past 40 year (1978-2018). Journal of Atmospheric Science Research. 4(1), 1-15. doi: 10.30564/jasr.v4i1.2488.

[10] Slama, R.B., 2020. Global warming and its multiple causes. Journal of Atmospheric Science Research. 3(2), 28-31. doi: 10.30564/jasr.v3i2.2013.

[11] Ullah, A., Ahmad, S.I., Ullah, R., et al., 2020. Climatic changes and their effect on wildlife of district dir lower, Khyber Pakhtunkhwa, Pakistan. Journal of Atmospheric Science Research. 3(4), 38-43. doi: 10.30564/jasr.v3i4.2275.

[12] Mazurkin, P.M., 2022. Asymmetric mean annual temperature wavelets surface air layer of Berlin for 1701-2021. Journal of Atmospheric Science Research. 5(3), 1-9. doi: 10.30564/jasr.v5i3.4674.

[13] Mazurkin, P.M., 2022. Quantum biophysics of the atmosphere: Asymmetric wavelets of the average annual air temperature of Irkutsk for 1820-2019. Journal of Environmental & Earth Sciences. 4(2), 1-16. doi: 10.30564/jees.v4i2.4586.

[14] Mazurkin, P.M., 2022. Wave dynamics of the average annual temperature surface air layer New Delhi for 1931-2021. Journal of Atmospheric Science Research. 5(2), 52-66. doi: 10.30564/jasr.v5i2.4639.

[15] Mazurkin, P.M., Kudryashova, A.I., 2019. Quantum meteorology. International Multidisciplinary Scientific GeoConference Surveying Geology and Mining Ecology Management, SGEM. (5.1), 619-627. doi: 10.5593/sgem2019/5.1/S20.077.

[16] Mazurkin, P.M., Kudryashova, A.I., 2019. Городская фитометеорология: влияние суммы температур на онтогенез листьев березы повислой. Географический вестник (Russian) [Urban phytometeorology: Influence of the sum of temperatures on the ontogeny of drooping birch leaves]. Geographical Bulletin. 4(51), 45-58. doi: 10.17072/2079-7877-2019-4-45-58.

[17] Zavalishin, N.N., 2018. The model of dependence of the temperature of the surface layer of atmosphere from the earth's Albedo and thermal inertia of the hydrosphere. Journal of Atmospheric Science Research. 1(1), 13-17. doi:

10.30564/jasr.v1i1.373.

[18] Zavalishin, N.N., 2022. Reasons for modern warming: Hypotheses and facts. Journal of Atmospheric Science Research. 5(1), 11-17.

[19] Singh, N.P., Anand, B., Srivastava, S.K., et al., 2020. Assessing the impacts of climate change on crop yields in different agro-climatic zones of India. Journal of Atmospheric Science Research. 3(4), 16-27. doi: 10.30564/jasr.v3i4.2269.

[20] Chernokulsky, A. Limits of adaptation: How in India they endure catastrophic heat [Internet] [cited 2022 Nov 19]. Available from: https://nplus1.ru/blog/2022/05/06/india-heatwave?from=feed&utm_referrer=https%3A%2F%2Fzen.yandex.com&utm_campaign=dbr (in Russian).

BILINGUAL PUBLISHING GROUP

Journal of Atmospheric Science Research
https://journals.bilpubgroup.com/index.php/jasr

ARTICLE

Investigating the Effects of Madden-Julian Oscillation on Climate Elements of Iran (1980-2020)

Kourosh Mohammadpour[1*], Zahra Hejazizadeh[1], Hooshang Ghaemi[2], Mohammad Salighe[1]

[1] *Department of Natural Geography, Kharazmi University, Tehran, 15447-33111, Iran*
[2] *Tehran Institute of Meteorology and Atmospheric Sciences, Tehran, 15447-33111, Iran*

ABSTRACT

The Madden-Julian Oscillation is one of the large-scale climate change patterns in the maritime tropics, with sub-seasonal time periods of 30 to 60 days affecting tropical and subtropical regions. This phenomenon can cause changes in various quantities of the atmosphere and ocean, such as pressure, sea surface temperature, and the rate of evaporation from the ocean surface in tropical regions. In this research, the effects of Madden-Julian fluctuation on the weather elements of Iran have been investigated with the aim of knowing the effects of different phases in order to improve the quality of forecasts and benefits in territorial planning. At first, the daily rainfall data of 1980-2020 were received from the National Meteorological Organization and quality controlled. Using the Wheeler and Hendon method, the two main components RMM1 and RMM2 were analyzed, based on which the amplitude of the above two components is considered as the main indicator of the intensity and weakness of this fluctuation. This index is based on the experimental orthogonal functions of the meteorological fields, including the average wind levels of 850 and 200 hectopascals and outgoing long wave radiation (OLR) between the latitudes of 20 degrees south and 20 degrees north. The clustering of the 7-day sequence with a component above 1 was used as the basis for clustering all eight phases, and by calculating the abnormality of each phase compared to its long term in the DJF time frame, the zoning of each phase was produced separately. In the end, phases 1, 2, 7, 8 were concluded as effective phases in Iran's rainfall and phases 3, 4, 5, 6 as suppressive phases of Iran's rainfall.

Keywords: Madden-Julian oscillation; Tropical convection; precipitation; Long-wave radiation; Sub-seasonal oscillation

*CORRESPONDING AUTHOR:
Kourosh Mohammadpour, Department of Natural Geography, Kharazmi University, Tehran, 15447-33111, Iran; Email: dr.kourosh_mohammadpour@yahoo.com

ARTICLE INFO
Received: 26 December 2022 | Revised: 29 March 2023 | Accepted: 31 March 2023 | Published Online: 14 April 2023
DOI: https://doi.org/10.30564/jasr.v6i2.5351

CITATION
Mohammadpour, K., Hejazizadeh, Z., Ghaemi, H., et al., 2023. Investigating the Effects of Madden-Julian Oscillation on Climate Elements of Iran (1980-2020). Journal of Atmospheric Science Research. 6(2): 21-32. DOI: https://doi.org/10.30564/jasr.v6i2.5351

COPYRIGHT
Copyright © 2023 by the author(s). Published by Bilingual Publishing Group. This is an open access article under the Creative Commons Attribution-NonCommercial 4.0 International (CC BY-NC 4.0) License. (https://creativecommons.org/licenses/by-nc/4.0/).

1. Introduction

Bridging the gap between spatial-temporal and climatic scales and an in-depth understanding of planetary systems is always an important challenge that the atmospheric community faces. Undoubtedly, progress in medium-range and seasonal weather forecasting and our understanding of large-scale weather patterns and the identification of specific causes of their occurrence rely on our deep understanding of the behavior of atmospheric-oceanic patterns and their relationship with each other [1]. Pressure anomalies and atmospheric and oceanic circulation patterns sometimes impose their direct and indirect effects on areas beyond the birthplace of the current [2], which is explained by the term "circulation" [3]. As we know Madden Oscillation Julian (MJO) is a distant coupling pattern and the dominant form of sub-seasonal variability in tropical and subtropical regions, which plays an important role in the atmosphere-ocean circulation system [4]. According to different theories, this phenomenon can be effective in the intraseasonal time scale in its different phases in the region of Southwest Asia, including Iran [5]. Considering the problem of water shortage in the country and the importance of planning in this area, revealing a zoning model of the various effects of this fluctuation in the country is of great importance [6]. It should be mentioned that due to the short life of knowing the effects of this fluctuation on Iran, the lack of a zoning model of the effects caused by Madden-Julian's fluctuation on Iran is felt in the scientific community of the country [7]. On the other hand, the analysis of the different phases of this fluctuation in Iran can smooth out the contradictions of theories in recent years and the results of this research can be a light for the country's macro-planning and development on the path of territorial development and sustainable development [8]. Madden-Julian Oscillation is one of the most important general atmospheric circulation phenomena in tropical regions and has been widely studied and researched in recent decades [9]. The use of this phenomenon to predict rainfall in the inter-seasonal time scale requires knowledge of its nature as well as the physical processes that occur during its evolution and distribution. This phenomenon was first discovered by Madden and Julian (1971) [10]. By spectral analysis of ground pressure data and the orbital component of the wind field from the surface of the earth to the upper levels of the atmosphere at the Canton Island station (3 degrees south and 172 degrees west), they found out the existence of a 30-60 day fluctuation in the changes of these parameters. Further research showed that such fluctuation exists in other parts of tropical regions. They considered this fluctuation to be caused by the phenomenon of convection in a large-scale orbital circulation cell moving eastward in tropical regions, which is associated with convergence at low levels of 850 hectopascals and divergence at high levels of 200 hectopascals [11]. Madden and Julian (1994) introduced this phenomenon as the strongest climatic factor in tropical regions with an inter-seasonal time scale. This phenomenon can cause variability in various parameters of the atmosphere and ocean, such as land surface pressure, wind field, cloud cover, precipitation, air temperature, sea surface temperature, and evaporation rate from the ocean surface in tropical regions [12]. In the following, some important features of this phenomenon will be discussed [13]. The inter-seasonal period of a complete MJO cycle Madden and Julian (1971) estimated the lifetime of a complete MJO cycle to be about 40-50 days using 10 years of upper atmosphere data at the Canton Island station. Then, using the data of the orbital component of the wind field at the level of 150 hPa at the Truk Island station (7 degrees south and 152 degrees east), they estimated this period to be about 22 to 79 days with an average of 45 days (Madden and Julian, 1994). The use of variability in other committees had little difference from the previous results. For example, Knutson et al. (1986) investigated the eastward propagation of OLR anomalies and obtained two events with a lifetime period of fewer than 20 days and two events with a lifetime period of more than 79 days. The lifetime period of a complete MJO

oscillation is 30 to 60. It is a day that its maximum frequency is observed in about 45 days (Madden and Julian, 1994).

2. Data and method

In the implementation of the research process on the effects of Madden-Julian fluctuation on Iran's climate, in the beginning, daily data of precipitation, maximum temperature, minimum temperature and cloud cover were received from the country's meteorological organization, which only 48 stations have data due to the start of the period since 1980. The few available gaps were processed on some days. In order to reduce the error in the possible results, with the specialized software of the data bank of the National Meteorological Organization, the data sets were quality controlled and verified and finally standardized. Next, the output data of the Wheeler and Hendon model were received and processed from the Australian Government Meteorological Database (http://www.bom.gov.au) in the mentioned time period. Various indicators have been provided to check this fluctuation. The method that has been used in the stages of this research is the Wheeler and Hendon method, which has been used as a reference for all the researchers conducted, in which the two main components of RMM1 and RMM2 are analyzed based on the formula introduced by Wheeler and Hendon. The range of the above two components is considered as the main indicator.

$$\text{Amplitude} = \sqrt{\text{RMM1}^2 + \text{RMM2}^2} \tag{1}$$

This index is based on the experimental orthogonal functions of meteorological fields, including the average wind levels of 850 and 200 hectopascals and outgoing long wave radiation (OLR) between latitudes of 15 degrees south and 15 degrees north (Wheeler and Hendon, 2004). In order to emphasize the role of Madden-Julian on Iran's rainfall and remove the phenomena of less than 30 and more than 60 days, these anomalies were passed through a time-lapse filter. For this purpose, each of the anomalies on the day is presented as follows (Duchon, 1979: Jones et al., 1997):

$$y_t = \sum_{k=-n}^{n} w_k x_{t-k}$$

$$w_k = \left[\frac{\sin(2\pi f_{c2}k)}{\pi k} - \frac{\sin(2\pi f_{c1}k)}{\pi k}\right]\sigma$$

$$f_{c1} = 1/60day^{-1}, f_{c2} = 1/30day^{-1} \tag{2}$$

$$n = 24 \quad \sigma = \frac{\sin\left(\frac{\pi k}{n}\right)}{\left(\frac{\pi k}{n}\right)}$$

In these relations **wk**, the weighting coefficients, f_{c1} and f_{c2} are the highest and lowest frequencies, respectively [14]. As a result, by applying these filters, phenomena whose activity period is more than 60 days and less than 30 days will be removed from the data groups. In the next step, the data of 40 years of parameters of daily precipitation, maximum temperature, minimum temperature and amount of cloudiness in each phase were clustered separately and prepared through various standardizations in Excel and Mini Tab software. Then, using Arc software GIS was concluded as zoning. In order to check the standard of phases and its effects on the climatic region of Iran, the long-term data of the phases of Madden-Julian oscillations have been considered in the clustering stage as a sequence of 7 days and more. This filter separately shows the net effects of this fluctuation on the study area, in the continuation of the purification process and application of various filters. With this condition, the number of days related to each phase in the study period is given. In this table, phases one, which is considered the birth of the Madden-Julian oscillation, have the minimum frequency and phase seven has the maximum frequency. The second part of **Table 1**, it refers to the number of consecutive periods of 7 days and more, among which phase one has the shortest period and phase 7 has the longest period [15].

Next, for the synoptic analysis of the studied meteorological quantities, the maps of the pressure fields of the earth's surface, geopotential height and wind at the standard pressure levels of each of the phases, from the daily data of the global reanalysis of the NCEP/NCAR database during the forty-year

winter period (including the month December, January and February corresponding to the years 1980 to 2020) were extracted for the region of Western Europe to Central Asia. Abnormality maps of the above atmospheric patterns of each of the eight phases of the Madden-Julian Oscillation were prepared with the desired quantities. The daily rainfall data of 48 satellite stations related to the three months of December, January and February during the forty-year statistical period (1980 to 2020) were obtained from the National Meteorological Organization. The distribution of these stations in the country is shown in **Figures 1-3**. It should be noted that due to the lack of a number of stations in the country and the weakening of the quality of the graphic output of zoning, the number of processing networks was increased by using the IDW interpolation method and the resolution of the studied points increased significantly. IDW interpolation is one of the important methods whose purpose is to interpolate and determine the amount of a parameter between two measured points. This work is also done according to the neighboring points and by averaging the sample points that are located around each unknown point. The data used in this research, with a spatial separation of one degree, are related to the wind field components, geopotential height, sea level pressure, temperature and humidity for the months of December, January and February 1980 to 2020, the average maps of The NCEP/NCAR daily norms of these committees were received and produced simultaneously with the clusters of eight phases as well as the average daily data of long-wave radiation from the top of the atmosphere from 1980 to 2020 with a spatial resolution of 2.5 degrees. In order to emphasize the role of the MJO, these anomalies are passed through a 30- to 60-day Lenxos inter-pass filter with 49 weighting factors. Finally, using the RMM index, based on which the activity period of each MJO event is divided into eight different phases, the average of these anomalies in each phase has been calculated and analyzed. In the second method of the research, by implementing the MM5 numerical model, the characteristics of different MJO phases have been simulated over a region including Southwest Asia and important parts of the Indian Ocean. In this regard, to reduce and eliminate the MJO effect, the initial pattern of the horizontal wind field between latitudes of five to 15 degrees north of the target network has been changed and then the model has been implemented. The results show that in the sixth and seventh phases of the MJO, with the reduction of geopotential height anomalies of the mid-level of the atmosphere, Strengthening of moisture fluxes and hot and humid currents from the Indian Ocean, strengthening of the divergence of the current at the top and its convergence at the bottom of the atmosphere and the upward movements of the air, a noticeable increase in conditions suitable for rainfall has occurred in parts of the south and southeast of the country. On the other hand, in the third, fourth and to some extent the fifth phases of MJO, with the reverse change of all the mentioned factors, there has been a noticeable decrease in the suitable conditions for rainfall in the mentioned areas. Pearson's correlation coefficient is one of the parametric statistical tests that represent the degree of linear regression relationship between two variables, which is denoted by r, whose value varies between +1 and –1. Pearson's correlation coefficient for a statistical sample with n pairs of data [16] {display style (X_{i},Y_{i})} is defined as follows:

Table 1. The number of days of phases one to eight of the Madden-Julian Oscillation under the condition of a sequence of 7 days or more (1980-2020).

phase	**8**	**7**	**6**	**5**	**4**	**3**	**2**	**1**
number of days	140	178	157	125	126	130	79	75
number of period	16	20	19	15	14	16	11	9

$$r_{xy} = \frac{(\sum x - \bar{x})(\sum y - \bar{y})}{\sqrt{\sum x^{r} \sum y^{r}}} \quad (3)$$

If the correlation coefficient is positive, the relationship between the two variables is direct, and if it is negative, the relationship between the two variables will be inverse [17]. In the next step, the studied parameters related to each of the MJO phases were extracted and prepared based on **Table 1**. Abnormality maps of

the aforementioned atmospheric parameters were calculated for each of the MJO phases compared to the average of 40 years, and maps related to each phase were prepared and analyzed separately. Here it is necessary to explain the abnormality of each parameter in each of the phases (q_{an}) including the difference between the average of that parameter in each phase (q_{ph}) with a forty-year average (from 1980 to 2020) of December, January and February. It will be the same amount. If it was greater than zero, it indicates a positive abnormality, and if it was less than zero, it indicates a negative abnormality [18].

$$q_{an} = q_{ph} - q_{3mon} \quad (4)$$

According to the output of the desired models of this research, in addition to statistical and synoptic discussion and the effects of MJO phases on other atmospheric systems and external links affecting Iran's climate, at the end of the output, the obtained results are plotted in the form of zoning maps, which we will show and explain in the conclusion section. Considering the importance of analyzing the precipitation data and other desired parameters, the output of this research will be the direct and indirect effects of the Madden-Julian oscillation phases on Iran's climate elements, as well as the interaction of the surrounding atmospheric systems and the pressure and wind fields and the simultaneous phases of Madden-Julian can show a purer effect of this important atmospheric event on the water and soil area of Iran. Another part of the data and analyzed in this research is the Wheeler chart data in the format (NC) and graphical display of interest, whose indicators were evaluated and discussed during the years 1980 to 2020. We got Madden-Julian from it and the verification and the final results of the work required a lot of these data, and definitely still in all the research of the world of science, the Wheeler diagram and the OLR data are still considered to be the leading data of Madden-Julian's Oceanic Atmospheric Oscillation investigation, which is shown below in the output.

3. Discuss

As discussed in the previous section about data mining and data processing, the country's daily rainfall data was analyzed in the period from 1980 to 2020, and finally, after applying data optimization filters, the output of Iran's rainfall zoning was The use of Arc Gis software was produced separately for all eight phases, which we will discuss in the following. According to the output of the map in **Figure 1**, which shows the irregularity of Iran's rainfall in phase 1 of Madden-Julian Oscillation, the distribution of rainfall in the conditions of phase one. It can be seen with a variety of fluctuations, among which the share of rainfall and abnormality of rainfall in the southwestern and southern regions of Iran, especially The region of Fars, Hormozgan, West Kerman and Bushehr provinces is more and it is significantly distinguished from other regions of Iran. In the region of the Caspian coast, the main reason for the rainfall is different from the rainfall in other regions of Iran, and it is not discussed in this analysis. In **Figure 2**, Iran's rainfall anomaly shows in phase 2. Compared to phase 1, the precipitations are weakened and uniformly weaker in most abnormal areas. **Figure 3** shows the irregularity of Iran's rainfall in the 3rd phase of Madden-Julian Oscillation. The significance of precipitation is limited and almost local. In phase 3, there is no precipitation in Iran, and obviously, with the beginning of the positive phase of Madden-Julian Oscillation, which includes phases 3, 4, 5, and 6, the changes in precipitation in Iran are different from the negative phases (1, 2, 7, 8). Its changes relative to each other can be considered. In **Figures 4 and 5**, rainfall anomalies are still weak and spotty at the level of the country. In **Figure 6**, which represents the irregularity of Iran's rainfall in the 6th phase of Maden Julian Oscillation, rainfall can be seen in the western and southwestern regions of Iran tangent to the Zagros mountain range, where the provinces of Kurdistan, Kermanshah, Ilam, Khuzestan, Lorestan, Fars, Bushehr, Chaharmahal and Bakhtiari. It has affected Kohgiluyeh and Boyer Ahmad, Hamedan and Markazi in a clear way. In **Figure 7**, most of the rains occurred in the southern half of Iran. Sistan and Baluchistan provinces, south Kerman, Hormozgan, Bushehr, Kohgiluyeh

and Boyer Ahmad, Chaharmahal and Bakhtiari, Khuzestan, Ilam, Lorestan, Fars and Bushehr are affected by the seventh phase of MJO, among which Hormozgan and Fars provinces have more anomalies than other southern provinces. In **Figure 8**, a stronger anomaly in the west, southwest and in south of Iran, it can be seen that the share of the provinces of West Hormozgan, Bushehr, Kohgiluyeh and Boyer Ahmad, Chaharmahal and Bakhtiari, Kurdistan, Kermanshah, Ilam, Khuzestan, Ilam, Lorestan, Fars and Bushehr in this anomaly is different from other provinces. The 24-hour average cloudiness maps of Iran in the 40-year period of 1980-2020 were separately averaged and produced in 8 phases, the purpose of which is to verify the effects of the Madden-Julian fluctuation on various atmospheric parameters and a more detailed analysis of the studied indicators. In this group of maps, the amount of cloudiness in the 24-hour period was checked on average, which was compared with the OLR maps and a conclusion was drawn (**Figure 9**). In the phase 1 model cloud cover can be seen in most regions of the country, which is consistent with the phase 1 precipitation maps and is a seal of approval in the verification of precipitation maps. In the phase 2 model, the amount of cloudiness in the country is more limited than in phase 1, and most of the cloudiness is seen in the northern half of Iran. In the phase 3 model, which indicates phase 3, the cloudiness is partially reduced from its previous phase and the cloudiness level of the Iranian sky is more limited. In models 4 and 5, which indicate phases 4 and 5, exactly in line with the precipitation maps of the country, the sky does not have the cloud cover caused by the Madden-Julian oscillation, and in these two phases, it is not much affected by the MJO. In model 6, which is related to phase 6, again with the change of the activity of the Julian oscillation from a positive to a negative phase, the cloudiness level has significant changes in the sky of Iran. And it is proven to be exactly in line with the precipitation maps of MJO activity in Iran in phases 6, 7 and 8. In model 8, which represents the 8th phase, cloudiness has intensified and strengthened while spreading in the sky of Iran in the western region of Iran in the provinces of Kurdistan, Kermanshah, Ilam, Hamedan, Lorestan and the western area of Alborz.

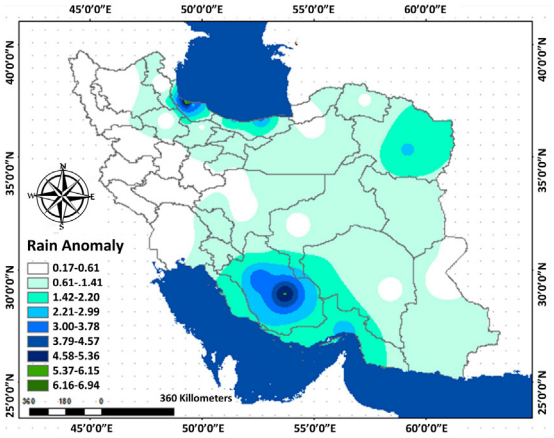

Figure 1. Iran's rainfall anomaly map in phase 1 of Madden-Julian Oscillation.

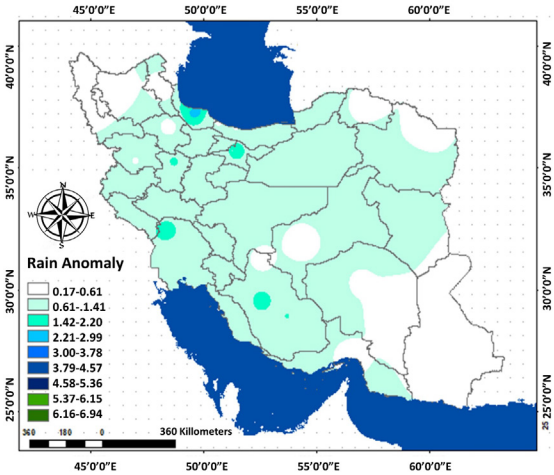

Figure 2. Iran's rainfall anomaly map in phase 2 of Madden-Julian Oscillation.

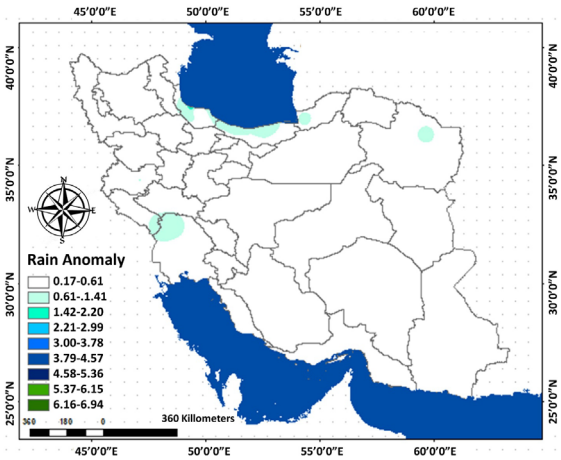

Figure 3. Iran's rainfall anomaly map in phase 3 of Madden-Julian Oscillation.

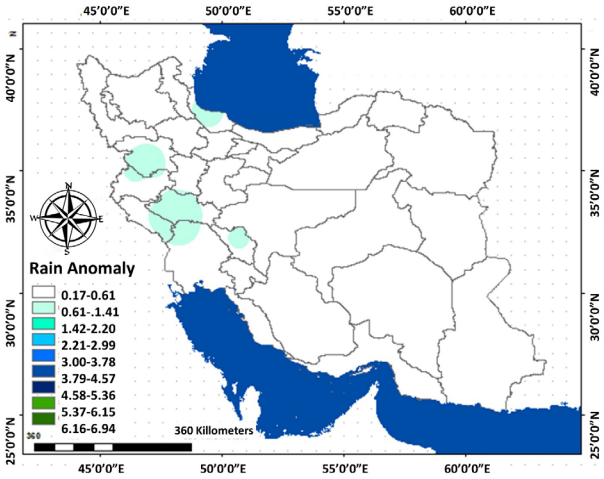

Figure 4. Iran's rainfall anomaly map in phase 4 of Madden-Julian Oscillation.

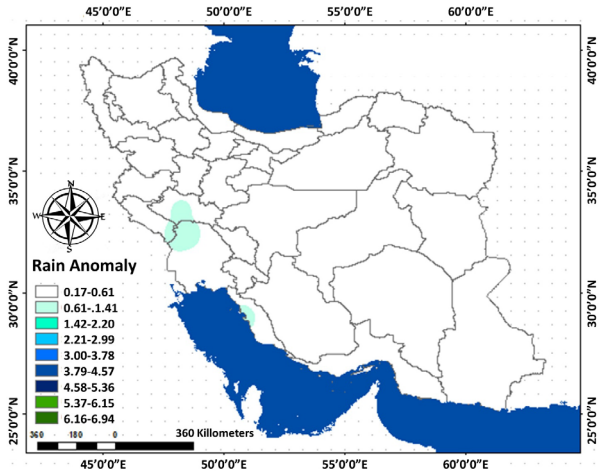

Figure 5. Iran's rainfall anomaly map in phase 5 of Madden-Julian Oscillation.

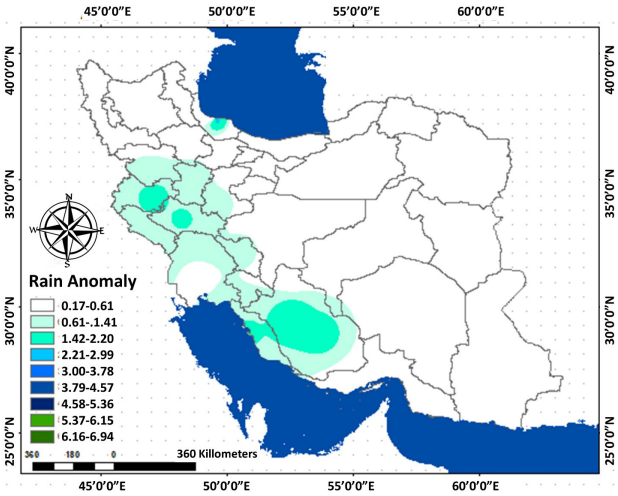

Figure 6. Iran's rainfall anomaly map in phase 6 of Madden-Julian Oscillation.

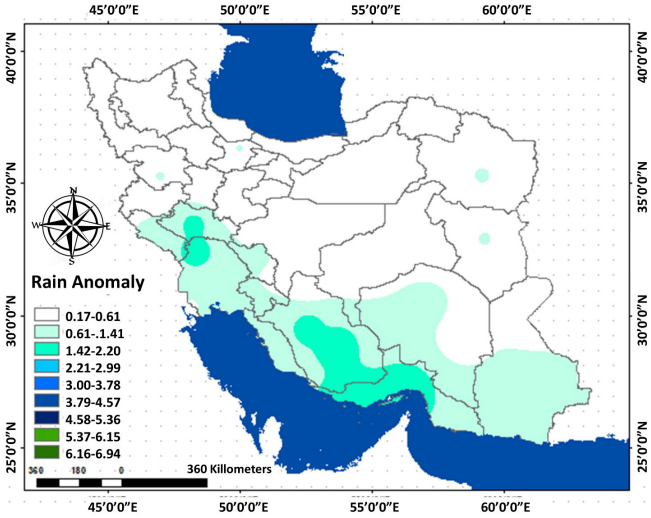

Figure7. Iran's rainfall anomaly map in phase 7 of Madden-Julian Oscillation.

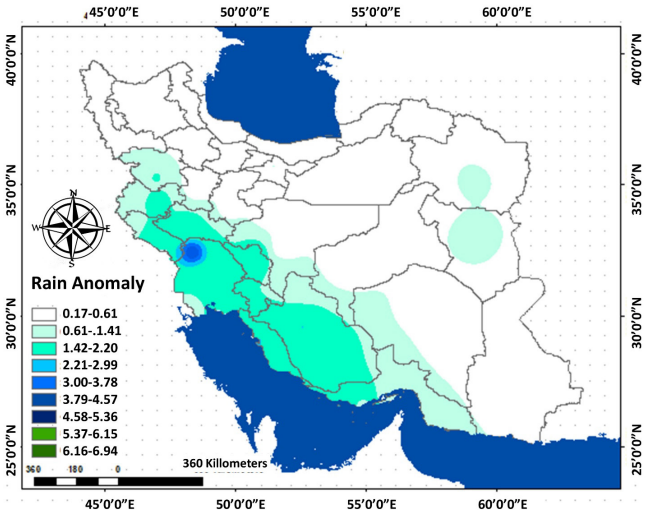

Figure 8. Iran's rainfall anomaly map in phase 8 of Madden-Julian Oscillation.

Interpretation of the mutual effects of the currents and the eight phases of the MJO

In this part of the article, we intend to interpret the mutual effects of jet streams and the eight phases of MJO, which is one of the most important factors of rainfall anomalies in the region. **Figure 10** shows the long-term average of the orbital wind component at the level of 200 m bar for DJF months from 1980 to 2020. In these maps, Iran is located between the two rivers of Asia and North Africa. And the connection and discontinuity between these two rivers can have a very important effect on Iran's rainfall [19].

During the occurrence of positive phases and when convection takes place in the region of Indonesia, the occurrence of abnormal events at the peak of convection with the divergence and anomalies of the upper levels winds cause the connection and continuity of the Asian and North African jets [20]. Due to the importance of the entry and exit of the rivers, which have positive and negative convection effects, these conditions can have a great effect on the behavior of phase precipitation in the region of Iran. In these situations, when the jets are connected to each other discretely or continuously. The impact of the behavior of the jets and the effects caused by them are weakened or strengthened. As can be seen in **Figure 11**, the different phases of Madden-Julian have an effect on the wind field of the upper atmosphere and as a result on the winds and their behavior.

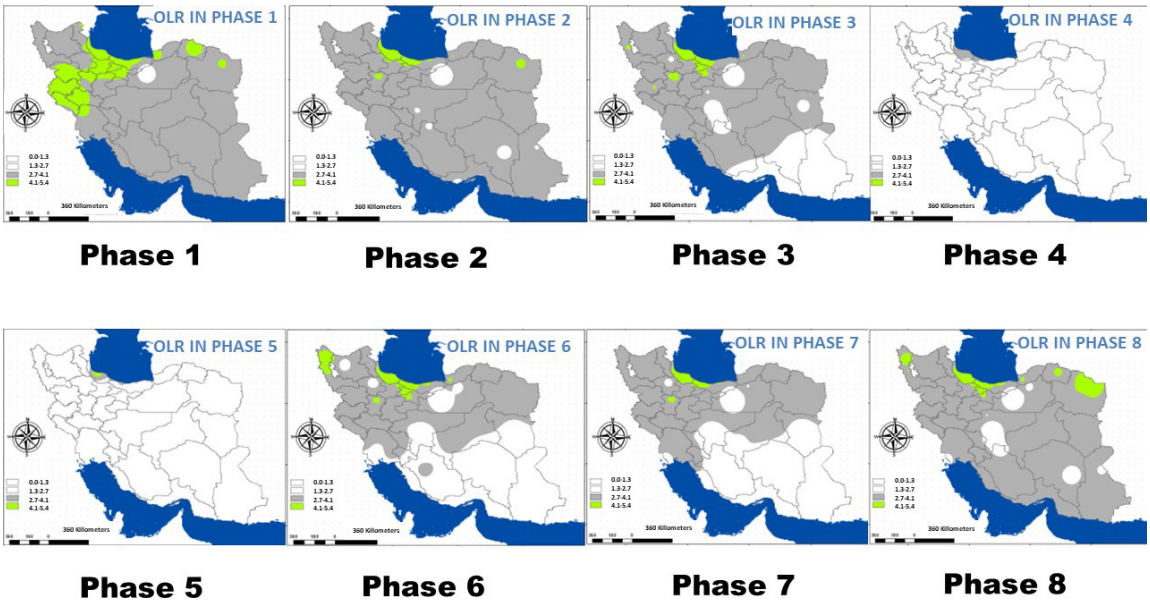

Figure 9. Clouds map of Iran during Madden-Julian oscillation phases (1980-2020).

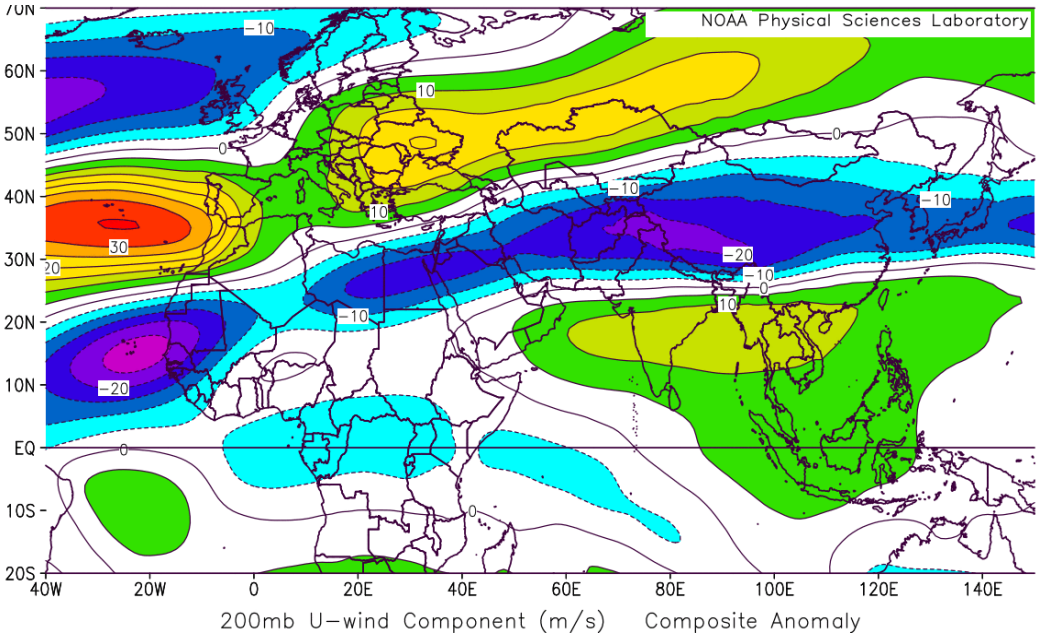

Figure 10. Long-term anomaly (between 1980 and 2020) of wind orbital component at 200 hPa level for DJF months and subtropical jet stream climatic position and average wind orbital component in the positive phases of MJO. (NOAA Physical Scinces Laboratory)

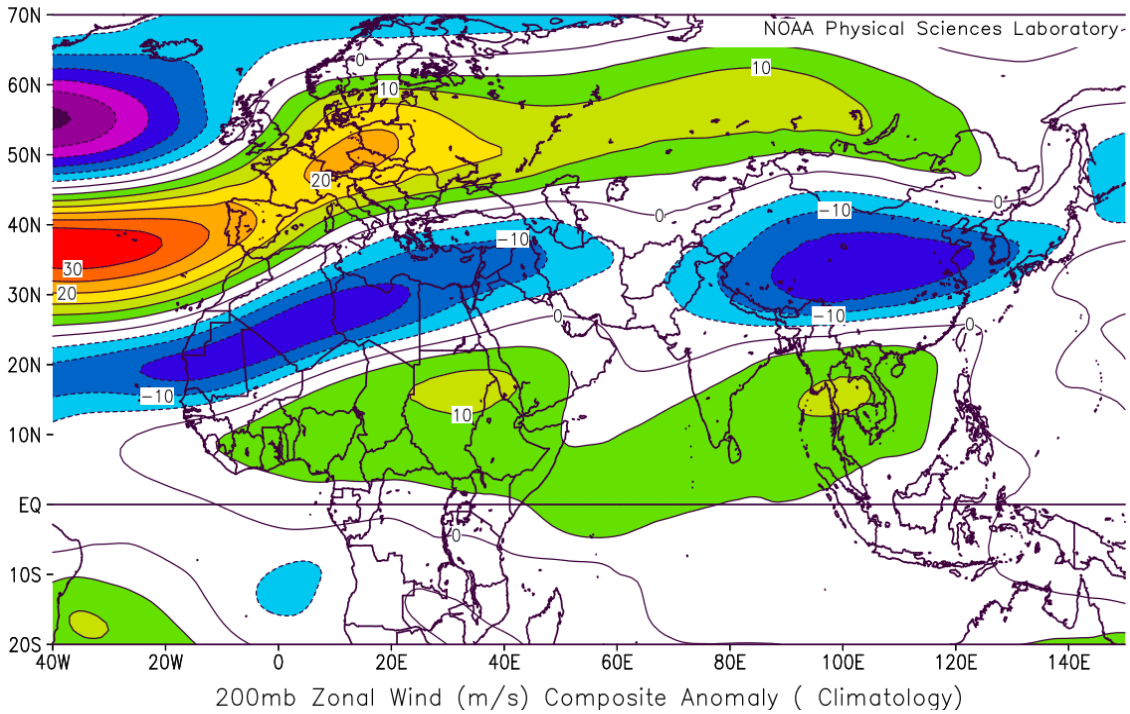

Figure 11. Long-term anomaly (between 1980 and 2020) of wind orbital component at 200 hPa level for DJF months and subtropical jet stream climate position and mean wind orbital component in the negative phases MJO. (NOAA Physical Scinces Laboratory).

The analysis of the anomaly of the meridional wind component at the level of 200 m bar (**Figure 9**) fully confirms that during the occurrence of positive phases of the MJO, the North African anomaly in the exit region of the jet and the wind fields in this region caused the jet to expand to the Indian region. The final connection of these two rivers has brought about this issue, which will cause Iran to leave the area of influence of the North African jet stream and the unstable conditions in Iran will disappear, in which we are witnessing a calm and stable pattern in Iran's air. But on the contrary, as **Figure 10** shows, when the anomalies of the upper atmosphere and the winds of this region are disturbed by convection in the negative phases of Madden-Julian, Iran is again located in the exit region of the North African Wind. It becomes favorable for the occurrence of precipitation in Iran, and in the conditions of the presence of precipitation systems, we will witness the strengthening of their precipitation behavior in Iran.

4. Conclusions

Phases with a sequence of 7 days and a component above 1 were used as the basis for clustering all eight phases, and by calculating the abnormality of each phase compared to its long duration in the DJF time frame and by passing the data through the 30-60 day intermediate filter, zoning each phase was produced in latitude 25 to 40 degrees north and longitude 44 to 63 east. With the investigations carried out and the output of the models and finally the production of zoning related to Iran's rainfall anomalies in the eight phases of the MJO, the country's daily rainfall data were analyzed in the period from 1980 to 2021, which finally after applying data optimization filters, Iran's precipitation zoning output using Arc Gis software were produced separately for all eight phases. According to the outputs, the distribution of rainfall in the conditions of phase one can be seen with a variety of fluctuations, among which the share of rainfall and rainfall anomalies is greater in the southwestern and southern regions of Iran, especially in the regions of Fars, Hormozgan, West Kerman and Bushehr provinces. It is significantly different from other regions of Iran. In the region of the Caspian coast, the main reason for the rainfall is

different from the rainfall in other regions of Iran, and it is not discussed in this analysis. Iran's rainfall anomaly in phase 2 has weakened compared to phase 1 rainfall, and it can be felt that the anomaly is weaker in most areas. Iran's rainfall anomaly in phase 3 of Madden-Julian Oscillation has shown, we have significantly limited rainfall and almost locally. In phase 3, there is no rainfall in Iran, and obviously, with the beginning of the positive phase of the Madden-Julian Oscillation, which includes phases 3, 4, 5, and 6, the changes in precipitation in Iran are different from the negative phases 1, 2, 7, and 8, and their changes can be considered in relation to each other. Eliminating the boundary between spatial-temporal scales and a deeper understanding of distant planetary systems is always an important challenge that the scientific community is facing. Undoubtedly, progress in medium-range and seasonal weather forecasting and our understanding of large-scale weather patterns and the identification of specific causes of their occurrence rely on our deep understanding of the behavior of atmospheric-oceanic patterns and their relationship with each other. Based on the direction of this research, the investigation of precipitation anomalies associated with the eight phases of MJO during the period of December, January and February 1980 to 2020 showed that the precipitation behavior of each of these phases is different from each other. These abnormalities are variable in each phase. At the end of this research, the results were obtained that the effect of MJO on Iran's rainfall is clear and according to the filters applied in this research, it can be concluded with a high percentage of confidence that this phenomenon is formed in the west of the Indian Ocean and towards the east. It is most active in the Indonesian region (phase 5) and weakens and gradually subsides in the middle of the Pacific Ocean (phase 8). The existence of strong and negative anomalies of the long wave radiation of the OLR output from the top of the atmosphere in the MJO convection zone. These anomalies are mainly due to the fact that in the convection zone, very huge convective clouds are formed and spread, whose peaks extend to the east and have weak long-wave radiation, which is evident in the path of OLR images. The presence of two rotating cells at the 850 hpa level on both sides of the equator and around the convection zone. These two cells in the convection zone cause the convergence of western winds, and the eastern winds located in front of the convection zone also help to strengthen this convergence [6]. Based on the results, it seems that the effects of the MJO include the regions of Iran, which is the result of the interaction between the MJO and other large-scale atmospheric circulations, especially the North Atlantic Oscillation (NAO) [4]. This fluctuation in phases 1, 2, 7, and 8 is clearly effective in some areas of Iran, and in phases 3, 4, 5, and 6, which are known as positive phases, it has a debilitating effect and rainfall is significantly limited. Considering the problem of water shortage in the country and the importance of planning in this area, it is very important to reveal the zoning pattern of the various effects of this fluctuation in the country. To complete these results, the frequency of dry and wet periods with positive and negative phase events respectively MJO is correlated. Thus, in the positive phase, the possibility of drought and in the negative phase of MJO is more likely to occur periodically. Finally, it can be concluded that Madden-Julian Oscillation indirectly and in the form of an intensifying and modulating engine has an effect on Iran's climate elements such as precipitation, humidity, cloudiness, wind and drought, and each of its phases in different ways in the water and Iran's weather are influential. Considering the outstanding research of this research on the effects of the Julian Oscillation on Iran, it was tried to examine the effects as purely as possible and the effects of other systems were removed from it, and this result was achieved to a high extent. In the end, it is hoped that the analysis of different phases and zoning produced by this research will be a light for

the country's macro-planning and development in the direction of territorial improvement and sustainable development.

Conflict of Interest

There is no conflict of interest.

References

[1] Hejazizade Begum, Zahra. Sadaqat, Mehdi. 2018. Digital tracking of cyclones in the Middle East during the cold period of the year: natural geography researches (former geographical researches), 41st fall of 2018, number 69.(http://ensani.ir/fa/article/226106/)

[2] Alamzadeh, Sh., Ahmadi Gievi, F., Mohbalhajeh, A. R., and Nasrasafhani, M. A., 1392, dynamic-statistical analysis of the mutual effect of the North Atlantic Oscillation (NAO) and Madden-Julian Oscillation (MJO): Geophysical Journal, 64-80(https://www.ijgeophysics.ir/article_39526.html)

[3] Quaid Amini Asadabadi, H., and Nazemalsadat, M. J., 1391, Evaluation of Madden-Julian Oscillations on the occurrence of daily rainfall in Sistan and Baluchistan and Fars Provinces: Ab and Khak Journal, 1383-1372, 6. (https://jsw.um.ac.ir/article_36596.html)

[4] Nasr Isfahani, M., Ahmadi Givi, F., 1389. Effect of Indian Ocean Convection on Some Meteorological Committees in Southwest Asia. Proceedings of the 14th Iran Geophysical Conference, Institute of Geophysics.(https://journals.ut.ac.ir/article_70987.html)

[5] Abadi, R.S., Soori, M., 2017. A study of the impacts of the MJO on atmospheric circulations and winter precipitation in Iran (Persian), Iranian Journal of Geophysics, 11(1), 49-65. (https://www.ijgeophysics.ir/article_46715.html#ar_info_pnl_cite)

[6] Ahmadi Givi, Farhang and Mohib al-Hajjah, Alireza and Ghazanfari, Abolqasem, 2008, Studying the distribution of humidity and precipitation over Iran in the winter of 2006 and its possible relationship with the circulation in the Indian Ocean(https://civilica.com/doc/72702/)

[7] Barlow, M., Wheeler, M., Lyon, B., et al., 2005. Modulation of daily precipitation over southwest Asia by the Madden-Julian Oscillation. Monthly Weather Review. 133, 3579-3594.

[8] Bond, N.A., Vecchi, G.A., 2003. The influence of the Madden-Julian oscillation on precipitation in Oregon and Washington. Weather and Forecasting. 18, 600-613.

[9] Cassou, C., 2008. Intraseasonal interaction between the Madden-Julian Oscillation and the North Atlantic Oscillation. Nature. 455, 523-527.

[10] Henderson, S.A., Maloney, E.D., Barnes, E.A., 2016. The influence of the Madden-Julian Oscillation on northern hemisphere winter blocking. Journal of Climate. 29, 4597-4616.

[11] Jones, C., 2000. Occurrence of extreme precipitation events in California and relationships with the Madden-Julian Oscillation. Journal of Climate. 13, 3576-3587.

[12] Jones, C., Waliser, D.E., Lau, K.M., et al., 2004. Global occurrences of extreme precipitation and the Madden-Julian Oscillation: Observations and predictability. Journal of Climate. 17, 4575-4589.

[13] Jones, C., Carvalho, L.M.V., 2010. Spatial intensity variations in extreme precipitation in the contiguous United States and the Madden-Julian Oscillation. Journal of Climate. 25(14), 4898-4913.

[14] Johnson, N.C., Collins, D.C., Feldstein, S.B., et al., 2014. Skillful wintertime north American temperature forecasts out to 4 weeks based on the State of ENSO and the MJO. Weather and Forecasting. 13, 23-38.

[15] Hendon, H.H., Salby, M.L., 1994. The life cycle of the Madden-Julian Oscillation. Journal of the

Atmospheric Sciences. 51, 2225-2237.

[16] Kalnay, E., Kanamitsu, M., Kistler, R., et al., 1996. The NCEP/NCAR 40-year reanalysis project. Bulletin of the American Meteorological Society. 77(3), 437-472.

[17] Lin, H., Brunet, G., Derome, J., 2009. An observed connection between the North Atlantic Oscillation and the Madden-Julian oscillation. Journal of Climate. 22, 364-380.

[18] Lin, H., Brunet, G., Mo, R., 2010. Impact of the Madden-Julian Oscillation on wintertime precipitation in Canada. Monthly Weather Review. 138, 3822-3839.

[19] Madden, R.A., Julian, P.R., 1972. Description of global-scale circulation cells in the tropics with a 40-50 day period. Journal of the Atmospheric Sciences. 29, 1109-1123.

[20] Climate Plotting and Analysis Tools [Internet] [cited 2023 Mar 27]. Available from: https://psl.noaa.gov/data/getpage/

BILINGUAL PUBLISHING GROUP

Journal of Atmospheric Science Research
https://journals.bilpubgroup.com/index.php/jasr

ARTICLE

Crucial, But not Systematically Investigated: Rock Glaciers, the Concealed Water Reservoirs of the Himalayas: An Opinion

***Sheikh Nawaz Ali*[1*], *Pratima Pandey*[2*]**

[1] *Birbal Sahni institute of Palaeosciences, Lucknow, 226007, India*
[2] *Indian Institute of Remote Sensing, Dehradun, 248001, India*

ABSTRACT

The current article is an opinion on the sensitivity of high mountain regions which are the most fragile, sensitive and vulnerable to ongoing climate change. Its impacts are especially severe on the high mountain communities owing to their weak socio-economic profile, limited livelihood resources and agricultural land. The melting of glaciers and changes in the snow cover under the climate change scenario is leading to the scarcity of freshwater supplies, affecting both local and downstream communities. Changes in the precipitation patterns have been suggested to cause droughts, impact restricted agriculture, and limit the availability of water for domestic use. Additionally, the high mountain areas contain distinct flora and fauna, and climate change is not just altering them, but also has resulted in biodiversity loss as species are unable to adapt to the changing climate. Because of its higher altitudes and semi-arid to arid climate, the consequences of climate change are more evident in the higher Himalayas. Climate change is affecting the availability of key resources, such as freshwater and agriculture and pasture lands, resulting in food and water insecurity and their reliance on imports from other regions. As a result, high mountain communities in the Himalayas are progressively shifting to higher glacier valleys in search of suitable cultivable land with adequate irrigation. People are engaging in agro-pastoral activities around thermokarst lakes (Oasis) atop rock glaciers as part of this endeavour. Such actions underscore the crucial role of rock glaciers in dealing with and adjusting to the consequences of climate change. Despite its relevance, rock glacier research in the Himalayan region is still in its infancy. The purpose of this work is to emphasise the significance of these major climate-resilient water resources, as well as the methodology that must be adopted for their systematic and compressive investigations.

Keywords: Climate change; Rock glaciers; Evolving agricultural practices; Systematic study; Higher Himalayas

*CORRESPONDING AUTHOR:
Sheikh Nawaz Ali, Birbal Sahni institute of Palaeosciences, Lucknow, 226007, India; Email: snawazali@gmail.com; Pratima Pandey, Indian Institute of Remote Sensing, Dehradun, 248001, India; Email: pratima@iirs.gov.in

ARTICLE INFO
Received: 14 March 2023 | Revised: 03 April 2023 | Accepted: 04 April 2023 | Published Online: 13 April 2023
DOI: https://doi.org/10.30564/jasr.v6i2.5541

CITATION
Ali, S.N., Pandey, P., 2023. Crucial, But not Systematically Investigated: Rock Glaciers, the Concealed Water Reservoirs of the Himalayas: An Opinion. Journal of Atmospheric Science Research. 6(2): 33-41. DOI: https://doi.org/10.30564/jasr.v6i2.5541

COPYRIGHT
Copyright © 2023 by the author(s). Published by Bilingual Publishing Group. This is an open access article under the Creative Commons Attribution-NonCommercial 4.0 International (CC BY-NC 4.0) License. (https://creativecommons.org/licenses/by-nc/4.0/).

1. Introduction

Rock glaciers are landforms characterized by the presence of rock debris intermingled with ice, resulting in the formation of a frozen mass that moves down-slope due to gravity. They have been referred to as the complex shallow groundwater reservoirs/systems of the high mountain areas due to their hydrological significance [1]. The rock glaciers which are the most characteristic landforms of mountain permafrost, are typically found in high-mountain environments. Rock glaciers are usually found in permafrost areas, where the frozen ground serves as a natural barrier to water movement, forcing it to accumulate and freeze among the rock debris. Ice build-up causes the rock debris to become unstable and slowly flow downhill, producing the distinctive tongue-like morphology. The resilience of these ice-rich bodies to climate change makes them a key water management resource, with implications for future freshwater management if the glacier ice volume shrinks by about 77% (expected) by the end of the century. While there is a lot of data on the effects of climate change on glaciers and snow melt, knowledge concerning the storage and water discharge behaviour of permafrost-influenced landforms such as rock glaciers remains limited [2,3]. The condition is deeply worrying in mid-altitude areas (below 4000 masl), where complete glacier ice loss is predicted by the end of the century [1,4].

The situation become more critical for the High Mountain Asia region, because under the high-end climate model simulations (RCP8.5), the warming is expected to be more than 2 °C (global average) by the end of the 21st century resulting in glacier ice loss of ~95% [5]. **Figure 1** displays the Hindukush-Karakoram-Himalaya region susceptible to climate change. The contemporary glacier ice loss and the decrease in snow cover associated are already being witnessed in a number of catchments in this region, particularly during the spring and early summer [6-8]. This situation creates a strong need for climate adaptation measures in the high mountain area of Himalayas especially the ones that experience a semi-arid to the arid climate and depend largely on the glacier and snow melt for their domestic purposes and livelihoods. People have started engaging in agro-pastoral activities around thermokarst lakes (Oasis) atop rock glaciers as part of this endeavour [9]. Hence a comprehensive understanding of all components of the high-mountain cryosphere and the associated hydrological cycle is required [5,10]. Considering that rock glacier research in the Indian Himalayan region is in its infancy, the most of the studies are related to creating the rock glacier inventories [11-14].

Previously, rock glaciers were classified using a variety of terminologies, and rock glacier research was generally limited to making and compiling inventories, and identifying them as either intact (rock glaciers with permafrost) or relict (rock glaciers without permafrost or ice) using a simple compositional characteristic [15]. Using remote sensing images, however, discriminating between the two (intact and relict) is extremely difficult. As a consequence, the International Permafrost Association (IPA) developed a rock glacier classification system based on morphological and sedimentological criteria [16]. This system should be adhered to. Furthermore, such studies may be insufficient unless the actual amount of water that is stored in these features is estimated. This would help in better comprehending the hydrological support and, consequently, the significance for high mountain communities to deal with the effects of climate change, in addition to evaluating the potential for their variations in the future. This will also increase our knowledge of the behaviour of rock glaciers in response to continuing climate change, which is something that will continue to be very important for future generations. As a result, it is necessary to combine our scientific resources and efforts in order to methodically research and comprehend the Himalayan rock glacier and their resistance to the anticipated climate change.

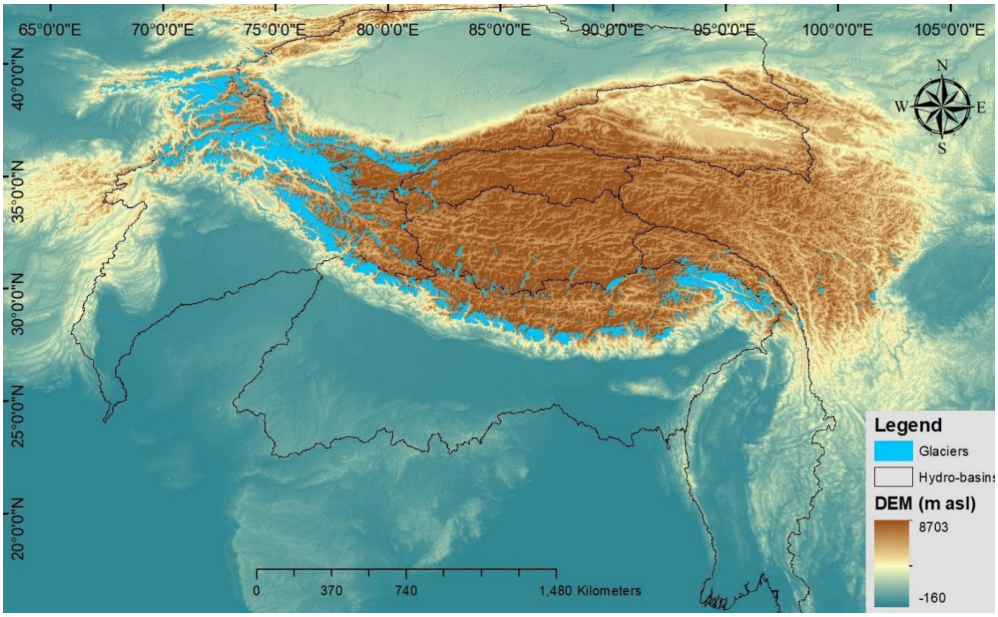

Figure 1. Shuttle Radar Topography Mission (SRTM) digital elevation model (DEM) showing the regional topography and the distribution of glaciers over the Hindukush-Karakoram-Himalaya (HKH) region. The glacier boundaries are derived from the Global Land Ice Measurements from Space (GLIMS) data.

2. Rock glacier classifications

With the recognition of rock glaciers as an integral part of the cryosphere, they have been categorized based on numerous characteristics such as morphology, geometry, activity, topographical association, and origin [17]. A fundamental classification of rock glaciers has been established based on their dynamic activity and the presence of ice [17,18]. Rock glaciers are classified as active, inactive, or fossils/relict based on their dynamic activity and ice presence [15]. Active rock glaciers contain a large volume of ice and creep downslope by a few centimetres to a few metres annually under gravity [19-21]. Inactive rock glaciers also have permafrost but are static, while relict rock glaciers lack both ice and movement, suggesting the existence of permafrost in the past [22]. Intact rock glaciers refer to both active and inactive rock glaciers [15]. Despite some disagreement about their genesis and formation [23], rock glaciers may be characterised based on their origin and ice presence and are divided into the glacial origin and periglacial origin [24]. Rock glaciers are classified into four types based on their morphological and sedimentological characteristics: 1) Tongue-shaped rock glaciers: These are the most common type of rock glacier and are characterized by a steep front and a long tongue-shaped extension. They typically have a well-defined lateral margin and a distinct accumulation area at the top (**Figure 2a**). 2) Lobate rock glaciers: These are similar to tongue-shaped rock glaciers but have a more irregular shape. They are characterized by a broad and lobate front and may have multiple tongues (**Figure 2b**). 3) Rounded rock glaciers: These have a more rounded shape than tongue-shaped or lobate rock glaciers and are typically smaller in size. They are characterized by a smooth front and a more gradual slope (**Figure 2c**). 4) Blocky rock glaciers: These are characterized by a blocky surface and a jagged, irregular front. They typically have a shallow accumulation area and are found in areas with more fractured bedrock (**Figure 2d**).

The International Permafrost Association (IPA) classification seems more robust as it is based on a combination of morphological and sedimentological characteristics, including the shape of the front, the presence of lateral moraines, the presence of permafrost, and the type of sediment present in the rock glacier [16]. We recommend this system be widely used in the field of permafrost and rock glacier studies to classify and describe different types of rock

glaciers. The classification of rock glaciers based on their connection to other landforms provides a useful framework for understanding the physical processes that shape these landforms and the environmental conditions under which they form. It also highlights the importance of considering the broader landscape context when studying rock glaciers and their role in mountain environments. Following a standard classification will remove the bias and/or incongruity in the data generated. The IPA classification system categorizes rock glaciers into four types discussed below and displayed in **Figure 3**:

1) Glacier-connected (GC): These rock glaciers are connected to a glacier or ice sheet and are often found at the toe of a glacier. They are characterized by a steep front and a long tongue-shaped extension, similar to tongue-shaped rock glaciers in the IPA classification (**Figure 3a**).

2) Talus-connected (TC): These rock glaciers are connected to talus slopes and are typically found on the lower slopes of mountains. They are characterized by a more irregular shape and a front that is often covered in loose rock debris (**Figure 3b**).

3) Glacier forefield-connected (GFC): These rock glaciers are located in glacier forefields, which are areas of newly exposed terrain at the toe of a glacier. They are characterized by a broad, fan-shaped front and may have multiple tongues (**Figure 3c**).

4) Debris-mantled slope-connected (DC): These rock glaciers are located on slopes covered in loose rock debris and are often found in areas with permafrost. They are characterized by a blocky surface and a more irregular shape than other types of rock glaciers (**Figure 3d**).

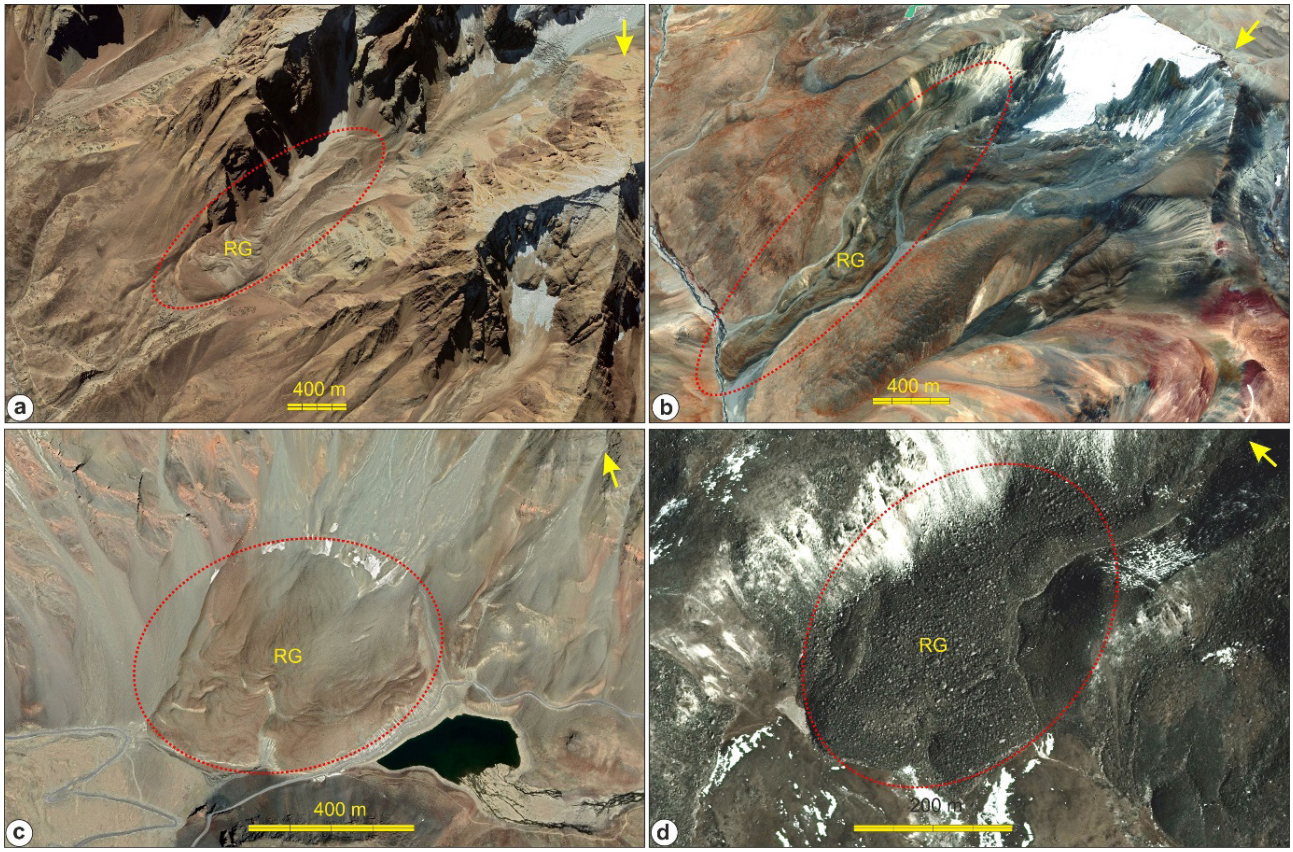

Figure 2. Showing different types of rock glacier (RG) on the Google Earth Pro imagery. a) Tongue-shaped rock glacier; b) Lobate rock glacier; c) Rounded rock glacier, and d) Blocky rock glacier.

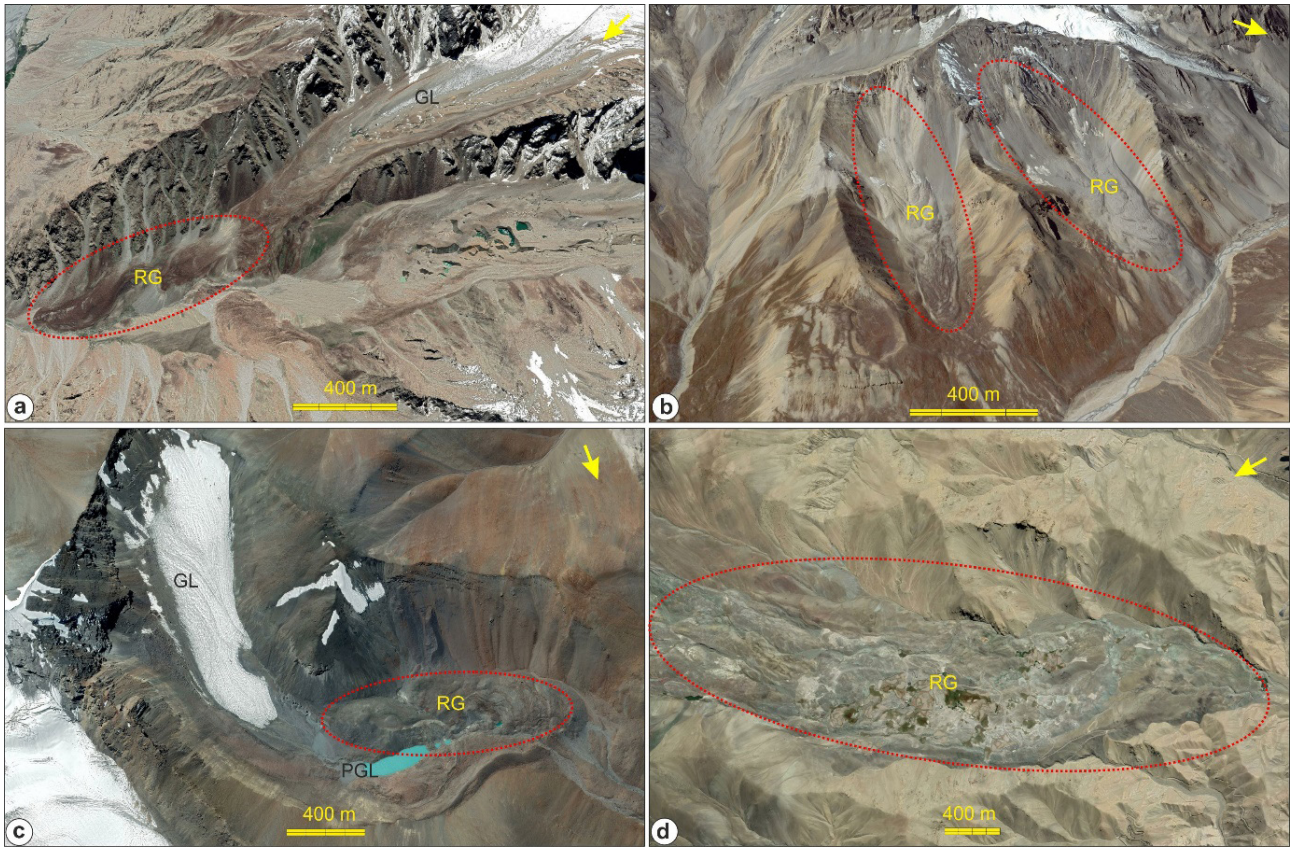

Figure 3. IPA classification is based on different types of rock glacier shown on the Google Earth Pro imagery. a) Glacier-connected rock glacier; b) Talus-connected rock glacier; c) Glacier forefield-connected rock glacier, and d) Debris-mantled slope-connected rock glacier.

Note: RG-rock glacier; GL-glacier and PGL-pro-glacial lake.

3. Systematic rock glacier research

Systematic rock glacier research entails examining the formation, characteristics, hydrological behaviour, and dynamics of rock glaciers at both the local and regional scales, particularly in the context of climate change. As rock glacier research in the Himalayan region is still in its embryonic stage, a properly developed standard strategy for monitoring them, assessing their hydrological behaviour and potential, and evaluating their resilience to climate warming would greatly aid in fostering understanding among policymakers and stakeholders. The characteristics of the rock and ice that make up the glacier, as well as the local geography, geological history, and climate may all be studied in this process. Hence, a multidisciplinary approach is necessary for the proper understanding of these important water reserves (**Figure 4**). The following steps could make up the strategy for investigating rock glaciers:

1) Inventory of rock glaciers: The first and foremost prerequisite for developing understanding is the identification and inventory of the rock glaciers. The ID of rock glaciers, type of rock glacier, origin, and kinematics should all be included in the inventory along with geographical information.

2) Geophysical Investigation: Geophysical investigation is very crucial for comprehending the internal structure and composition of rock glaciers in terms of hydrological perspectives. To ascertain the underlying structure, presence of ice, and depth of bedrock, a geophysical study may be conducted using ground penetrating radar (GPR), electrical resistivity tomography (ERT), and seismic refraction.

3) Topo-climatic characteristics: Rock glaciers are considered as the physical proof or validation of permafrost existence. Permafrost formation is

influenced by a number of topographical factors, including mean annual air temperature (MAAT), sun radiation, and slope aspect. Rock glaciers' topographical climatic and temperature regimes are crucial factors in determining whether or not they can serve as an accurate proxy for permafrost spread. To comprehend the temperature of the subsurface and the composition of rock glaciers, boreholes should be employed extensively.

4) Hydrological significance: A thorough evaluation of the occurrences, characteristics, and internal structure of rock glaciers might also be used to model the percentage of water volume equivalent of rock glaciers for their water reserve capacity in the future.

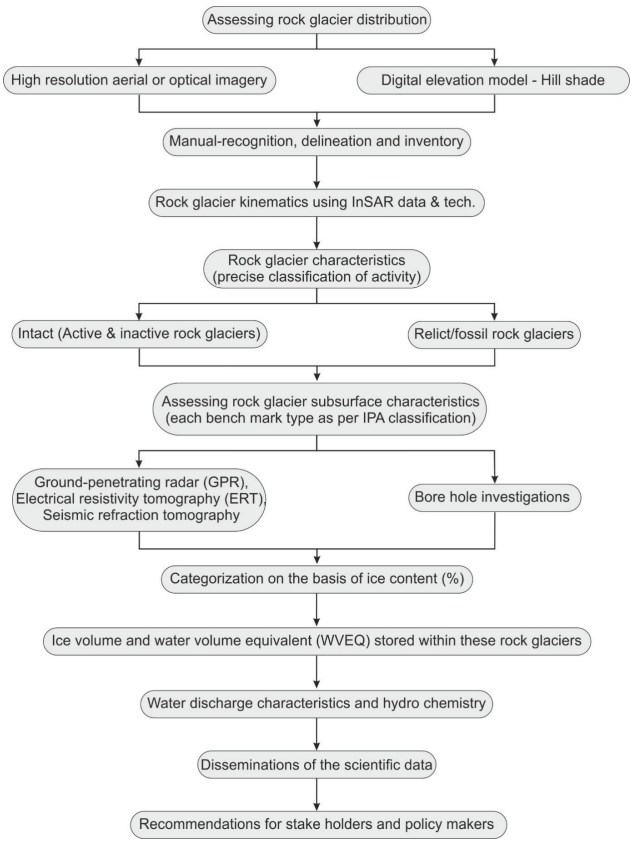

Figure 4. The flowchart shows the strategy and steps required for rock glacier studies.

4. Discussion

Under the ongoing warming scenario, the 0 °C isotherm is and will gradually increase in elevation and result in further melting of the glacier ice, snowpack and permafrost [25]. This is going to affect the mountain hydrology and alter the geo-ecological zones and stress the high mountain areas including communities that generally depend on these water resources. The repercussions of climate change are worrisome in the Himalayas where the future model projections show a warmer and wetter climate, with significant implications for high-mountain glacier cover and glacial lake expansion [26]. In such a situation, the climate-resilient and substantial rock glaciers will act as buffers against these changes. Hence overall, research on rock glaciers is important for comprehending their role in mountain environments, predicting their future behaviour, and managing potential hazards associated with their movement is needed. The key areas of research on rock glaciers in the high mountain Himalayas must include: (1) Mapping and creating rock glacier inventories. Rock glaciers in the Himalayas are often difficult to locate and study due to their remote locations in the rugged terrain and harsh climate. Therefore, researchers need to map and inventory rock glaciers in the region using high-resolution remote sensing imageries and techniques. (2) Understanding the Formation and evolution of rock glaciers because understanding the factors that contribute to the formation and evolution of rock glaciers is important for predicting their future behaviour. Hence the information about the geology, hydrology, and climate conditions that lead to the formation of rock glaciers, as well as the mechanisms that cause them to move needs to be critically investigated. (3) Studying the movement and dynamics of rock glaciers will further help in understanding their behaviour. The rock glacier can move at rates ranging from a few centimetres to several meters per year. Researchers may use various techniques, such as ground-based surveys, remote sensing, and modelling, to monitor the movement and dynamics of rock glaciers. This information is crucial for predicting the potential hazards associated with rock glacier movements, such as landslides and rockfall. (4) Understanding the impacts on water resources is one of the most important factors for societal impli-

cations. Rock glaciers will form an important source of water in mountain environments, as they can act as natural reservoirs and release water gradually over time. Research on the hydrological processes of rock glaciers, including water storage and release, must be conducted in order to comprehend their influence on water resources and guide water resource management strategies, and (5) finally the impact on infrastructure development. Rock glaciers can pose a significant hazard to infrastructure development, such as the construction of roads and buildings, due to their potential for movement and instability. High-resolution maps of rock glaciers and permafrost need to be developed for the categorization of potential hazards associated with rock glaciers to inform infrastructure planning and design.

Estimating the water volume stored in rock glaciers is the most crucial and challenging task, particularly in the Himalayas where many of the rock glaciers are located in remote and difficult-to-access areas (**Figure 5**). As a result, there is a lack of accurate water volume estimates for rock glaciers in the Himalayas. One of the primary reasons for the lack of water volume estimates is the limited data on the internal structure of rock glaciers. Rock glaciers are complex structures consisting of a mixture of ice, rock debris, and water, and their internal structure can vary significantly from one location to another. This makes it challenging to estimate the water volume stored in a rock glacier accurately. Rock glaciers can act as natural reservoirs, storing water in the form of ice and releasing it gradually over time. However, the precise mechanisms by which water is stored and released from rock glaciers are not well understood, particularly in the Himalayas. Despite these challenges, efforts are being made to estimate the water volume stored in rock glaciers in the Himalayas. Remote sensing techniques, such as satellite imagery and aerial photography, are being used to map and inventory rock glaciers in the region, providing valuable data for estimating their water storage capacity.

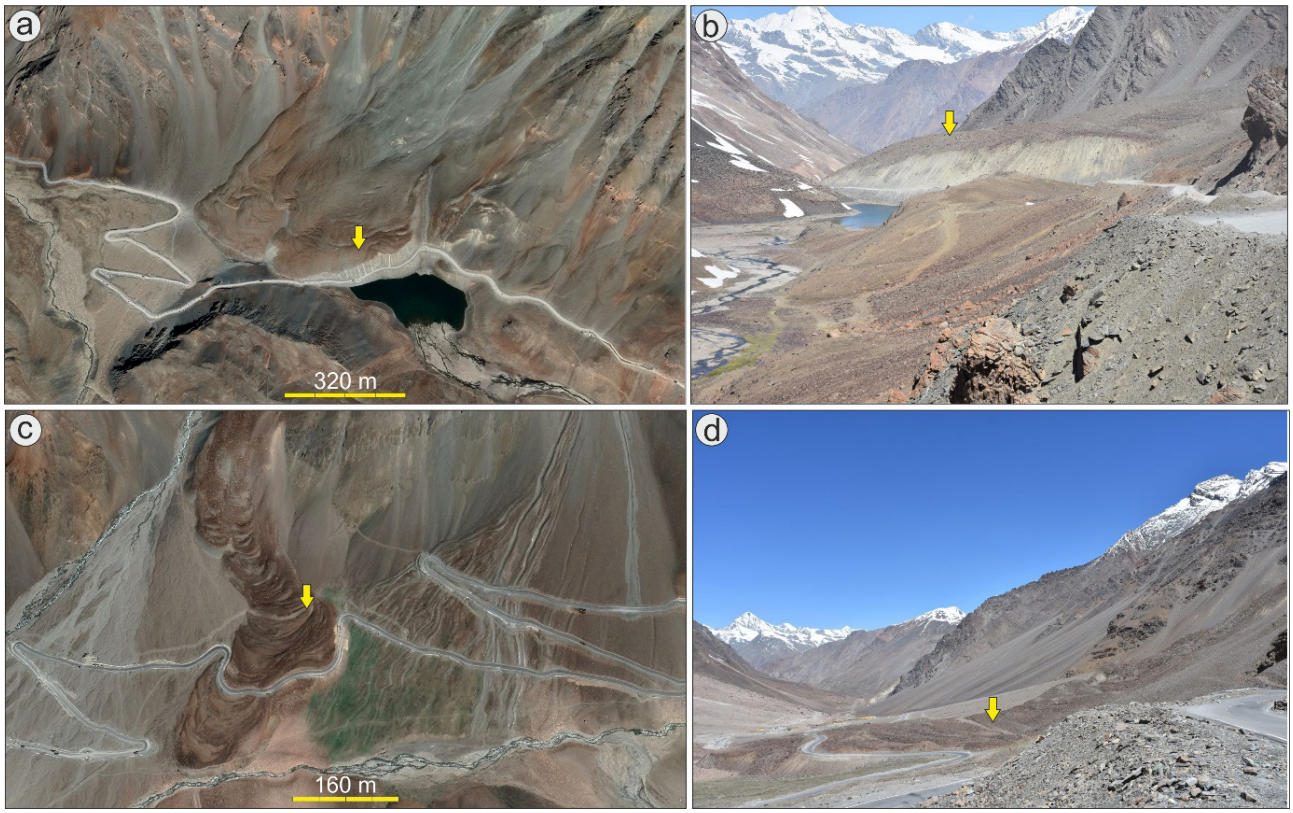

Figure 5. Google Earth images and Filed photographs of two prominent rock glacier in the Bhaga watershed of the western Himalayas, India.

However, ground-based surveys and monitoring programs must be implemented to study the hydrological processes associated with rock glaciers. Till date, the rock glacier water volume equivalent (WVEQ) estimation is being carried out by the empirical thickness-area scaling relations which is a 2-D-area- related statistic [10]. These estimates are crude in nature unless filed-based data are available from different types of rock glaciers discussed in section 2. The volumetric estimates of the ice content in the rock glaciers are also based on assumptions and hence a wide range of ice content is assumed. It ranges from 40%-60% (lowest 40%, mean 50%, and upper limits 60%), but Wagner et al. [1] adjusted the lower bound to 20% to account for the likelihood of less ice content in inactive rock glaciers in the Austrian Alps. This creates a huge difference in the estimation of WVEQ. Therefore, at least some ground-based data on the thickness and ice volume percentages should be made available so that the estimation is genuine. This will include a systematic investigation of different types of rock glaciers like the glacier-connected (GC) rock glaciers, talus-connected (TC) rock glaciers, debris-mantled slope-connected (DC) rock glaciers, and glacier forefield-connected (GFC) rock glaciers.

5. Conclusions

Mountainous regions' cryospheric water supplies are at risk due to climate change. Thus it's important to understand the hydrological cycle as a whole in order to manage these resources. Future global warming may cause rock glaciers to become more significant hydrologically, yet despite their greater climate adaptability than glaciers and potential for beneficial ice accumulation, rock glaciers have received less attention. Systematic investigations of rock glaciers in a changing environment are crucial for improving our knowledge of how to rock glaciers behave in mountain environments and for predicting future behaviour. There aren't many baseline statistics from the Himalayan region, despite it being significant. By studying how climate change impacts rock glaciers, researchers may get a crucial understanding of the potential implications on water supply, natural disasters, and infrastructure. Use of this information is necessary to develop effective management and adaption strategies for the changing climate.

Conflict of Interest

There is no conflict of interest.

Acknowledgements

The authors are thankful to the Directors of Birbal Sahni Institute of Palaeosciences (BSIP), Lucknow and Indian Institute of Remote Sensing (ISRO), Dehradun for providing infrastructure, encouragement and support.

References

[1] Wagner, T., Kainz, S., Helfricht, K., et al., 2021. Assessment of liquid and solid water storage in rock glaciers versus glacier ice in the Austrian Alps. Science of the Total Environment. 800, 149593.

[2] Geiger, S.T., Daniels, J.M., Miller, S.N., et al., 2014. Influence of rock glaciers on stream hydrology in the La Sal Mountains, Utah. Arctic, Antarctic, and Alpine Research. 46(3), 645-658.

[3] Rogger, M., Chirico, G.B., Hausmann, H., et al., 2017. Impact of mountain permafrost on flow path and runoff response in a high alpine catchment. Water Resources Research. 53(2), 1288-1308.

[4] Shannon, S., Smith, R., Wiltshire, A., et al., 2019. Global glacier volume projections under high-end climate change scenarios. Cryosphere. 13, 325-350.

[5] Jones, D.B., Harrison, S., Anderson, K., et al., 2021. Rock glaciers represent hidden water stores in the Himalaya. Science of The Total Environment. 793, 145368.

[6] Ming, J., Wang, Y., Du, Z., et al., 2015. Widespread albedo decreasing and induced melting of Himalayan snow and ice in the early 21st

century. PLoS One. 10(6), e0126235.

[7] Gurung, D.R., Maharjan, S.B., Shrestha, A.B., et al., 2017. Climate and topographic controls on snow cover dynamics in the Hindu Kush Himalaya. International Journal of Climatology. 37, 3873-3882.

[8] Smith, T., Bookhagen, B., 2018. Changes in seasonal snow water equivalent distribution in High Mountain Asia (1987 to 2009). Science Advances. 4, e1701550.

[9] Pandey, P., Ali, S.N., Allen, S., 2022. Rock glacier Oasis: An alternative for agro-pastoralism in a changing environment in the Himalayan cold desert. The Geographical Journal. 188(4), 585-590. DOI: https://doi.org/10.1111/geoj.12468

[10] Jones, D.B., Harrison, S., Anderson, K., et al., 2021. Rock glaciers represent hidden water stores in the Himalaya. Science of The Total Environment. 793, 145368.

[11] Baral, P., Haq, M.A., Yaragal, S., 2019. Assessment of rock glaciers and permafrost distribution in Uttarakhand, India. Permafrost and Periglacial Processes. 31, 31-56.

[12] Pandey, P., 2019. Inventory of rock glaciers in Himachal Himalaya, India using high-resolution Google Earth imagery. Geomorphology. 340, 103-115.

[13] Majeed, Z., Mehta, M., Ahmad, M., et al., 2022. Active rock glaciers of Jhelum basin, Kashmir Himalaya, India. Indian Journal of Geosciences. 76(1), 107-124.

[14] Chakravarti, P., Jain, V., Mishra, V., 2022. The distribution and hydrological significance of intact rock glaciers in the north-west Himalaya. Geografiska Annaler: Series A, Physical Geography. 104(3), 226-244.

[15] Barsch, D., 1996. Rock glaciers: Indicators for the present and former geoecology in high mountain environments. Springer-Verlag: Berlin. pp. 331.

[16] RGIK, 2021. IPA Action Group Rock Glacier Inventories and Kinematics [Internet]. Towards Standard Guidelines for Inventorying Rock glaciers: Baseline Concepts (version 4.2.1). Available from: https://bigweb.unifr.ch/Science/Geosciences/Geomorphology/Pub/Website/IPA/Guidelines/V4/210801_Baseline_Concepts_Inventorying_Rock_Glaciers_V4.2.1.pdf

[17] Martin, H.E., Whalley, W.B., 1987. Rock glaciers: Part 1: Rock glacier morphology: Classification and distribution. Progress in Physical Geography. 11, 260-282.

[18] Wahrhaftig, C., Cox, A., 1959. Rock glaciers in the Alaska Range. Geological Society of America Bulletin. 70, 383-436.

[19] Kääb, A., Kaufmann, V., Ladstadter, R., et al., 2003. Rock glacier dynamics: Implications from high-resolution measurements of surface velocity fields. Eighth International Conference on Permafrost. 1, 501-506.

[20] Berger, J., Krainer, K., Mostler, W., 2004. Dynamics of an active rock glacier (Otztal Alps, Austria). Quaternary Research. 62, 233-242.

[21] Necsoiu, M., Onaca, A., Wigginton, S., et al., 2016. Rock glacier dynamics in Southern Carpathian mountains from high resolution optical and multi-temporal SAR satelliteimagery. Remote Sensing of Environment. 177, 21-36.

[22] Haeberli, W., 1985. Creep of mountain permafrost: Internal structure and flow of Alpine rock glaciers. Mitteilungen der Versuchsanstalt fur Wasserbau. Hydrologie und Glaziologiean der ETH Zurich. 77, 5-142.

[23] Berthling, I., 2011. Beyond confusion: Rock glaciers as cryo-conditioned landforms. Geomorphology. 131(3-4), 98-106.

[24] Haeberli, W., Hallet, B., Arenson, L., et al., 2006. Permafrost creep and rock glacier dynamics. Permafrost and Periglacial Processes. 17(3), 189-214.

[25] Iribarren, P.A., Kinney, J., Schaefer, M., et al., 2018. Glacier protection laws: Potential conflicts in managing glacial hazards and adapting to climate change. Ambio. 47(8), 835-845.

[26] Ali, S.N., Pandey, P., Singh, P., et al., 2023. Intimidating evidences of climate change from the higher Himalaya: A case study from Lahaul, Himachal Pradesh, India. Journal of the Indian Society of Remote Sensing. (In press).

BILINGUAL PUBLISHING GROUP

Journal of Atmospheric Science Research
https://journals.bilpubgroup.com/index.php/jasr

ARTICLE

The Possibilities of Using the Minimax Method to Diagnose the State of the Atmosphere

Elena S. Andreeva

Department of Life Safety and Environmental Protection, Don State Technical University, Rostov-on-Don, 344111, Russia

ABSTRACT

The article is devoted to the discussion of the possibilities of approbation of one of the probabilistic methods of verification of evaluation works - the minimax method or the method of establishing the minimum risk of making erroneous diagnoses of the instability of the planetary boundary layer of air. Within the framework of this study, the task of probabilistic forecasting of diagnostic parameters and their combinations, leading in their totality to the formation of an unstable state of the planetary boundary layer of the atmosphere, was carried out. It is this state that, as shown by previous studies, a priori contribution to the development of a number of weather phenomena dangerous for society (squalls, hail, heavy rains, etc.). The results of applying the minimax method made it possible to identify a number of parameters, such as the intensity of circulation, the activity of the Earth's magnetosphere, and the components of the geostrophic wind velocity, the combination of which led to the development of instability. In the future, it is possible to further expand the number of diagnosed parameters to identify more sensitive elements. In this sense, the minimax method, the usefulness of which is shown in this study, can be considered as one of the preparatory steps for the subsequent more detailed method for forecasting individual hazardous weather phenomena.

Keywords: Minimax method; Dangerous weather phenomena; Atmospheric instability; Boundary layer of the atmosphere; Intensity of atmospheric circulation; Earth's magnetosphere; Geostrophic wind

*CORRESPONDING AUTHOR:
Elena S. Andreeva, Department of Life Safety and Environmental Protection, Don State Technical University, Rostov-on-Don, 344111, Russia; Email: meteo0717@yandex.ru

ARTICLE INFO
Received: 08 March 2023 | Revised: 04 April 2023 | Accepted: 12 April 2023 | Published Online: 18 April 2023
DOI: https://doi.org/10.30564/jasr.v6i2.5519

CITATION
Andreeva, E.S., 2023. The Possibilities of Using the Minimax Method to Diagnose the State of the Atmosphere. Journal of Atmospheric Science Research. 6(2): 42-49. DOI: https://doi.org/10.30564/jasr.v6i2.5519

COPYRIGHT
Copyright © 2023 by the author(s). Published by Bilingual Publishing Group. This is an open access article under the Creative Commons Attribution-NonCommercial 4.0 International (CC BY-NC 4.0) License. (https://creativecommons.org/licenses/by-nc/4.0/).

1. Introduction

As convincingly proved in a number of scientific studies conducted in different years, the unstable state of the atmosphere, more precisely, its planetary boundary layer, is provided by a number of conditions. Among which, of course, both direct telluric or terrestrial origin and cosmic parameters describing aspects of the physical state of the atmospheric boundary layer and part of the so-called free atmosphere above it vertically should be taken into account. Telluric factors are associated with atmospheric processes occurring in the immediate vicinity of the underlying surface and primarily dependent on it. The instability of the atmospheric air layer inside the boundary layer contributes to the emergence and further implementation of a number of dangerous weather phenomena of various scales and damages. In this regard, studies aimed at identifying and diagnosing the state of instability of the atmospheric layer are relevant, since they affect not only the interests of states, but also of humanity as a whole [1-4].

Within the framework of this study, we will consider the problem of probabilistic forecasting of an unstable state of the atmosphere, which a priori will be accompanied by the largest number of hazardous weather phenomena (rainfall, squalls, strong winds, hail, etc.) [1,2,4].

To determine the probability of erroneous decisions when diagnosing the instability of the system - the stability of the state of the atmosphere, we use the minimax method [5-8].

This mathematical estimation method has been used since the 1960s [5] to solve a number of applied problems, if it was necessary to estimate the probability of erroneous and correct solutions in order to minimize incorrect (non-robust) results. Usually, this method was effectively used if the parameters of distributions of random variables of erroneous results are not sufficiently reliable or known. In this regard, based on the difficulties described in a number of scientific publications in accurately identifying the states of the atmosphere, relying on the capabilities of the minimax method, from the list of possible diagnostic parameters of the system under study, we select those that directly characterize the intensity of the circulation of the atmospheric layer, activated by a certain combination of telluric factors: Vertical and horizontal components of geostrophic wind speed (m/s); the actual intensity of atmospheric circulation (hPa/100 km) [9-12]. From the whole variety of cosmic factors affecting the Earth's atmosphere, we will use the index of magnetic activity (points), which allows us to indirectly reveal the fact of the impact of solar activity (high-energy particles of the solar wind) on the electromagnetic field. It seems that the index of magnetic activity makes it possible to sufficiently fully reveal the fact of disturbance of the Earth's electromagnetic field due to the release of high-energy particles during increased solar activity.

2. Materials and methods

The study is based on the daily data of the information array of the NSP NCAR, which includes the values of air temperature. The study is based on daily data from the NSP NKAI information array, which includes the values of air temperature, components of geostrophic wind, cloudiness, precipitation, surface atmospheric pressure, averaged over the period from 1948 to 2005, and presented as a numerical field with sides 60-40° north latitude and 40-60° east longitude. The specified meteorological information was converted into database No. 1 (meteorological fields under various combinations of atmospheric conditions). Database No. 2 included the values of the magnetic activity index (IZMIRAN) in the SI system for individual years, chosen arbitrarily (1984, 1991, 2000, etc.); recurrence (probability) of a number of dangerous weather phenomena, as well as parameters of atmospheric circulation within the lower layer (planetary boundary layer). In particular, the sample for 1948-2005 from meteorological logs TM-1 fixing dangerous weather phenomena made it possible to obtain numerical characteristics of the frequency of occurrence of dangerous weather phenomena, taking into account their intensity and duration. The mentioned recurrences of a number of dangerous weather phenomena were studied over a significant period of time (more than 50 years),

which made it possible to convert them into probabilities. The calculation method was used to obtain the values of atmospheric circulation intensity, expressed as coefficients (Kac circulation indices) [9]. Since all the indicated meteorological characteristics had their own dimensions and ranges of values, a special coefficient was introduced for their consistency, taking these circumstances into account. Database No. 1 was a reference (training within the framework of this model); database No. 2 contained factual information about certain dangerous weather phenomena that developed against the background of instability of the lower layer of the atmosphere (planetary boundary layer). The results of the model operation - a probabilistic assessment of the identified cases of atmospheric instability - were presented in database No. 3. Finally, for diagnosing an unstable state of the atmospheric boundary layer, the minimax method was used in this work - a method for mathematically estimating the probability of making an erroneous/correct diagnosis. Mathematical estimation methods are usually based on the belief that the probability distribution of computational errors is known, or at least the mathematical expectation and covariance matrix of the distributions of these errors are known. However, in practice this does not happen very often. In particular, if there are doubts about the correctness of the calculation results or it is necessary to check the adequacy of the obtained solutions, the minimax method of estimating the available results makes it possible to effectively identify erroneous or, conversely, correctly established solutions. Actually, the minimax method with all its capabilities was described in the monograph by Piter H'yuber in 1984 and began to be used either for mathematical evaluation and analysis of the stability of engineering indicators, or for research in the field of economics (risks of losses, damages, etc.). However, in the framework of meteorological studies, the above method was applied for the first time, since the problem of correctly identifying the states of the atmosphere, more precisely, its planetary boundary layer, for developing forecasts of individual hazardous weather phenomena is very relevant and far from a final solution. The computer implementation of this method is based on net technology using the Visual Basic language.

3. Results

Let us take the dichotomy of states inherent in the boundary layer of the atmosphere as a basis: unstable and stable. Obviously, the transition from an unstable state to a stable one can occur with a certain set of parameters and their configuration, in this case called diagnostic ones [13-20]. Within the framework of the problem being solved, we will assume that the change of diagnosed states of the atmospheric boundary layer occurs in n-dimensional space when the diagnosed parameters x_1, x_2, $x_3 \ldots x_n$ are combined. Making a decision about a particular state of the object under study is reduced to identifying in the diagnostic space a certain boundary surface that divides the indicated space into two regions S_0 and S_1. In this case, these areas are a geometric expression to indicate the possibility of the object under study being in one state or another. So, if, for example, the vector x, including x_1, x_2, ... x_n of diagnostic parameters obtained as a result of observations, belongs to the region S_0 ($x \in S_0$), the diagnosis is D_0 - "the boundary layer of the atmosphere is unstable". If the vector belongs to the region S_1 ($x \in S_1$), we will assume that the boundary layer is stable, which corresponds to the diagnosis D_1 (**Figure 1**).

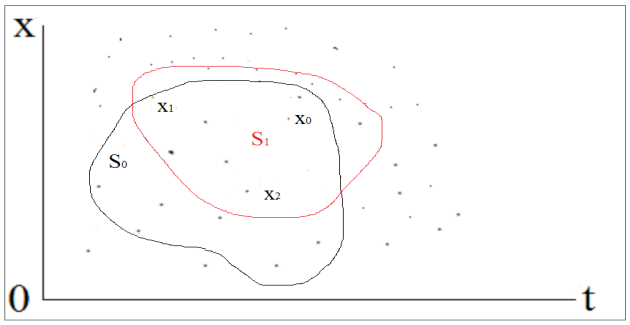

Figure 1. Graphical expression of the possibility of diagnosing the atmospheric boundary layer in unstable or stable states.

Further, we denote by W (xi/Di) = W ((x_1,x_2,… x_n)/Di), (i = 0 or 1) the conditional probability densities of the distribution of the vector of parameters x of the states D_0 and D_1.

Then the probabilities of correct diagnoses when

dividing the space into areas S_0 and S_1 can be calculated using relation (1):

$$\begin{aligned} P_0 &= P(D_0)P(x \in S_0 / D_0) = P(D_0)\int_{S_0} w(x / D_0)dx \\ P_1 &= P(D_1)P(x \in S_1 / D_1) = P(D_1)\int_{S_1} w(x / D_1)dx \end{aligned} \quad (1)$$

The error probability in diagnosing the state of the unstable boundary layer of the atmosphere will be taken as P_F. The probability of an erroneous statement of a stable state of the atmospheric boundary layer will be called P_M. We will consider errors P_F and P_M as errors of the first and second kind, respectively:

$$\begin{aligned} P_F &= P(D_0)P(x \in S_1 / D_0) = P(D_0)\int_{S_1} w(x / D_0)dx \\ P_m &= P(D_1)P(x \in S_0 / D_1) = P(D_1)\int_{S_0} w(x / D_1)dx \end{aligned} \quad (2)$$

Figure 2 shows the probability density distribution of the vector x of the field of diagnostic parameters (x_1, x_2,…x_n) for two possible states of the object under study (unstable and stable). So, the area S_0 at $x < x^o$ corresponds to the diagnosis D_0; S_1 at $x > x^o$ determines the diagnosis D_1; finally, x^o is the value of the vector x of diagnostic parameters separating the areas S_0 and S_1. Segments BC and AB, formed at the intersection of probability density curves for the distribution of the vector of diagnostic parameters, represent the probabilities of errors in diagnosing the state of the atmospheric boundary layer P_F and P_M of the first and second kind, respectively.

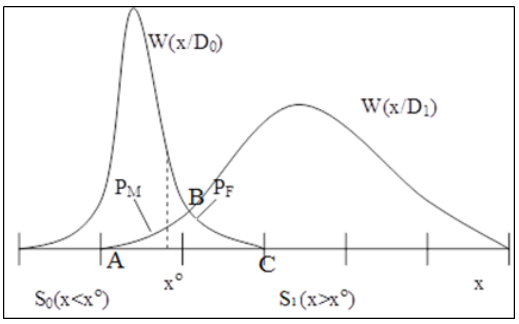

Figure 2. Conditional probability densities of a possible hit of the vector x in the areas S_0 and S_1.

Hence, in order to calculate the required probability of the diagnosed object transition from a stable state to an unstable state, it is necessary to investigate the area of the geometric figure ABC, divided by the perpendicular x^o. To obtain reliable results for calculating the area of a figure, we use the method of dividing the figure into unit segments with their subsequent summation. Taking into account, at the same time, that the number of segments is limited, it is selected empirically and depends on the set of diagnosed parameters x_1, x_2,…x_n.

Since errors in diagnosing an unstable state of the atmospheric boundary layer can lead to omissions in identifying possible hazardous weather phenomena that develop into the lower layer of the atmosphere and pose a real threat to society, economic facilities, etc., which, in connection with the above, cannot be acceptable to society. For this reason, within the framework of this study, the diagnostics of the object under study—the atmospheric boundary layer and its states—will be carried out on the basis of a consequence of the minimum risk method—*the method of the minimum number of erroneous decisions (the minimax method)*.

As is known to us all, this method is used if the costs of losses and gains in the diagnosis are unknown. In our case, the magnitude of damage from possible hazardous weather phenomena is also very close, and their exact size can only be estimated after the elimination of the consequences. The rule for making a diagnosis is found from the minimum proportion of erroneous decisions. The probability of such solutions can be determined by relation (3):

$$P_{ош} = P(D_0)\int_{S_1} w(x / D_0)dx + P(D_1)\int_{S_0} w(x / D_1)dx \quad (3)$$

It can be shown that the above probability is minimal if the region S_0 of the diagnosis D_0 contains x values for which:

$$\lambda(x) > \frac{P(D1)}{P(D0)} = \lambda 0 \quad (4)$$

The equation $\lambda(x) = \lambda_0$ defines the boundary surface between the regions S_0 and S_1 of the diagnostic space. Then the rule for making a diagnosis can be written as inequalities (5):

$$\begin{aligned} &\lambda(x) > \lambda_0, \text{ therefore, the object is in state } D_0 \\ &\lambda(x) < \lambda_0, \text{ therefore, the object is in state } D_1 \end{aligned} \quad (5)$$

Errors of the first P_F and second P_M kind when us-

ing this rule (5) are calculated by formula (2) taking into account the division of the diagnostic space into areas S_0 and S_1.

At present, the minimax method discussed in this study is applied to a surface area with coordinates 60-40° northern latitude and 40-60° eastern longitude. To assess the reliability of the results obtained, individual years from the time interval 1980-2020 were used, within which certain dangerous weather phenomena were recorded within the above geographical coordinates.

The actual result of the study is the established combination of diagnostic parameters, in which the probability of an error of the first kind, P_F, is minimal, which confirms the correctness of the diagnosis and the identified instability of the atmospheric boundary layer. A correct statement of atmospheric instability makes it possible to make an adequate forecast of hazardous phenomena developing in its lower layer, which generally reduces the magnitude of socio-economic losses or damages.

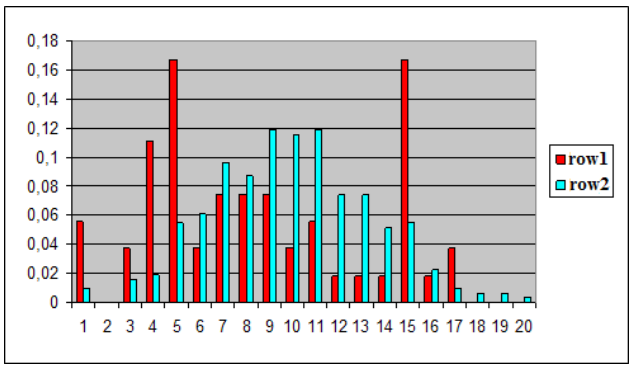

Figure 3. Conditional probabilities of diagnosing atmospheric instability (row 1) and boundary layer stability (row 2) for individual years of the period 1980-2020.

A selection from the array of obtained numerical values of the conditional probabilities of the state of instability of the atmospheric boundary layer is shown in **Figure 3**. So, the y-axis of **Figure 3** shows the numerical values of the vector x, which includes combinations of the diagnosed parameters (x_1, x_2,… x_n): intensity of atmospheric circulation, velocity of geostrophic wind components, activity indices of the Earth's magnetosphere. The abscissa axis shows the numbers of the studied time intervals (dates) when certain dangerous weather phenomena were observed within the studied area of the surface with coordinates 60-40° northern latitude and 40-60° eastern longitude.

4. Discussion

Application of the minimax method for individual years within the time interval 1980-2020 made it possible to identify the most probable diagnostic parameters (x_1, x_2,…x_n) that contributed to the development of the instability of the atmospheric boundary layer. These include the following parameters:

- The intensity of atmospheric circulation is not less than 0.3 hPa/100 km (with the predominant role of its meridional component);
- The speed of the vertical component of the geostrophic wind is not less than –1.7 to –2.1 m/s; horizontal component not less than –0.3 to 0.5 m/s;
- The intensity of the Earth's magnetosphere is not less than 2.3 points.

It is important to note that, in addition to the above values of probable diagnostic parameters and their combinations, as a result of approbation of the minimax method, situations were comprehended when the least probable P_F errors of the first kind were observed in diagnosing an unstable state. So, in particular, the minimum errors P_F in ascertaining the instability of the atmosphere were observed in the following situations, when:

- Circulation intensity had small values;
- The weakly disturbed magnetic field of the Earth was recorded;
- Geostrophic wind velocities differed in average values against the background of negative signs of vectors of their vertical and horizontal components.

It seems that the results obtained can be quite explained by the fact that an increase in the magnetic activity of the Earth's magnetosphere, as well as an increase in the intensity of atmospheric circulation, which contributes to an increase in flow velocities, including the geostrophic wind, in their totality can create so-called noise or interference for the correct making diagnoses of the state of the atmosphere, thereby increasing the likelihood of misdiagnosis.

5. Conclusions

Thus, the mentioned above results of applying the minimum risk or minimax method showed the fundamental usefulness of adapting this method to search for the most probable situational parameters, the combination of which can contribute to the development of atmospheric boundary layer instability in this case. To test this method in the present study, some telluric and cosmic parameters were selected that describe aspects of the physical state of the atmospheric boundary layer and part of the so-called free atmosphere above it vertically. In the future, subsequent selection and expansion of the number of diagnosed parameters are quite possible in order to identify more sensitive elements, the combination of which leads to the development of instability of the atmospheric boundary layer. In this sense, the minimax method, the usefulness of which is shown in this study, can be considered as one of the preparatory steps for the subsequent more detailed method for forecasting individual hazardous weather phenomena.

Author Contributions

The author of this article fully formulated the idea, made calculations, wrote the text, took care of the design of the article.

Conflict of Interest

There is no conflict of interest.

Funding

This research received no external funding

Acknowledgments

In memory of my Teacher and outstanding scientist and oceanologist Professor Karlin L.N.

References

[1] Андреева, Е.С., 2008. Вероятностно-географический метод прогноза сильных ветров для равнин юга России (Russian) [Probabilistic-geographical method of forecasting strong winds for the plains of southern Russia]. Естественные и технические науки. 4(36), 217-220. Available from: https://www.elibrary.ru/item.asp?id=11651224

[2] Andreev, S.S., Popova, E.S., 2012. Global warming and anthropogenic factor. European Journal of Natural History. 4: 27-28. Available from: https://www.elibrary.ru/item.asp?id=20798443

[3] Андреева, Е.С., Андреев, С.С., 2007. География и генезис опасных погодных явлений юга России (Russian) [Geography and genesis of dangerous weather phenomena in the South of Russia]. Издательский дом: Турова Е.А. Ростов-на-Дону. pp. 93. Available from: https://www.elibrary.ru/item.asp?id=19479460

[4] Карлин, Л.Н., Андреева, Е.С., 2003. Принципы управления рисками аномальных погодных явлений (Russian) [Principles of risk management of abnormal weather phenomena] Материалы VIII Всероссийской научно-практической конференции по проблемам защиты населения и территорий от чрезвычайных ситуаций. Центр стратегических исследований гражданской защиты МЧС России. Издательство: ООО “Триада” (Тверь). p. 221-226. Available from: https://www.elibrary.ru/item.asp?id=25079808

[5] Huber, P.J., 1981. Robust statistics. John Wiley & Sons, Inc.: Moscow. pp. 308. DOI: https://doi.org/10.1002/0471725250

[6] Malinetskii, G.G., Faler, D.S., 2014. Bifurcation analysis in a two-mode approximation of the Kuramoto-Tsuzuki system. Mathematical Modeling and Numerical Methods. 3, 111-125.

[7] Вагер, Б.Г., Надеждина, Е.Д., 1975. Структура пограничного слоя атмосферы в условиях горизонтальной неоднородности (Russian) [The structure of the boundary layer of the atmosphere under conditions of horizontal heterogeneity]. Известия Академии наук СССР. Физика атмосферы и океана. 11(6), 565-573.

Available from: https://www.elibrary.ru/item.asp?id=24506080

[8] Вагер, Б.Г., Серков, Н.К., 1996. Конечные цепи Маркова в метеорологии и гидрологии (Russian) [Finite Markov chains in meteorology and hydrology]. Санкт-Петербургский государственный архитектурно-строительный университет (Санкт-Петербург). pp. 111.

[9] Карлин, Л.Н., Ванкевич, Р.Е., Тумановская, С.М., et al., 2008. Гидрометеорологические риски (Russian) [Hydrometeorological risks]. Российский государственный гидрометеорологический университет (Санкт-Петербург). pp. 282. Available from: https://www.elibrary.ru/item.asp?id=19481361

[10] Андонова, А.С., Бабин, А.В., Викулина, М.А., et al., 2013. Влияние изменений климата и опасных природных явлений на природопользование Европейского Севера (Russian) [The impact of climate change and natural hazards on the environmental management of the European North]. РГГМУ. Санкт-Петербург. pp. 124. Available from: https://www.elibrary.ru/item.asp?id=28437325

[11] Карлин, Л.Н., Самусевич, И.Н., 2010. Глобальный климат, история и культура (Russian) [Global climate, history and culture]. Общество. Среда. Развитие. 1, 130-138. Available from: https://www.terrahumana.ru/arhiv/10_01/10_01_25.pdf

[12] Липовицкая, И.Н., 2006. Метод восстановления структуры нижней тропосферы (Russian) [Method of restoring the structure of the lower troposphere]. Научно-технические ведомости Санкт-Петербургского государственного Политехнического университета. 6-1(48), 193-197. Available from: https://www.elibrary.ru/item.asp?id=14777452

[13] Гаврилов, А.С., Петров, Ю.С., 1981. Оценка точности определения турбулентных потоков по стандартным гидрометеорологическим измерениям над морем (Russian) [Estimation of the accuracy of determining turbulent flows by standard hydrometeorological measurements over the sea]. Метеорология и гидрология. 4, 52-59. Available from: https://www.elibrary.ru/item.asp?id=41706784

[14] Василенко, С.В., Гаврилов, А.С., Липовицкая, И.Н., et al., 2006. Метод климатологического анализа вертикальной структуры атмосферного пограничного слоя с использованием численной модели (Russian) [Modeling of the atmospheric boundary layer in relation to the problems of climatology. Interuniversity thematic collection of works]. Ученые записки Российского государственного гидрометеорологического университета. 2, 53-64. Available from: https://www.elibrary.ru/download/elibrary_15614914_54790933.pdf

[15] Гаврилов, А.С., 1973. О строении пограничного слоя атмосферы над поверхностью с произвольными свойствами шероховатости (Russian) [On the structure of the boundary layer of the atmosphere above the surface with arbitrary roughness properties]. Метеорология и гидрология. 12, 35-42. Available from: https://www.elibrary.ru/item.asp?id=41768386

[16] Гаврилов, А.С., Донг, Н.Ф., Хи, Н.Д., 2016. О возможностях использования геострофического соотношения в тропической зоне (Russian) [On the possibility of using the geostrophic ratio in the tropical zone]. Ученые записки Российского государственного гидрометеорологического университета. 42, 104-108. Available from: https://www.elibrary.ru/item.asp?id=25953200

[17] Белушкина, Г.В., Булыгин, Б.И., Деундяк, Д.В., 2010. Расчёт накопления вредных веществ в замкнутом объёме помещения обкатки машин в аварийной ситуации (Russian) [Calculation of the accumulation of harmful substances in a closed volume of a machine running-in room in an emergency situation]. Вестник Донского государственного технического университета. 10(3), 397-401. Available from: https://www.vestnik-donstu.ru/jour/article/view/993/988?locale=en_US

[18] Шамшура, С.А., Богданова, И.В., 2008. Математическая модель резонансного

гасителя (Russian) [Mathematical model of a resonant damper]. Вестник Ростовского государственного университета путей сообщения. 4(32), 15-19. Available from: https://www.elibrary.ru/item.asp?edn=jvylpj

[19] Булыгин, Ю.И., Панченко, О.С., Романов, В.А., et al., 2013. Повышение эффективности обеспыливания воздуха рабочих зон металлообрабатывающих и деревообрабатывающих производств (Russian) [Improving the efficiency of dedusting the air of working areas of metalworking and woodworking industries]. Вестник Донского государственного технического университета. 13(7-8), 49-57. DOI: https://doi.org/10.12737/2020

[20] Дымникова, О.В., Зарипова, Ю.С., Воскобойник, Т.С., 2012. Проблемы обращения с ртутьсодержащими отходами (Russian) [Problems of mercury-containing waste management]. Вестник Донского государственного технического университета. 12(5), 10-18. Available from: https://www.vestnik-donstu.ru/jour/article/view/601?locale=en_US

BILINGUAL PUBLISHING GROUP

Journal of Atmospheric Science Research
https://journals.bilpubgroup.com/index.php/jasr

ARTICLE

Rainfall and Temperature Variations in a Dry Tropical Environment of Nigeria

David O. Edokpa[1*], Precious N. Ede[1], Bridget E. Diagi[2], Susan I. Ajiere[3]

[1] *Department of Geography and Environmental Management, Faculty of Social Sciences, Rivers State University, Port Harcourt, 500262, Nigeria*

[2] *Department of Environmental Management, Federal University of Technology, Owerri, 460114, Nigeria*

[3] *Department of Geography and Environmental Management, University of Port Harcourt, Port Harcourt, 500262, Nigeria*

ABSTRACT

This study examines long-term rainfall and temperature variations over a dry tropical environment in Nigeria. An assessment of the variations of these weather variables showcases the extent of climate change limits and corresponding effects on the biotic environment. Rainfall and temperature data were obtained from Nigerian Meteorological Agency for a period of 31 years (1991-2020) for Kano and Katsina States. Descriptive statistics were used to determine the degree of variability of the weather variables across spatial domains. Results showed that there is a sharp contrast in mean annual rainfall amounts of 1154.1 mm and 569.6 mm for Kano and Katsina located in the dry continental and semi-arid climate zones of Nigeria respectively. It is revealed that the month of August had the highest mean monthly rainfall for both areas i.e. 359 mm and 194 mm with little or no trace during the dry season. The sharp difference in rainfall amount across spatial domains of the near similar climate zones shows that the Inter-tropical Discontinuity (ITD) does not completely overwhelm the northern band of Nigeria in August. The least variable monthly rainfall was in August and July with coefficient variations (CV) of 40% and 47% for Kano and Katsina. The months of February and March had the highest CV of 557% and 273% for the respective areas. In the examined areas the wet and dry seasons are from June-September and October-May respectively. The index of rainfall variability and drought intensity for the areas ranged from 0.85-0.95 and 45% indicating moderate variability and drought respectively. Mean annual temperature values are 33.4 °C and 33.8 °C for Kano and Katsina. The study recommends a proper climate observing scheme, most especially for agrarian practices so as to ensure profitable outputs for human sustainability.

Keywords: Rainfall; Air temperature; Climate change; Kano State; Katsina State

*CORRESPONDING AUTHOR:
David O. Edokpa, Department of Geography and Environmental Management, Faculty of Social Sciences, Rivers State University, Port Harcourt, 500262, Nigeria; Email: david.edokpa@ust.edu.ng

ARTICLE INFO
Received: 10 March 2023 | Revised: 05 April 2023 | Accepted: 10 April 2023 | Published Online: 14 April 2023
DOI: https://doi.org/10.30564/jasr.v6i2.5527

CITATION
Edokpa, D.O., Ede, P.N., Diagi, B.E., et al., 2023. Rainfall and Temperature Variations in a Dry Tropical Environment of Nigeria. Journal of Atmospheric Science Research. 6(2): 50-57. DOI: https://doi.org/10.30564/jasr.v6i2.5527

COPYRIGHT
Copyright © 2023 by the author(s). Published by Bilingual Publishing Group. This is an open access article under the Creative Commons Attribution-NonCommercial 4.0 International (CC BY-NC 4.0) License. (https://creativecommons.org/licenses/by-nc/4.0/).

1. Introduction

Rainfall and temperature are major climatic factors that impact the semi-arid zone of tropical West Africa. A distinct wet season exists from June to September when there is a southward retreat of the bands of low pressure known as the Inter-tropical Discontinuity (ITD). Variations in rainfall and air temperature for any region arise from the energy interactions between the surface layer and the lower atmosphere including the dominant air mass that characterizes the region [1]. The variation of rainfall pattern is vital as it determines the onset, cessation and extent of seasons as well as an important component of climate and hydrological systems [2-4]. Rainfall changeability is slight in humid regions of the wet tropics and most variable in dry and sub-humid areas. The sub-humid areas are the most vulnerable since small negative deviations from the mean rainfall may cause widespread crop failure and famine as frequently happens in the area. Minimal rainfall deviations indicate that the average amount for any specified catchment is steady while large deviations denote extensive variations in the average rainfall amount. A given amount of rainfall may be termed consistent if it can be expected to be corresponded to or surpassed some chosen probability level.

Nigeria characterised by a low-lying is principally placed within the warm and humid tropics close to the equator which induces a high ambient temperature pattern [5] and this near equatorial position boosts the high-temperature condition observed over the area all through the year. As noted by Ayoade [2], Nigeria's latitudinal position as well as solar elevation which is large at low latitudes contributes to the high-temperature range. Temperatures over the dry tropical zone of Nigeria have increased over the last decades, in line with an increase in global temperatures [6,7]. The impact of global warming on rainfall in the zone remains challenging to assess in a climate that is vulnerable to vital variation at spatial-temporal scales. Future soil suitability for major crops is expected to be affected by climate change; in particular beans, maize and millet production might face declines and require cropping system transformations. This study evaluated the rainfall and temperature deviations between two close areas (Kano and Katsina) both at the northern tip of Nigeria, however, under the influence of different climate zones.

2. Materials and methods

2.1 Study area

The climate of the study domains are classified by Koppen's climate pattern as *Aw* (wet and dry tropical continental with a mono-modal rainfall pattern) and *BSh* (a climate domain that has the characteristics of both the Sahara Desert and tropical wet and dry climate i.e. semi-arid zone, with more of a dry condition). **Figure 1** shows the map of both Kano and Katsina with part of Katsina bordering the Niger Republic. Subsidence prevails almost all year round with respect to the high-pressure area being influenced by the Saharan Desert bearing dry tropical continental air mass. The mean ambient temperature for both diurnal and annual ranges is large from 20 °C to 25 °C [2]. Lower and higher temperatures are recorded during December—January and March—April with 12 °C and 40 °C being the extreme low and high respectively. Ayoade [2] noted that August is recorded as a peak rainfall period with a mean range of 215-250 mm and intermittent or irregular nature of rainfall that spans between May-September exists in the area [8,9]. According to Mamman et al. [10], the mean annual minimum and maximum range for 262-956 mm. Rainfall amount for Kano and Katsina are 416-1872 mm and due to the domains' distance and position from the influence of rain-bearing air mass from the Atlantic Ocean, longer dryer spells persist from October to May when there is a retreat of the ITD towards the coast in September. The extensive dyer days sustained by a mean sunshine diurnal range of 8-11 hours increases the evapotranspiration rate thereby enhancing drought and desertification of the area [11]. The cloudiness index for the area is less than 0.45 while the mean surface solar radiation across seasons is greater than 280 W/m^2 [12]. The dryer atmosphere retains less amount of water vapour

to a percentage range of 18%-63%. The study area exhibits a typical feature of the Sahel Savannah environment where there is less vegetation with a vast landmass that increases surface wind speed with a mean range of 1.5-12 m/s.

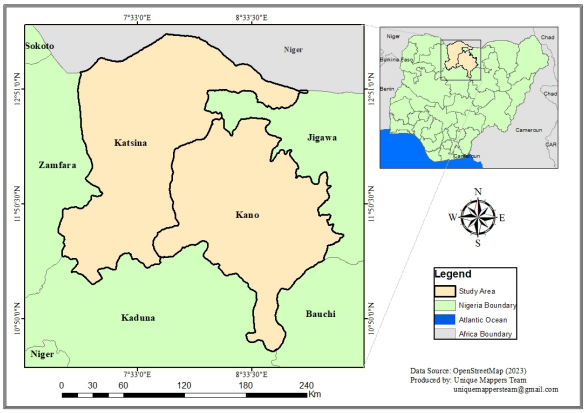

Figure 1. Map of study areas.

2.2 Rainfall and temperature data

A 31-year mean monthly rainfall and temperature data for Kano and Katsina from 1990-2020 were acquired from the Nigerian Meteorological Agency and analysis was done using Microsoft Excel Spreadsheet 2016. Statistical tools were engaged to determine the seasonal spatial variations of the retrieved climate data. Oyegoke et al. [13] indicated that statistical techniques of analysis are essential normally to precisely evaluate rainfall data for effective planning and for future forecasts regarding proficient and operative water resources management. The coefficient of variation (CV) was used to examine the extent of rainfall variation. The method is given as:

$$CV = \sigma/\bar{x} \quad (1)$$

where: σ is the rainfall standard deviation and $\bar{x}$ is the mean rainfall and CV is the coefficient of variation. The 10, 50 and 90 percentiles are the index of rainfall changeability used in climatological studies and according to Ayoade [14] it is as follows:

$$(90\% - 10\%)/50\% \quad (2)$$

where greater than 1.75 is extreme variability; 1.50-1.75 is very high variability; 1.25-1.50 is high variability, 1.00-1.25 is moderately high variability; between 0.75-1.00 is moderate variability; 0.50-0.75 is moderately low variability; < 0.05 is low variability. The measure of drought intensity was analysed using the percentage derivation below the mean, with the following categories: 11-25 (slight drought), 26-45 (moderate drought), 46-60 (severe drought) and more than 60 (disastrous drought).

3. Results and discussion

Results as shown in **Figure 2** indicate the average monthly values of rainfall in Kano and Katsina in the dry continental (Koppen's *Aw*) and semi-arid (Koppen's *BSh*) climate zones of Nigeria respectively. The study areas recorded rainfall values of less than 50 mm from October to April. This shows the extent of the dry season for the areas with 0 mm rainfall from November to March. The rainiest month for the areas was in August with peak values of 194 mm and 359 mm for Katsina and Kano. The percentage contributions of the peak rainy month for the areas to the overall amount were 34% and 30% for Katsina and Kano respectively (**Figure 3**). The highest difference for the climate indicator pattern was during the dry season for the months of February and March where the CVs were 557% and 273% for Kano and Katsina respectively. The lowest spatial variability was experienced in July and August i.e. (CVs of 40 and 47 %) for the respective areas (**Figure 4**). The high coefficient of variations for the dry season showed the complete dominance of the dry continental air mass in Kano for the month of February (with rainfall amount of 0.3 mm) and in Katsina for the month of March (with a rainfall amount of 1.5 mm). It showed that, there was little encroachment of the rain-bearing moist maritime air mass for the areas. The complete dominance of moist maritime air mass during the rainy season indicates the lowest spatial variability for the climate indicator.

Also, as shown in **Figure 5**, there is a distinct spatial difference in the average annual rainfall spread in Kano and Katsina from 1990 to 2011. Kano experienced a dominant rainfall domain for the specified years and Katsina experienced the only dominance for the zone in 2015. The year 2020 shows a similar

trend for both areas, however, indicating a back shift for the Kano rainfall pattern when compared to that for Katsina. This shows that the study areas in the same climate zone varied in spatial rainfall values, however both areas have no strong relationship with the El Nino Southern-Oscillatiom (ENSO) associated with convective rainfall across the equatorial Pacific Ocean as investigated by Hashidu and Badaru [15]. Mohammed et al.; Abaje et al. [16,17] highlighted in studies of rainfall patterns in Kano (1914-2013) and (1911-2010) respectively that there was an improvement in the moisture condition for the area during the last two decades when compared to the past. As shown in **Figure 5**, there was a lower rainfall amount in Katsina from 1990-2003 when compared to 2004-2011. A study conducted by Suleiman et al. [18], showed that the above mean rainfall amount was observed from the year 2000 upward. Also, Yamusa and Abdulkadir [19] disclosed that while mean yearly rainfall, onset dates of the wet season as well as yearly minimum and maximum temperature were increasing; the cessation dates and length of the wet season were decreasing. As noted by Adeleke and Orebayo [20], if there is an increase in maximum and mean temperature as well as the onset of rains, then rainfall amount will increase and vice-versa. The index of rainfall variability for the areas ranged from 0.85-0.95 and this shows moderate rainfall variability for the areas.

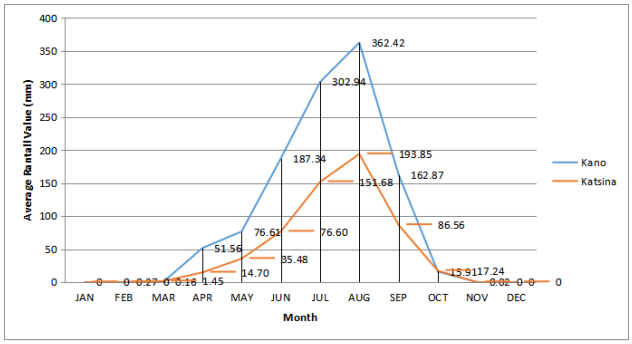

Figure 2. Average rainfall values for the study areas.

The moderate rainfall variability indicates the study domain's location far inland which impedes its constant impact on the Ocean's maritime air. Fabeku and Okogbue [8] and Ogungbenro and Morakinyo [21] highlighted that the mean yearly rainfall amount for the Sahel zone where the study area belongs is from 150 mm to about 1000 mm for the zone. This variability makes the climatic region to be susceptible to heightened actual evapotranspiration which enhances drought especially for Katsina. It has been emphasized that the early cessation of rainfall trend in Katsina is due to the early retreat of the ITD from the area. As disclosed by Yaya et al. [22], the moderate drought condition that exists within the study environment is associated with the late start of the wet season and its early termination. This early cessation as noted by Atedhor [23] impacts soil moisture deficiency that induces forced harvest of crops from the study area most especially rice yield [24]. Peter et al. [25] highlighted that the major crop cultivated in the study environment includes: cowpea, soya beans, cotton, sorghum, millet, etc. The drought index for the areas which was analysed from the percentage rainfall derivation below the mean indicated about 45% for the areas. This shows that there is a moderate drought index experienced in the zone. Ati et al. [26] examined meteorological drought and temperature in the Sudano-Sahelian zone of Nigeria from 60-year and 40-year rainfall and temperature data respectively. It was revealed using the Bhalme and Mooley Drought Index (BMDI) that mild to moderate drought exists in the zone. Cases of droughts according to Dada [27] can be attributed to shifting weather forms exhibited through the consistent accumulation of surface layer heat fluxes, atmospheric fluctuations resulting in reduced rainfall and low rain cloud resulting in greater evaporation rates. It was also emphasised that the ensuing impacts of drought are intensified by anthropogenic happenings. These happenings include grassland clearing and burning, overgrazing and disadvantaged cropping systems, which decrease water holding of the soil, and inappropriate conservation methods leading to soil deficiency. Furthermore, it was specified that numerous flora and fauna kinds are vanishing in the drought-inclined area of Kano and Maiduguri. Activities such as land degradation, bush burning and desertification had impacted the productivity and diversity of flora and fauna in the areas [27,28].

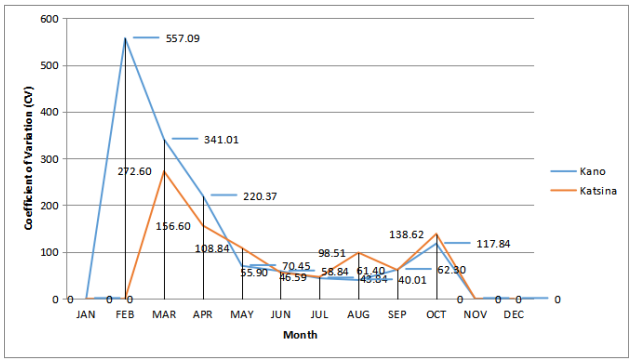

Figure 3. Average percentage contribution of monthly rainfall to annual total value.

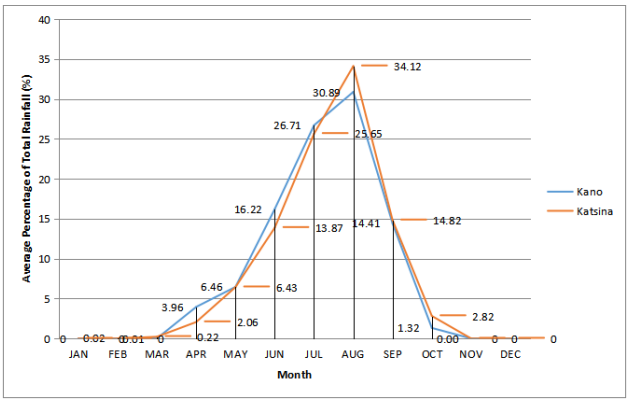

Figure 4. Rainfall coefficient of variation (CV) for study areas.

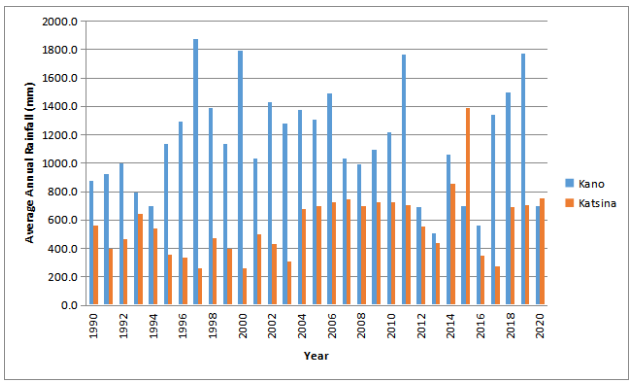

Figure 5. Average annual rainfall values for study areas.

Results as shown in **Figures 6 and 7** indicate the pattern of air temperatures for the study areas. It is shown that annual air temperatures are high for the period considered with ranges from 31-34 °C and 32-35 °C for Kano and Katsina respectively. On average, higher temperatures of range 36-38 °C are recorded from March to May for the areas with April being the hottest month and December being the coolest month. The high-temperature pattern which cuts through both the end of dry and the beginning of wet seasons shows that the zone is found in the high-pressure zone where air subsidence dominates. Akinsanola and Ogunjobi [29] observed that the air temperature is typically high and low during the wet and dry seasons respectively and this makes temperature deviation lower at the coast than in the northern domain of Nigeria. The study domain is majorly influenced by the dry and stable continental air from across the Saharan desert. This trend makes the zone fall under the Sudan-Sahel climate region of Nigeria with a latitude from 11° to 13° [30]. On the monthly average, the difference between the maximum highest temperatures and lower temperatures is 10 °C for the study areas. This high-temperature peak range shows the effect of climate change anomaly arising from excessive heating of the earth's surface where more heat is experienced and less rainfall is observed. This implied that the high variability of average monthly temperatures can affect plant growth and development. It can also affect the comfort index of human endeavors across the areas [31]. An assessment of the aridity index of Katsina has shown that its northern axis is within the arid zone while the southern axis falls in the semi-arid zone with an index of 0.26 and 0.49 respectively with an overall aridity increase from years 2000 to 2016 [32]. The study further highlighted a significant increase in actual evapotranspiration in Katsina. Ibrahim et al. [33] observed in a study conducted that extremely high and low ambient temperature has been noted to support the survival of mosquitoes in Katsina. It was highlighted that sharp deviations of temperature changes enhanced 77% of severe malaria cases for an infant with occurrence between the months of May-September. It was recommended that adequate medical care be offered to children less than 5 years old.

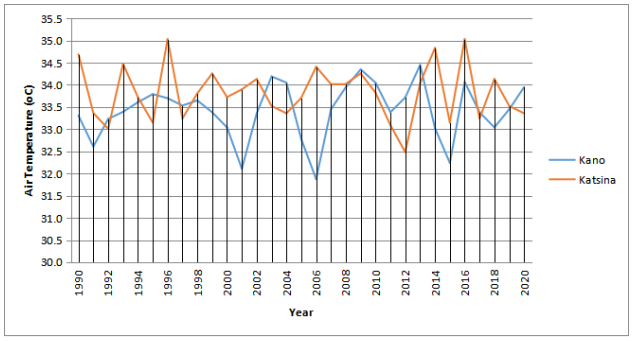

Figure 6. Average annual air temperature values for study areas.

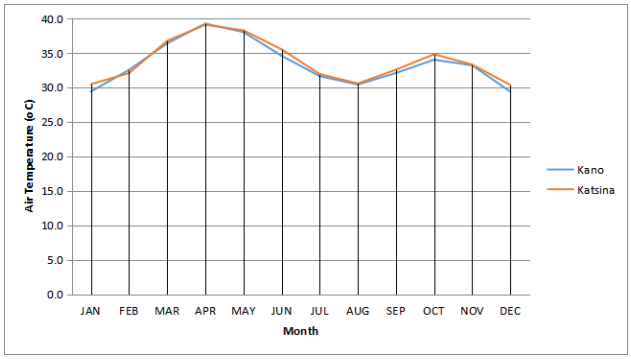

Figure 7. Average monthly air temperature values for study areas.

4. Conclusions

This study surveyed the rainfall and temperature variations for Kano and Katsina areas domiciled in the Sudan zone of Nigeria. An assessment of the variability of the weather variables considered shows that climate change limits and impacts the liveable environment. Study findings show that there is moderate rainfall variation with a low rainfall pattern especially for Katsina as compared to Kano and also a moderate drought pattern for the areas. The evaluated drought pattern may degenerate to a severe category if conservation practices are not put in place. Average monthly maximum temperatures for the areas ranged from 29-39 °C. This high-temperature peak shows the effect of climate change arising from excessive heating of the earth's surface where more heat is experienced and less rainfall observed. This climate pattern will definitely impact the dominant agricultural practices that prevail in the study areas with subsequent effects on the economic development of the region. The study recommends a proper climate observing scheme, most especially for agrarian practices so as to ensure profitable outputs for human sustainability.

Conflict of Interest

There is no conflict of interest.

References

[1] Adejuwon, J.O., 2018. Effects of seasonal on spatial variability of rainfall in the Niger Delta, Nigeria. Journal of Applied Sciences and Environmental Management. 22(10), 1701-1706.

[2] Ayoade, J.O., 2004. Introduction to climatology for the tropics (2nd edition). Spectrum Books: Ibadan.

[3] Shiru, M.S., Park, I., 2020. Comparison of ensembles projections of rainfall from four bias correction methods over Nigeria. Water. 12(11), 2-16.

[4] Okorie, F.C., 2021. North Atlantic oscillation and rainfall variability in south-eastern Nigeria: A statistical analysis of 30 year period. Journal of Atmospheric Science Research. 4(4), 42-49.

[5] Edokpa, O.D., 2018. Atmospheric stability conditions of the lower atmosphere in selected cities in Nigeria [Unpublished PhD thesis]. Port Harcourt: University of Port Harcourt.

[6] Niang, I.O., Abdrabo, M.A., Esssel, A., et al., 2014. Africa, Climate change 2014: Impacts, adaptation, and vulnerability. Part B: Regional aspects. Contribution of Working Group II to the Fifth Assessment Report of the Intergovernmental Panel on Climate Change. Cambridge University Press: Cambridge. pp. 1199-1266.

[7] Abaje, I.B., Oladipo, E.O., 2019. Recent changes in the temperature and rainfall conditions over Kaduna State, Nigeria. Ghana Journal of Geography. 11(2), 127-157.

[8] Fabeku, B.B., Okogbue, E.C., 2014. Trends in vegetation response to drought in Sudano-Sahelian part of Northern Nigeria. Atmospheric and Climate Sciences. 4, 569-588.

[9] Agunbiade, O., Adelekan, I., 2017. Monitoring

drought occurences over the Sahel and Sudan Savannah of Nigeria using NDVI. International Journal for Research in Applied Sciences & Engineering Technology. 5, 2178-2188.

[10] Mamman, M.B., Bello, A.A., Usman, A.A., 2018. Analysis of rainfall variation over northern parts of Nigeria. Environmental and Earth Sciences Research Journal. 5(3), 74-78.

[11] Odjugo, P., Ikhuoria, A., 2003. The impact of climate change and anthropogenic factors in desertification in the semi-arid region of Nigeria. Global Journal of Environmental Science. 2(2), 118-126.

[12] Julius, K.A., Balogun, R.A., 2022. Characteristics and distribution of some radiation parameters over Nigeria. European Journal of Environment and Earth Sciences. 3(4), 32-40.

[13] Oyegoke, S.O., Adebanjo, A.S., Ododo, H.J., 2020. Rainfall intensity analysis for synoptic stations in northern Nigeria. Nigerian Journal of Technological Development. 17(3), 223-228.

[14] Ayoade, J.O., 2008. Techniques in climatology. Stirling-Horden Publishers: Ibadan.

[15] Hashidu, U.S., Badaru, S.I., 2021. Relationship between El-Nino southern-oscillation and rainfall in Susano-Sahelian region of Northern Nigeria. Journal of Agricultural Economics, Environment and Social Sciences. 7(2), 211-216.

[16] Mohammed, M.U., Abdulhamid, A., Badamasi, M.M., et al., 2015. Rainfall dynamics and climate change in Kano, Nigeria. Journal of Scientific Research & Reports. 7(5), 386-395.

[17] Abaje, I.B., Ndabula, C., Garba, A.H., 2014. Is the changing rainfall patterns of Kano State and its adverse impacts an indication of climate change? European Scientific Journal. 10(2), 192-206.

[18] Suleiman, U.B., Abdulhamid, A.I., Salisu, K., 2020. Trend analysis of monthly and annual rainfall profile in Katsina and its environs. FUDMA Journal of Sciences. 4(1), 519-527.

[19] Yamusa, A.M., Abdulkadir, A., 2020. Rainfall and temperature trends in Samaru and Minjibir, Northern Guinea and Sudan Savannas of Nigeria. Journal of Sustainable Agriculture and the Environment. 18(2), 255-265.

[20] Adeleke, E.A., Orebayo, E.A., 2020. Spatio-statistical analysis of rainfall and temperature distribution, anomaly and trend in Nigeria. Geosfera Indonesia. 5(2), 226-249.

[21] Ogungbenro, S.B., Morakinyo, T.E., 2014. Rainfall distribution and change detection across climatic zones in Nigeria. Weather and Climate Extremes. 5-6, 1-6.

[22] Yaya, O.S., Gil-Alana, L.A., Akomolafe, A.A., 2015. Long memory, seasonality and time trends in the average rainfall in major cities of Nigeria. CBN Journal of Applied Statistics. 6(2), 39-58.

[23] Atedhor, G.O., 2020. Rainfall variability during onset and cessation of the growing season in the Sudano-Sahelian region of Nigeria. Journal of Geography Meteorology and Environment. 3(1), 1-14.

[24] Akinbile, C.O., Ogunmola, O.O., Abolude, A.T., et al., 2019. Trends and spatial analysis of temperature and rainfallpatterns on rice yields in Nigeria. Atmospheric Science Letters. 21, 1-13.

[25] Peter, I.E., Henry, V.N., Chinasa, E.C., 2018. Assessment of the effect of temperature and rainfall in agriculture in Nigeria. SSRG International Journal of Agriculture & Environmental Science. 5(3), 21-25.

[26] Ati, O.F., Aremu, K., Olatunde, A.F., et al., 2022. Meteorological drought and temperature in Sudano-Sahelian region of Nigeria under increasing global warming. The nature, causes, effects and mitigation of climate change on environment. IntechOpen Limited: London. DOI: https://doi.org/10.5772/intechopen.100108

[27] Dada, B.M., 2022. Drought and its intricating impacts on some areas in northern Nigeria. International Research Journal of Innovations in Engineering Technology. 6(3), 75-87.

[28] Olagunju, T.E., Adewoye, S.O., Adewoye, A.O., et al., 2021. Climate change impacts on environment: Human displacement and social conflicts

in Nigeria. Earth and Environmental Sciences. 655, 1-10.

[29] Akinsanola, A.A., Ogunjobi, K.O., 2014. Analysis of rainfall and temperature variability over Nigeria. Global Journal of Human-Social Science: (B). 14(3), 1-17.

[30] Kurowska, E.E., Czerniak, A., Garba, M.L., 2022. Afforestation of transformed savanna and resulting land cover change: A case study of Zaria (Nigeria). Sustainability. 14, 1-22.

[31] Ukhurebor, K.E., Siloko, I.U., 2020. Temperature and rainfall variability studies within south-south region of Nigeria. Assumption University-eJournal of Interdisciplinary Research. 2, 1-19.

[32] James, G.K., Jega, I.M., Olojo, O.O., et al., 2018. Geospatial assessment of climatic variability and aridity in Katsina State, Nigeria. International Journal of Innovative Science and Research Technology. 3(12), 615-625.

[33] Ibrahim, O.R., Lugga, A.S., Ibrahim, N., et al., 2021. Impact of climatic variables on childhood severe malaria in a tertiary health facility in northern Nigeria. Sudanese Journal of Paediatrics. 21(2), 173-181.

BILINGUAL PUBLISHING GROUP

Journal of Atmospheric Science Research
https://journals.bilpubgroup.com/index.php/jasr

ARTICLE

Formation and Transport of a Saharan Dust Plume in Early Summer

Habib Senghor[1*], Abdou L. Dieng[2], Moussa Gueye[3], Cheikh A. Diop[1], Mariane D. Kane[1], Amadou T. Gaye[2]

[1] *Agence Nationale de l'Aviation Civile et de la Météorologie, Dakar, 8184, Sénégal*
[2] *Laboratoire de Physique de l'Atmosphère et de l'Océan Siméon-Fongang (LPAO-SF), Université Cheikh Anta Diop, Dakar, 10700, Sénégal*
[3] *Département de Mathématiques et Informatiques, Université du Sine Saloum Elhadj Ibrahima Niass, Kaolack BP 55, Sénégal*

ABSTRACT

This research studies the capability of the Weather Research and Forecasting model coupled with the Chemistry/Aerosol module (WRF-Chem) with and without parametrization to reproduce a dust storm, which was held on 27th June 2018 over Sahara region. The authors use satellite observations and ground-based measurements to evaluate the WRF-Chem simulations. The sensitivities of WRF-Chem Model are tested on the replication of haboob features with a tuned GOCART aerosol module. Comparisons of simulations with satellite and ground-based observations show that WRF-Chem is able to reproduce the Aerosol Optical Depth (AOD) distribution and associated changes of haboob in the meteorological fields with temperature drops of about 9 °C and wind gust 20 $m \cdot s^{-1}$. The WRF-Chem Convection-permitting model (CPM) shows strong 10-meter winds induced a large dust emission along the leading edge of a convective cold pool (LECCP). The CPM indicates heavy dust transported over the West African coast (16°W-10°W; 6°N-21°N) which has a potential for long-distance travel on 27th June between 1100 UTC and 1500 UTC. The daily precipitation is improved in the CPM with a spatial distribution similar to the GPM-IMERG precipitation and maximum rainfall located at the right place. As well as raising a large amount of dust, the haboob caused considerable damage along its route.

Keywords: Dust storm; WRF-Chem; Convection-permitting; Parameterization; MCS

*CORRESPONDING AUTHOR:
Habib Senghor, Agence Nationale de l'Aviation Civile et de la Météorologie, Dakar, 8184, Sénégal; Email: habib.senghor@anacim.sn

ARTICLE INFO
Received: 12 January 2023 | Revised: 06 April 2023 | Accepted: 10 April 2023 | Published Online: 14 April 2023
DOI: https://doi.org/10.30564/jasr.v6i2.5407

CITATION
Senghor, H., Dieng, A.L., Gueye, M., et al., 2023. Formation and Transport of a Saharan Dust Plume in Early Summer. Journal of Atmospheric Science Research. 6(2): 58-74. DOI: https://doi.org/10.30564/jasr.v6i2.5407

COPYRIGHT
Copyright © 2023 by the author(s). Published by Bilingual Publishing Group. This is an open access article under the Creative Commons Attribution-NonCommercial 4.0 International (CC BY-NC 4.0) License. (https://creativecommons.org/licenses/by-nc/4.0/).

1. Introduction

As a major contributor to global dust emissions, the North African region plays an important role in the Earth's climate by scattering and absorbing incoming solar radiation and changing the physical properties of clouds [1]. Dust particles can be used in cloud formation as giant cloud condensation nuclei which can affect the microphysics development of clouds [2]. The effect of mineral dust on the cloud properties is to inhibit precipitation [3]. However, the role of Saharan dust on rainfall remains poorly understood [4] since research works showed, on contrary, that dust could enhance the precipitation in numerical weather prediction (NWP) models [5]. Kocha et al. [6] highlighted the necessity to couple the NWP forecasting models with an aerosol module [6]. The utilization of a dust scheme in NWM could contribute to improving the cloud cover in West Africa [7]. In this region, the mesoscale convective systems contribute the most to the precipitation during the monsoon season [8]. The total precipitation is generated particularly up to 90% by the convective storms in West Africa [9]. The convective storms generate downdrafts and cold pools over dry dusty surfaces producing large dust storms [10]. The haboobs are dust storms produced by the spreading of evaporatively cooled air from thunderstorms over the dusty area [10]. Several thunderstorms produce mesoscale convective systems when they merge to create a continuous area of convective instability that persists at least for several hours and produces a continuous precipitation area [11].

Finney et al. [12] have highlighted the limitation of the Parameterized models (PM) due to their approximations in the representation of the convection. Using two simulations with 12 km horizontal grid spacing, one running with Parameterized and the other with explicit convection, Birch et al. [13] showed a significant bias of the diurnal water cycle. The uncertainties of the diurnal water cycle have induced an increase in the northward advection of the moisture into Sahel [13]. Marsham et al. [14] showed that simulations of the West African monsoon explicitly resolve moist convection with simulations which parameterize convection with the UK Met Office Unified Model with 12 km grid spacing. By using the dust uplift potential (DUP), which represents the dependency of dust uplift on wind speed for an idealized land surface, Marsham et al. [15] showed that haboobs are absent in models with parametrized convection. These failures have been linked to systematic errors [16]. On the other hand, several studies showed that CPM can be helpful for improving rainfall [13,17,18] by reducing the biases of the diurnal cycle of simulated precipitation, extreme precipitation, cloud cover, and radiation [18]. The explicit convection improves the intensity of storms and the West Africa monsoon [19,20]. Nevertheless, the meteorological features are not improved in whole aspects of the CPM model [18,21].

This study aims to examine the ability of WRF-chem to reproduce a dust storm and the mesoscale characteristics associated with the event, from 26 to 27 June 2018 over Western Africa, by using parametrized and explicit convection. The impact of dust on solar radiation, 2-meter temperatures and changes including precipitation is also studied using an additional simulation with no dust activation (NODUST).

The paper is organized as follows. Datasets, model experiments and methodology are described in Section 2. The satellite observations and ground measurements are used to describe the synoptic state of the event in Section 3.1. The evaluation of simulated dust AOD is presented in Section 3.2. The properties of the storm in the model simulations are analyzed in Sections 3.3 and 3.4. The impact of the dust on the radiative budget is investigated in Section 3.5. Finally, the conclusion is given in Section 4.

2. Data and method

2.1 Observations

The moderate resolution imaging spectroradiometer (MODIS) is a passive imaging radiometer that measures reflected radiation and emitted thermal

radiation in 36 bands. The dataset is provided with 10 km as a horizontal resolution for a better comparison with simulated AOD [22]. Cold pools can be discriminated in the dust channels with dark color and mineral dust with pink color [23]. The identification of dust depends strongly on the column water vapor, the lower tropospheric lapse rate, and dust altitude. Dust is particularly masked when the water vapor exceeds 25 mm [23].

The moderate resolution imaging spectroradiometer (MODIS) is a passive imaging radiometer and measures reflected radiation and emitted thermal radiation in 36 bands. Dataset are provided with 10 km as horizontal resolution for a better comparison with simulated AOD [24]. We use MODIS/Aqua level-3 atmosphere daily global product which overpass above Western Africa in the afternoon.

The Infrared Atmospheric Sounding Interferometer (IASI) algorithm, which enables to retrieval of optical and microphysical properties of aerosol types [25], is used to retrieve dust AOD during the event.

The Visible Infrared Imaging Radiometer Suite (VIIRS) deep blue Aerosol Optical Thickness (AOT) layer is taken from the National Aeronautics and Space Administration (NASA)/National Oceanic and Atmospheric Administration (NOAA) Suomi National Polar-Orbiting Partnership (Suomi NPP) satellite for the daytime overpass. The imagery resolution is 2 km at nadir, and the temporal resolution is daily [26,27].

The Global Precipitation Measurement (GPM) was launched on 27 February 2014 by NASA in association with the Japan Aerospace Exploration Agency (JAXA) to provide a higher spatiotemporal resolution product for global precipitation between 60°S and 60°N [28]. We use 24 h accumulated rainfall from Integrated Multi-satellite Retrievals for Global Precipitation Measurement (IMERG) version V06 with a 0.1° × 0.1° spatial grid.

The fifth generation of reanalysis from the European Center for Medium-Range Weather Forecasts (ECMWF) ERA5 is used to investigate the synoptic situation preceding the initiation of the MCS. The ERA5 dataset is provided at a 1-hourly time step and is gridded to a regular latitude-longitude of 31 km horizontal resolution and 139 pressure levels [29].

2.2 Model description and experimental setup

We use the WRF model version 3.7.1 coupled with chemistry which enables the simulation of aerosols and trace gases with meteorological fields [30]. Both models are run from 15 to 29 June with one-day spin-up. Daily mean AOD from 16 at 00:00 and 29 June at 23:00 in 2018 are computed boundary conditions provided by NOAA/National Centers for Environmental Prediction Final Analysis (NCEP-FNL) with a horizontal grid spacing of 0.5° × 0.5° and interpolated by WRF preprocessing system and update every 6 hours. The simulation domain is centered in North Mali (1°W, 19°N) and contains 390 × 250 horizontal grid points with 9 km resolution and 51 vertical levels extending up to 50 hPa. The configuration of the model uses the Goddard Global Ozone Chemistry Aerosol Radiation and Transport (GOCART) module [31] to simulate mineral dust concentration PM10 and AOD. The Yonsei University (YSU) planetary boundary layer scheme [32], the Noah land-surface model [33], the revised Mesoscale Model (MM5) scheme [34], the Rapid Radiative Transfer Model for Global models (RRTMG) for shortwave [35] and RRTM for longwave radiation [36], the Grell cumulus parametrization [37] and WRF Single-Moment 5-class (WSM5) microphysics schemes [38] are used by the configuration (**Table 1**). The aerosol feedback which provides a reduction in downward solar radiation from aerosol scattering is taken into account [39]. The Parameterized (PM) and the CPM models used the same configuration except that cumulus (CU) parametrization is not activated in the CPM model. A control simulation is also run to evaluate the impact of dust in the 2 m temperature.

2.3 Model tuning

The sensitivity tests which consist to adjust the coefficient of dust emission flux are performed with

the GOCART aerosol module in both PM and CPM models. In this study, the GOCART dust scheme parametrization is tuned by calibrating dust emission to match observed AOD from AERONET (not shown) and satellites retrieved AOD averaged in the entire domain (**Figure 1**). For this purpose, the coefficient C in Equation (1), which was originally estimated to be 0.8 $mg \cdot s^2 \cdot m^{-5}$ [31] in version 3.7.1, is adjusted to achieve the most agreement with observed AOD [40,41]. The dust emission mass flux, *Fp* ($\mu g \cdot m^{-2} \cdot s^{-1}$), for a specific aerosol size group *p* is defined as followed:

$$F_p = \begin{cases} CSS_p\,(U^2_{10m} - U_t) & \text{if } U_{10m} > Ut, \\ 0 & \text{otherwise} \end{cases} \quad (1)$$

where, *C* is a dimensional constant coefficient that controls the magnitude of dust emission flux; *S* is the source function that characterizes the spatial distribution of dust emission; *U10m* is the horizontal wind speed at 10 m; *Ut* is the threshold velocity of wind erosion, which depends on particle size and wetness; and *Sp* is a fraction of mass emitted into size group *p*.

Table 1. Physical and chemical schemes used in the WRF-Chem simulations.

Simulation settings	**Values**
Domain size	390 × 250 cells
Horizontal resolution	9 km
Vertical resolution	51 levels up to 50 hPa
Time step for physics	60 s
Time step for chemistry	60 s
Physics options	**Used schemes**
Microphysics	WSM5
Longwave radiation	RRTM
Shortwave radiation	RRTMG
Surface layer	Revised MM5
Surface land	Noah and land surface model
Planetary boundary layer	YSU
Cumulus parametrization	Grell-3
Chemistry options	**Used schemes**
Chemistry	GOCART simple aerosol scheme, no ozone chemistry

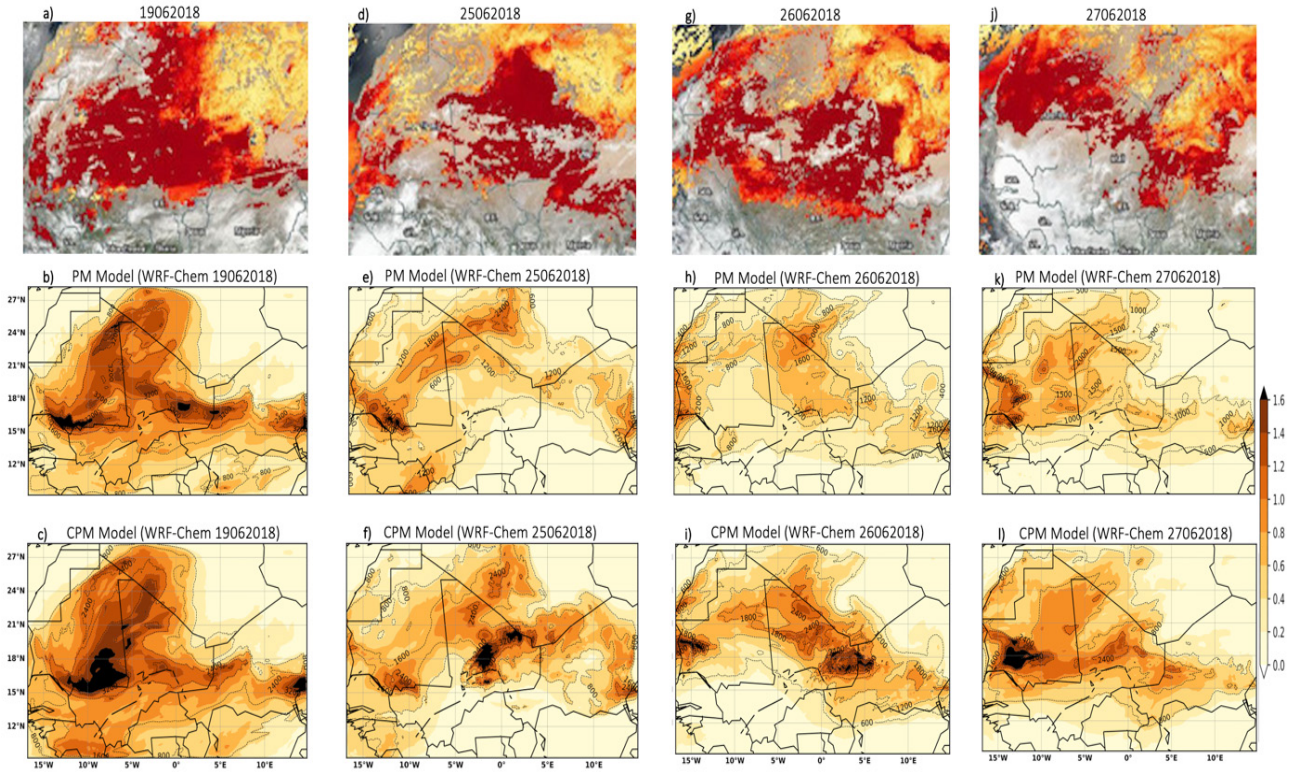

Figure 1. Daily mean AOD observed by NASA Worldview (top panel), daily average simulated AOD are shown by the color shading and PM10 concentration in $\mu g \cdot m^{-3}$ are represented by the black contour respectively by WRF-Chem Parameterized (PM) model (middle panel), and WRF-Chem Convection-permitting model (CPM) (bottom panel) on (a-b-c) 19 June 2018, on (d-e-f) 25 June, (g-h-i) on 26 June, and (j-k-l) on 27 June.

3. Results and discussion

3.1 Observations of synoptic situation

Figure 2 and **Figure 3** show the evolution of the synoptic-scale meteorology which has provided the formation of the MCS. The synoptic situation for this case study includes the mean sea-level pressure, the position of the ITD defined by the 14 °C isotherm of the 2 m dewpoint temperature, and the relative humidity for **Figure 2**. Complementary information for the synoptic situation is given in **Figure 3** and is based on the 200 hPa geopotential, 925 wind speed, and 925 hPa streamlines. The description of the synoptic situation covers twelve days from 16 to 27 June and uses the daily mean ERA5 Reanalysis. Ten (10) days before the event (16 June), a core of low pressure of 1008 hPa (**Figure 2a**) is located over North Mali and four (04) days after central Mali with a lower pressure of 1006 hPa (**Figure 2b**). This southward transport of the core of low pressure brings dry air masses from the northern Sahara to Sahel region up to 12°N. On 24 June, the monsoon trough is located further north involving a strong shift of the Intertropical Discontinuity (ITD) [22] to the south of Algeria (**Figure 2c**). On 23 June (**Figure 2d**), the ITD is almost zonal and located further north and the low-pressure core is located over the Western Africa coastal region. On the day of the event, the ITD is still further north and strong contrast is observed in the relative humidity between Sahara and Gulf of Guinea. From 24 to 26 June, there is an anticyclone characterizing by a high geopotential at the upper level over boundaries between Algeria, Mali and Mauritania and generating heavy dust emission over the same area as shown in **Figure 1**. This produces

a strong southward dust transport with high wind speed at 925 hPa and the southward shift of the ITD from south Algeria to northwest Niger (**Figure 2e**).

The thermodynamic properties of the cold pool are studied at the time of detection of the cold pool over Kayes and Matam (**Figures 4e** and **4f**) [42]. The haboob was detected at 0900 UTC over Kayes in western Mali (**Figure 4c**) and at 1000 UTC over Matam (**Figure 4d**) on 27 June. Sudden changes are associated with the location of the MCS over Eastern and Western Senegal both with a greater decrease of the temperature of about 9 °C [42]. The maximum wind speeds are obtained about 1-hour before the arrival of the MCS at the stations as already observed during the Fennec field campaign by Allen et al. [43].

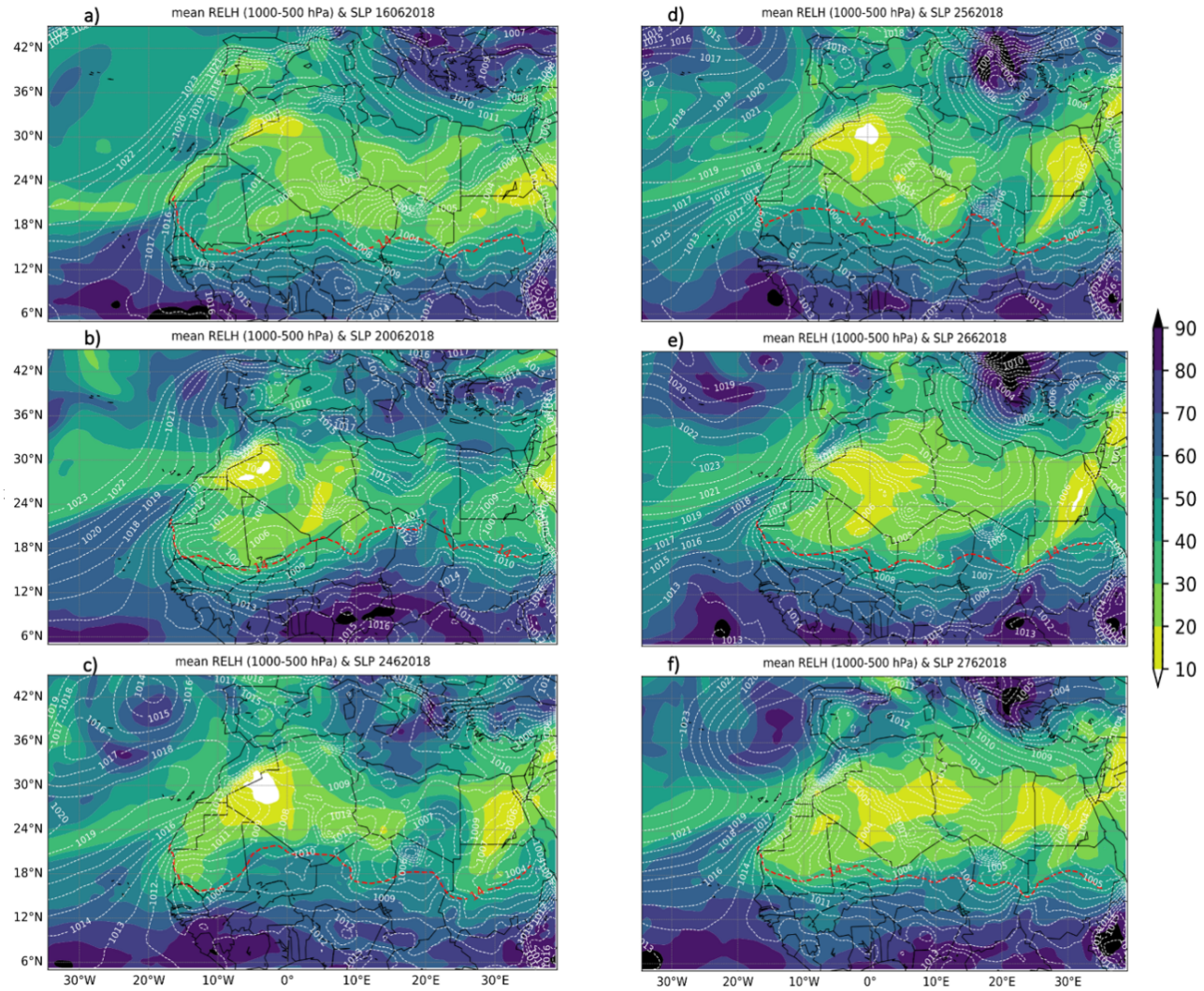

Figure 2. Synoptic state before and during the establishment of the haboob in the western Africa region on (a) 16 June 2018, (b) 20 June, (c) 24 June, (d) 25 June, (e) 26 June, and (f) 27 June. The ITD from ERA5 Re-Analysis is defined by the 14 °C isotherm of 2m dewpoint temperature (dashed red line), mean sea-level pressure in hPa (dashed with line) and relative humidity (color shading).

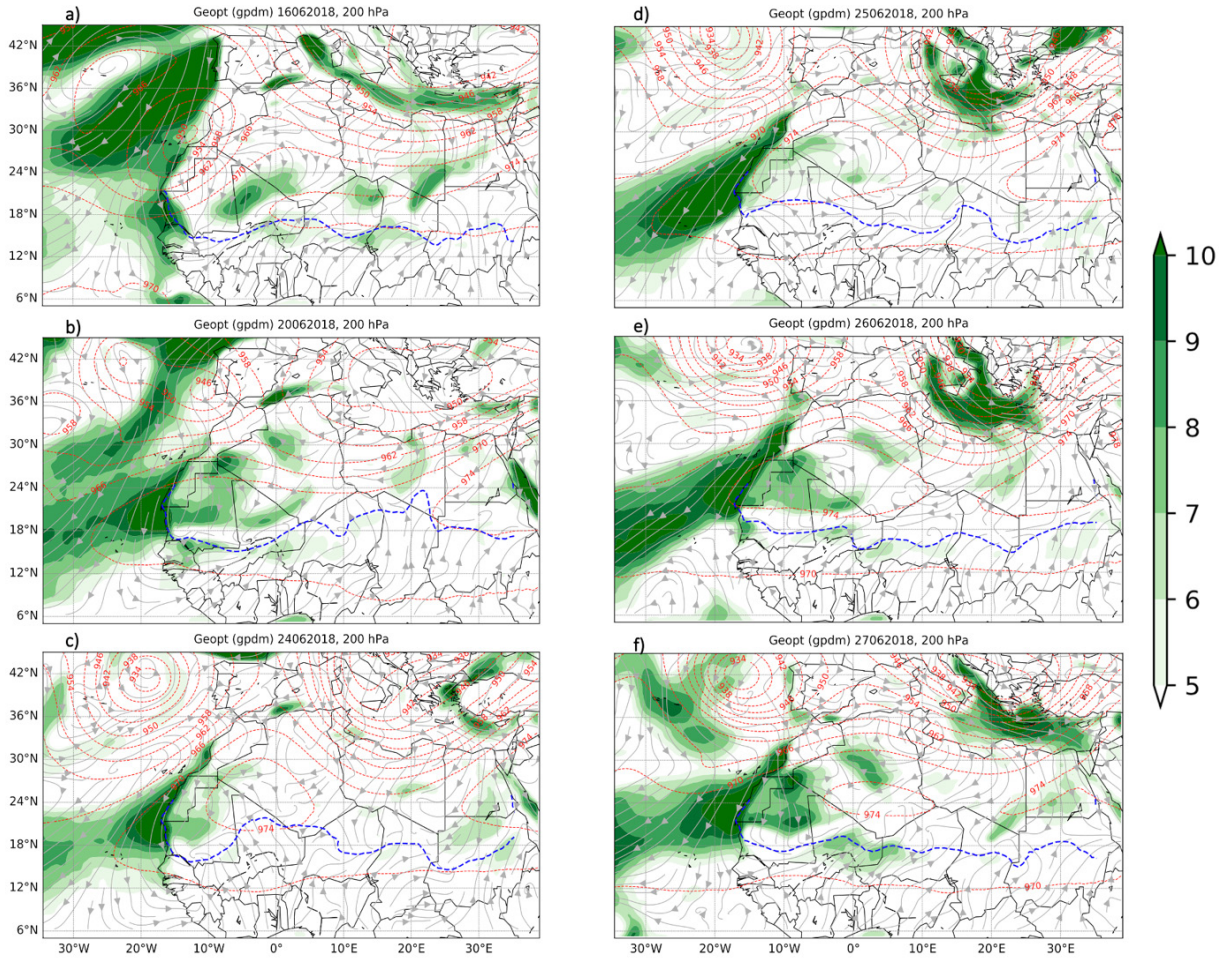

Figure 3. Synoptic state before and during the establishment of the haboob over the western Africa region on (a) 16 June 2018, (b) 20 June, (c) 24 June, (d) 25 June, (e) 26 June, and (f) 27 June. The ITD from ERA5 Re-Analysis is shown over land (dashed blue line), 200 hPa geopotential (dashed red line), 925 hPa wind speed (green shading) overlain with 925 hPa streamlines (grey).

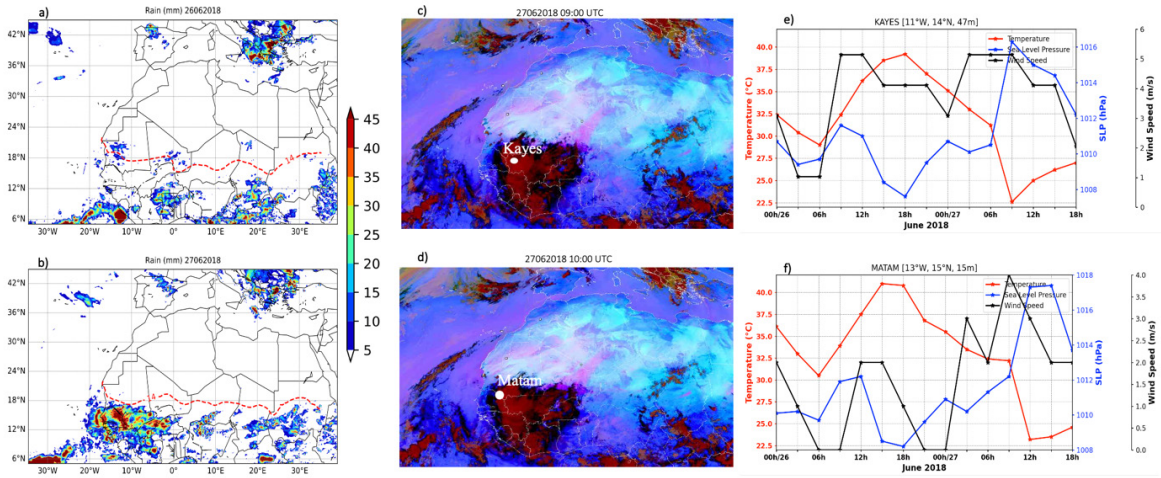

Figure 4. ITD from ERA5 (dashed red line), estimated 24 h accumulated rainfall from IMERG on (a) 26 June 2018, and (b) 27 June 2018. Spinning Enhanced Visual and Infrared Imager (SEVIRI) red, green, blue (RGB) dust image (c) at 0900 UTC 27 June 2018, and (d) at 1000 UTC 27 June 2018. Dust is represented by magenta, deep clouds by red, midlevel clouds by orange, cirrus clouds by black, and surface by blue, and white dots show the location of the synoptic station of Kayes (Mali) and Matam (Senegal). The synoptic measurement over Kayes and Matam are respectively shown in (e) and (f). The near-surface temperature is shown by the red line, the wind speed by the black line, and the sea-level pressure by the blue line.

3.2 Assessment of dust

To assess the aerosol integrated-column, we compare AOD from both simulations PM and CPM with the daily retrieved AOD from IASI and MODIS sensors over West Africa (17°W-15°E; 9°N-30°N) between 16 June and 29 June 2018 (**Figure 5a** and **Figure 1**). In General, the simulations conducted by a tuning factor of 1 $mg \cdot s^2 \cdot m^{-5}$ show a good replication of the magnitude and temporal evolution of observed AOD. Between 16 and 21 June, the diurnal variability of observed AOD is reproduced by simulations with a best agreement in the CPM (**Figure 5a** and **Figure 1**). Both simulations are in accordance with observations by capturing the maximum retrieved AOD between 17 and 20 June and minimum AOD between 22 and 29 June (**Figure 5a**). Both models did not match the maximum value of retrieved AOD by satellites on 20 June. The increase tendency of AOD on 25 June is also missed in simulations. **Figure 1** more details in the daily aerosol horizontal distribution of simulated and observed AOD which retrieved from Suomi NPP/VIIRS Deep Blue. The horizontal distribution of AOD showed that both models are able to reproduce the spatial distribution with a better accordance in the CPM. The shape of the dust plume is well replicated in the simulations with a maximum the PM10 concentration of 4000 $\mu g \cdot m^{-3}$ located over the maximum AOD values. On 19 June, the dust emissions were apparent strongly activated with a considerable contribution of Bodélé (Chad) dust source [44] and the Saharan dust source [45] located particularly over southern Algeria, and northern Mali and Mauritania. The magnitude of dust emission as shown by the observations and simulations decreases after 19 June, however the major dust contribution from sources cited above is maintained. On 27 June, when the dust storm occurs, the maximum PM10 isotherm of 2000 and 2400 $\mu g \cdot m^{-3}$ respectively in PM and CPM were located over southern Mauritania.

Figure 6 shows that emitted dust is strongly led by the 10-meter winds which exceed largely the wind threshold of 5.2 $m \cdot s^{-1}$ for desert dust emission [46]. The Outgoing Longwave Radiation (OLR) shows the evolution of the MCS identified by the minimum values less than 240 $W \cdot m^{-2}$ [47]. The MCS is clearly faster and finer in the CPM than in the PM (**Figure 6**). The MCS reaches the eastern boundaries of Senegal at 0000 UTC (**Figure 6a**) and 0300 UTC (**Figure 6d**) respectively in the PM and CPM models.

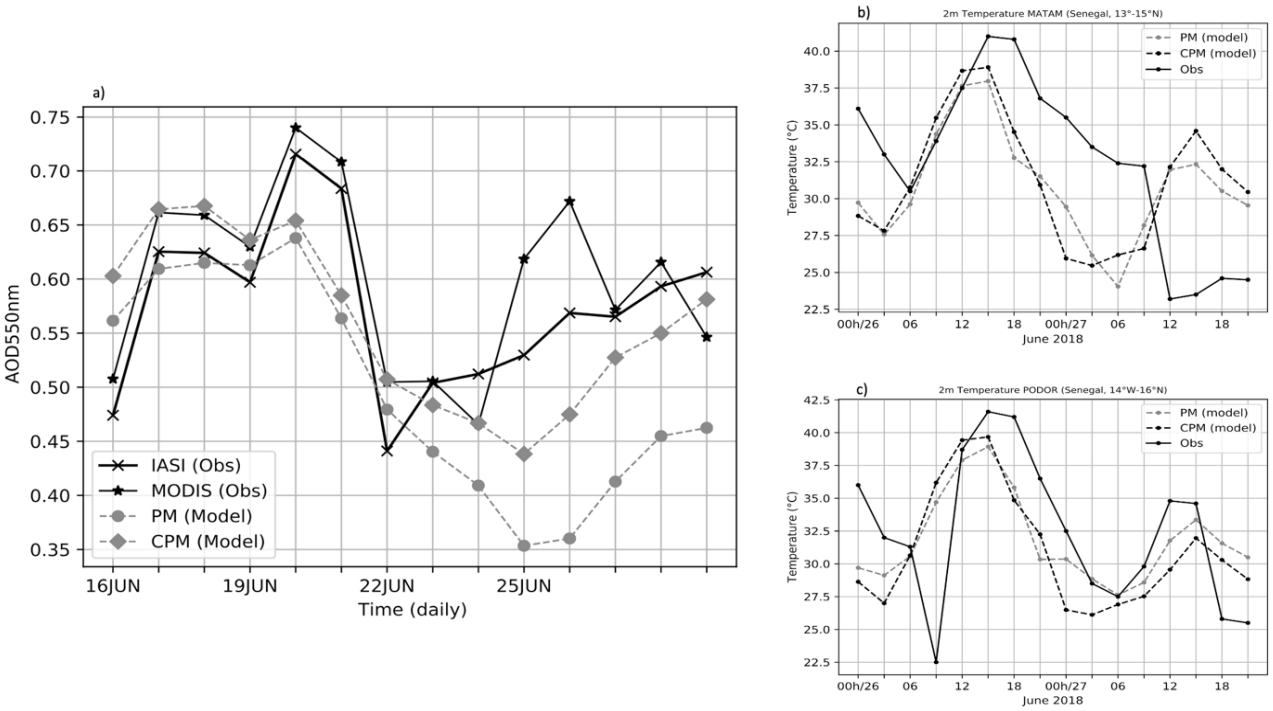

Figure 5. (a) Time series of AOD area averaged over Western Africa (17°W-15°E; 9°N-30°N) observed by MODIS (solid black line with stars) and IASI (solid black line with x signs) sensors, and simulated by the PM (dashed gray line with circles) and CPM (dashed gray line with squares) models between 16 June and 29 June 2018. (b) and (c) represent the sub-daily evolution of the 2-meter temperatures respectively over Matam and Podor with PM (dashed grey line), CPM (dashed black line), and observations (solid black line).

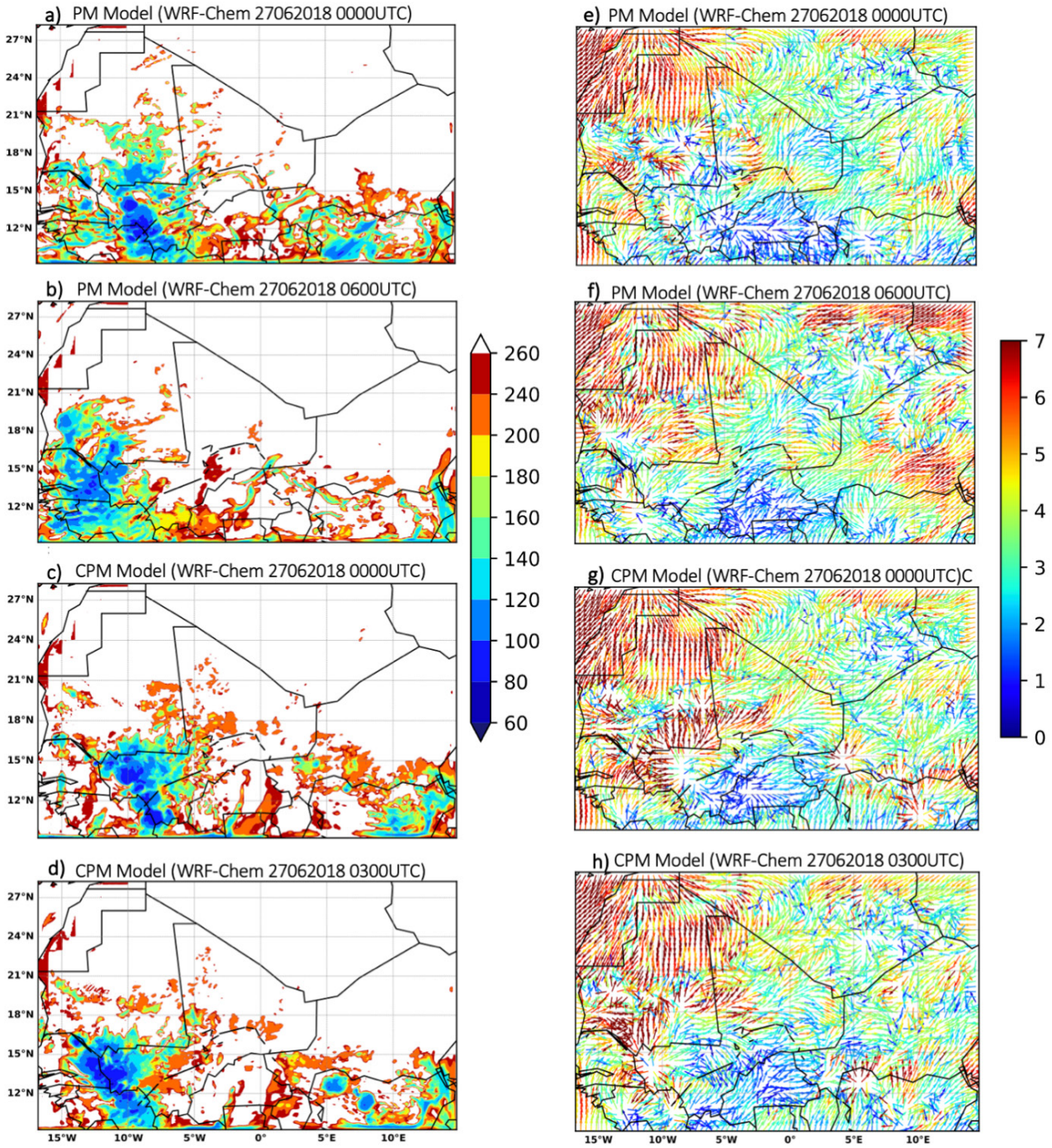

Figure 6. Outgoing Longwave Radiation (OLR) in W·m^{-2} respectively simulated by the PM at (a) 27 June 0000 UTC, (b) 27 June 0600 UTC, and CPM at (c) 27 June 0000 UTC and (d) 27 June 0300 UTC. 10-meter wind directions (arrow), and wind magnitudes (color shading) respectively simulated by PM at (a) 27 June 0000 UTC, (b) 27 June 0600 UTC, and CPM at (c) 27 June 0000 UTC and (d) 27 June 0300 UTC.

3.3 Environmental properties of the MCS

Figure 5c shows that both simulations reproduce the diurnal cycle of the surface temperature over the eastern side and northern side of Senegal with a better agreement with observation over Podor. Based on the surface temperature, simulations show an abrupt change related to the spreading of the MCS over West Africa on 26 and 27 June 2018 (**Figures 5b** and **4c** and **Figure 7**) as observed in synoptic scale (**Figures 4c** and **4d**). The minimum temperature shown by the observation at the detection time of the MCS over Matam is obtained in the simulations at 1200 UTC (**Figure 5**). **Figure 7i-7p** shows more details on the changes in 2-meter temperatures (T2m) induced by the MCS properties. By 2100 UTC on 26 June, significant dry air masses are located in the aerosol transect [48] over southern Algeria, northern Mali, southern Mauritania, and northeastern Senegal (**Figures 7i** and **7m**). By 0000 UTC on 27 June, a decrease of T2m of about 5 °C is noted on this transect when the MCS merged with northeastward convective cells (**Figures 7j** and **7n**). When the MCS is detected on the eastern side of Senegal and the western side of Mali (**Figures 6** and **7**), a significant gradient of temperature greater than 10 °C is obtained (**Figures 7k** and **7o**). By 1800 UTC on 27 June after the system spread away from West Africa, the situation becomes drier on the northern latitude 12°N (**Figures 7l** and **7p**).

The important transport of southwestward moisture, which is associated with oceanic air masses and powering the MCS on 27 June at 0000 UTC, is in **Figures 7b** and **7f** with precipitable water exceeding 50 mm. The cold pool is associated with 10-meter wind exceeding 20 $m \cdot s^{-1}$ and the migration of the ITD is located at northern Texte latitude 18°N during the event. The monsoon surge shown by the southwesterly wind direction at 925 hPa and the strong northward progression of the ITD transport humidity over the border of Mali-Algeria and Niger as already highlighted in a previous case study [22].

3.4 Vertical profile of storm environment

Figure 8 shows the differences in the thermodynamic structure preceding and associated with the spread of the cold pool. The atmosphere became increasingly moist, which is defined by the distance between the black and green lines, below 700 hPa when the MCS arrived at Matam with a maximum humidity located between 850 and 700 hPa in the PM model. The atmosphere is generally well mixed with the westward transport of air masses as shown in Figure 8 by wind directions above 800 hPa. The moisture transport is stronger in the PM than in CPM model (**Figure 8**), in contrast to the wind surface which shows respectively a magnitude contours of 11.5 $m \cdot s^{-1}$ and 24 $m \cdot s^{-1}$ (**Figure 7**). This result is in agreement with the founding [12], where authors showed that their Parameterized simulation has got a greater moisture convergence than their explicit model.

3.5 Impact of dust

In this section, we investigate the profile, T2m temperature, and daily precipitation between the Parameterized and explicit convection in WRF-Chem. On 27 June at 0000 UTC, the lowest atmosphere between the surface and 2 km is dryer in the explicit convection than in the model Parameterized (**Figures 8a** and **8c**). After the event on 27 June, the PM model showed heavy moisture between 850 hPa and 500 hPa (1.5 km to 3 km). The explicit convection is quick dryer at this altitude and above and is similar to the ERA5 vertical profile (not shown).

On 27 June, the observation from GPM-IMERG shows a spatial distribution of daily precipitation over the western Sahel, with a maximum over northern Burkina Faso, southern Mali, eastern Senegal, western African coastal, northern Nigeria and southwestern Niger (**Figure 9a**). The Parameterized and NODUST explicit convection models miss capture in general the maximum rain over West Africa expected in southeastern Senegal and overestimate the daily

precipitation in Central Senegal (**Figures 9b** and **9d**). However, the explicit convection captures well the spatial patterns of daily precipitation as shown by the observations except in central Mali, and southwestern Niger (**Figures 9c**). **Figure 10** shows the spatial patterns of T2m temperature between dust and no-dust explicit models. This shows that airborne dust clearly affects solar radiation by inducing a cooler surface temperature before the event (from 26 June 2100 UTC to 27 June 0000 UTC). The atmosphere is heated after dust plume transport over the Sahel on 27 June 1800 UTC (**Figure 10d**).

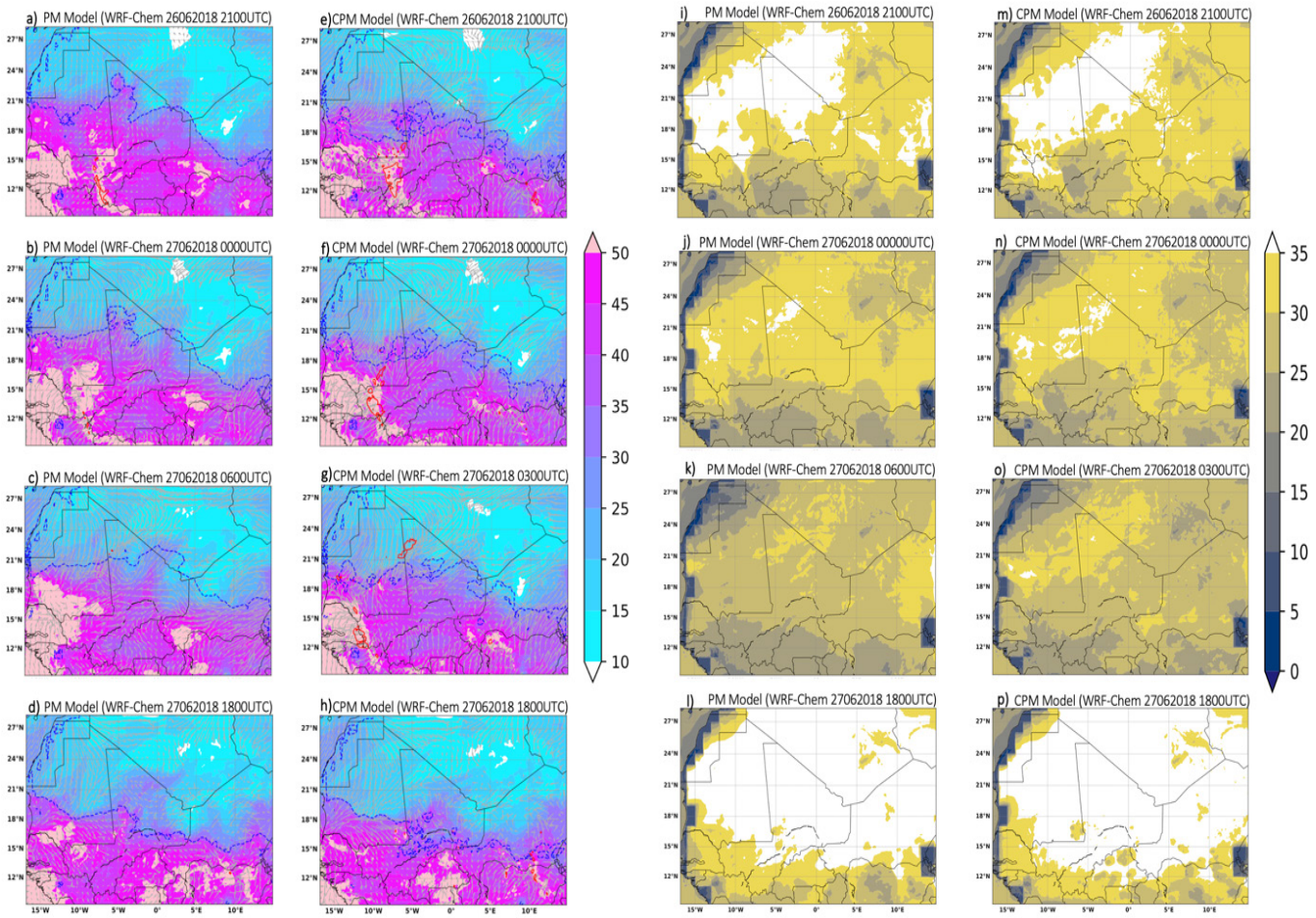

Figure 7. Precipitable Water Vapor (color shading) respectively simulated by the PM at (a) 26 June 2100 UTC, (b) 27 June 0000 UTC, (c) 27 June 0600 UTC, (d) 27 June 1800 UTC, and (e-h) by the CPM at the same time, and the ITD (dashed blue line) and 925 streamlines (grey). The 2 m surface temperature (color shading) respectively simulated by the PM (i-l), and the CPM (m-p) at the same time.

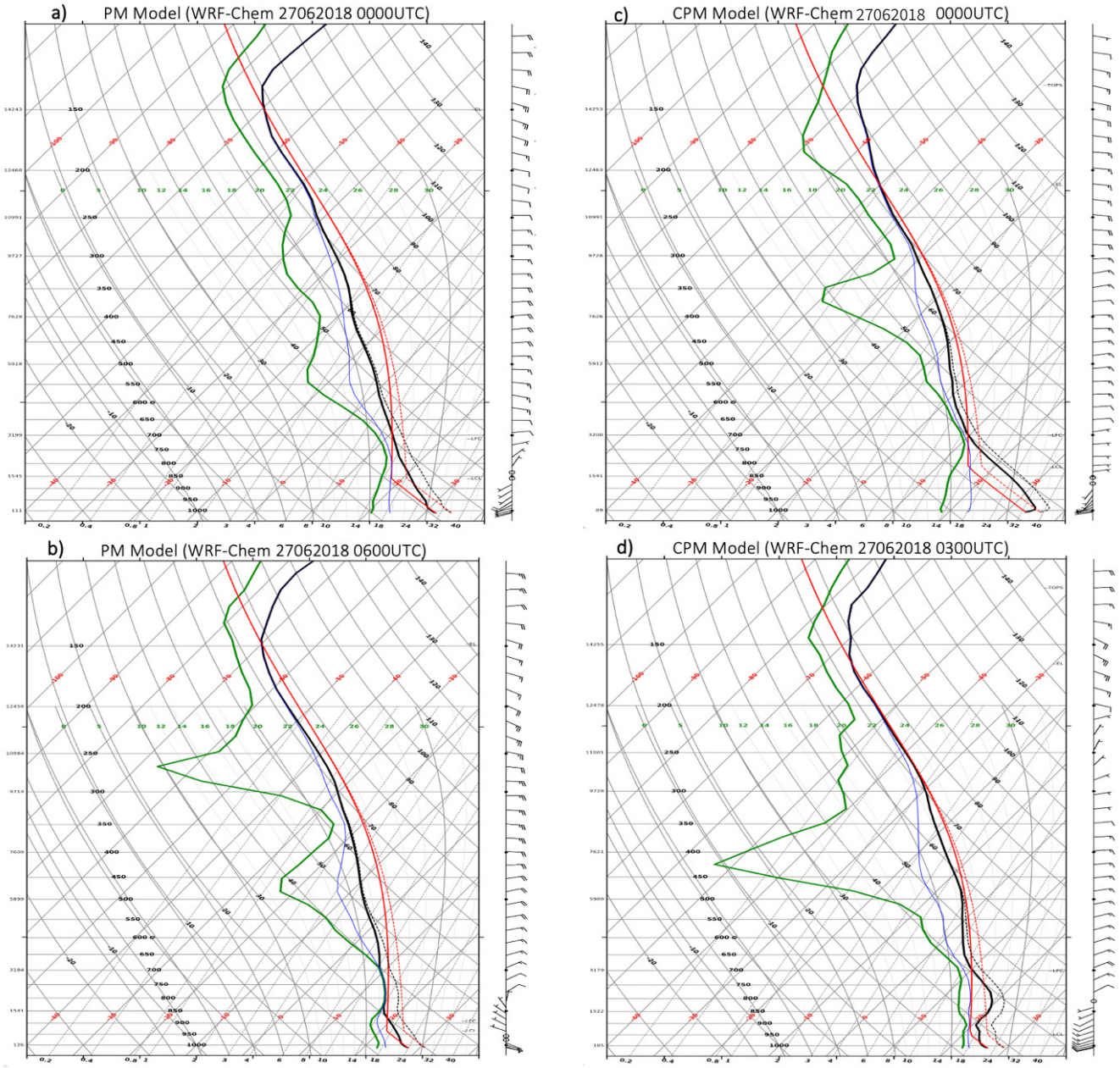

Figure 8. Skew-T diagram of simulated soundings over Matam (Senegal) respectively by the PM at (a) 27 June 0000 UTC, (b) 27 June 0600 UTC, and by the CPM at (c) 27 June 0000 UTC, and (d) 27 June 0300 UTC. Solid black and green show air and dew point temperatures (°C), and black wind barbs show the simulated winds in knots.

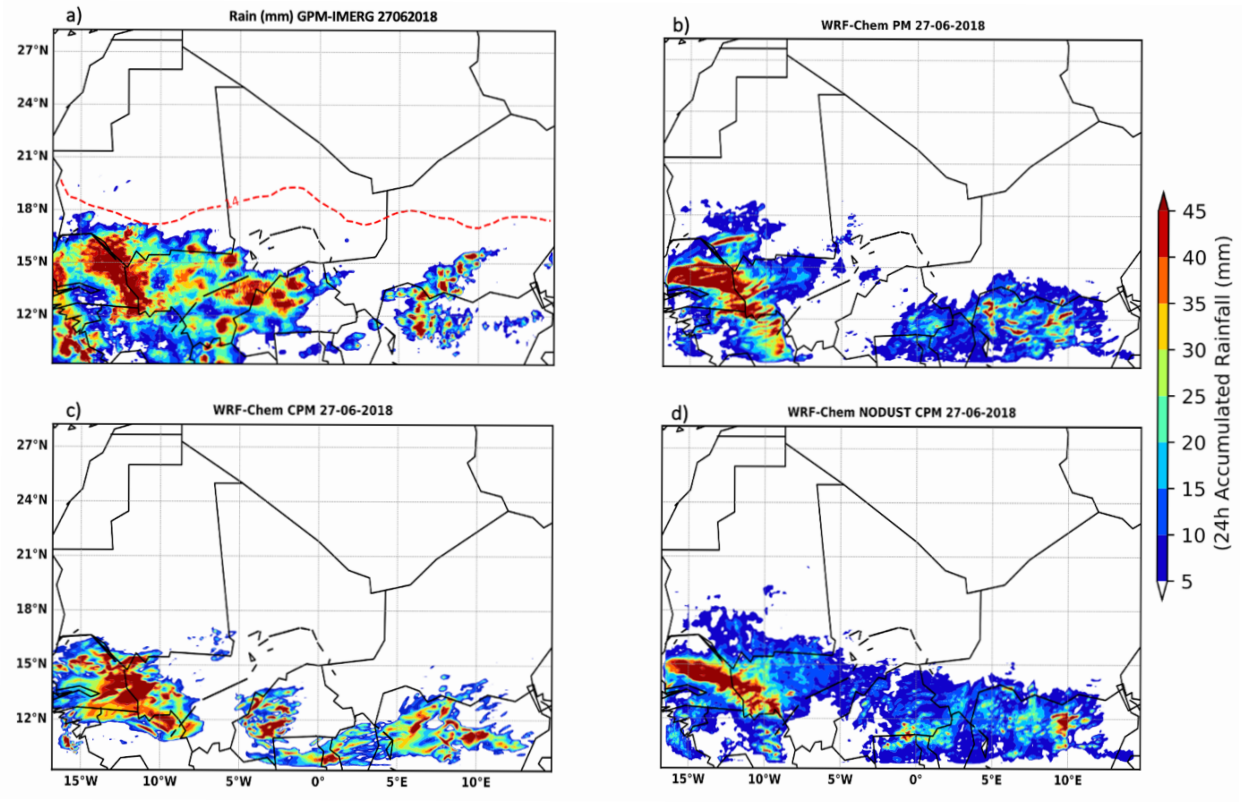

Figure 9. 24 h accumulated rainfall from GPM-IMERG (a), (b-d) accumulated modeled daily precipitation from respectively PM, CPM and NODUST models on 27 June.

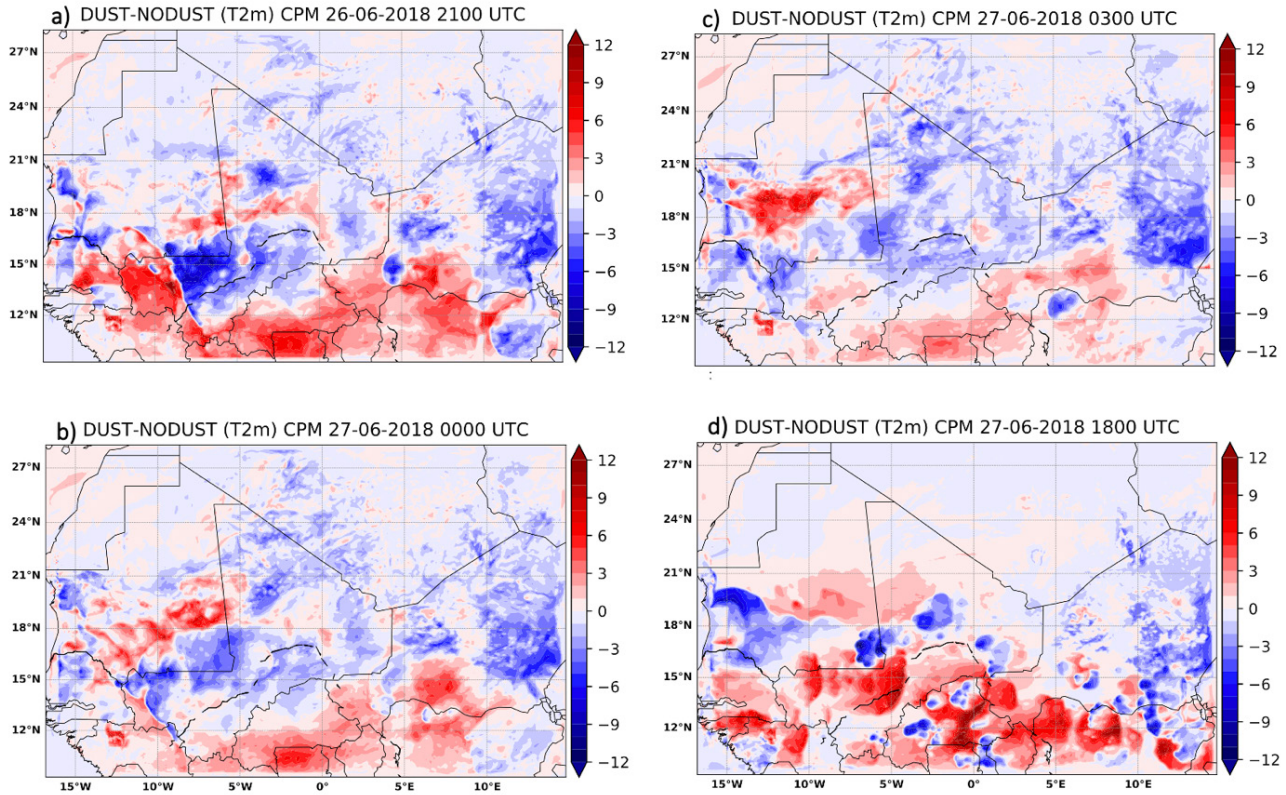

Figure 10. The difference in 2-meter temperatures (color shading) between Dust and NODUST CPM simulations at (a) 26 June 2100 UTC, (b) 27 June 0000 UTC, (c) 27 June 0300 UTC, and (d) 27 June 1800 UTC.

4. Conclusions

In this study, we have investigated the capability of WRF-chem model to capture a dust storm and the synoptic weather conditions that triggered a severe dust storm in West Africa between 26 and 27 June 2018 accompanied by the first precipitation in the early monsoon season. Observational data from synoptic stations and satellite estimations showed a typical characterization of a haboob event accompanied by a huge amount of dust mobilization along the LECCP. The West African weather is clearly improved in the CPM model with a better spatial pattern of the daily precipitation similar to the distribution shown by the satellite observations. The explicit convection model captures well the dust-generating winds, which are enough underestimated in the Parameterized convection model. The strong 10-meter winds have exceeded 20 m/s in the CPM model and 15 m/s in the PM model. These strong winds have induced heavy dust emission along the Sahelian dust transect and then impacted strongly the 2-m surface temperatures in both models. However, surface turbulence is better represented in the CPM than in the PM models. The heavy dust emitted in the CPM model has induced a strong gradient in the surface temperature with warmer and cooler air masses respectively onward and behind the MCS. The thermodynamic features showed that the characterization of haboob is matched in both simulations when the MCS spreading from North Burkina merges with small convective cells advected from central Mali on the night of 27 June 2018 as well as showed in the observations. The merging of the convective cells was coinciding with a strong southwest transport of air masses bringing moisture and then empowering the MCS.

Conflict of Interest

There is no conflict of interest.

Acknowledgment

The authors wish to thank the Global Challenges Research Fund (GCRF) African Science for Weather Information and Techniques (SWIFT) Programme. Thanks to NASA, CNES, ICARE and AERONET for providing access to CALIOP data and Sun photometer. We are grateful to the University Corporation for Atmospheric Research (UCAR) in Boulder, Colorado, for access to Cheyenne supercomputer.

References

[1] Levin, Z., Ganor, E., Gladstein, V., 1996. The effects of desert particles coated with sulfate on rain formation in the eastern Mediterranean. Journal of Applied Meteorology and Climatology. 35(9), 1511-1523.

[2] Wurzler, S., Reisin, T.G., Levin, Z., 2000. Modification of mineral dust particles by cloud processing and subsequent effects on drop size distributions. Journal of Geophysical Research: Atmospheres. 105(D4), 4501-4512.

[3] Rosenfeld, D., Rudich, Y., Lahav, R., 2001. Desert dust suppressing precipitation : A possible desertification feedback loop. Proceedings of the National Academy of Sciences. 98(11), 5975-5980.

[4] Martínez, I.R., Chaboureau, J.P., 2018. Precipitation and mesoscale convective systems : Radiative impact of dust over northern Africa. Monthly Weather Review. 146(9), 3011-3029.

[5] Camara, M., Jenkins, G., Konare, A., 2010. Impacts of dust on West African climate during 2005 and 2006. Atmospheric Chemistry and Physics Discussions. 10(2), 3053-3086.

[6] Kocha, C., Lafore, J., Tulet, P., et al., 2012. High-resolution simulation of a major West African dust-storm : Comparison with observations and investigation of dust impact. Quarterly Journal of the Royal Meteorological Society. 138(663), 455-470.

[7] Chaboureau, J., Tulet, P., Mari, C., 2007. Diurnal cycle of dust and cirrus over West Africa as seen from Meteosat Second Generation satellite and a regional forecast model. Geophysical Research Letters. 34(2).

[8] Janiga, M.A., Thorncroft, C.D., 2014. Convec-

tion over tropical Africa and the east Atlantic during the West African monsoon : Regional and diurnal variability. Journal of Climate. 27(11), 4159-4188.

[9] Mathon, V., Laurent, H., Lebel, T., 2002. Mesoscale convective system rainfall in the Sahel. Journal of Applied Meteorology. 41(11), 1081-1092.

[10] Roberts, A., Knippertz, P., 2014. The formation of a large summertime Saharan dust plume : Convective and synoptic-scale analysis. Journal of Geophysical Research: Atmospheres. 119(4), 1766-1785.

[11] Lin, Y.L., 2007. Mesoscale convective systems. Mesoscale dynamics. Cambridge University Press: Cambridge. pp. 322-378. DOI: https://doi.org/10.1017/CBO9780511619649.010

[12] Finney, D.L., Marsham, J.H., Rowell, D.P., et al., 2020. Effects of explicit convection on future projections of mesoscale circulations, rainfall, and rainfall extremes over Eastern Africa. Journal of Climate. 33(7), 2701-2718.

[13] Birch, C., Parker, D., Marsham, J., et al., 2014. A seamless assessment of the role of convection in the water cycle of the West African monsoon. Journal of Geophysical Research: Atmospheres. 119(6), 2890-2912.

[14] Marsham, J.H., Dixon, N.S., Garcia-Carreras, L., et al., 2013. The role of moist convection in the West African monsoon system : Insights from continental-scale convection-permitting simulations. Geophysical Research Letters. 40(9), 1843-1849.

[15] Marsham, J.H., Knippertz, P., Dixon, N.S., et al., 2011. The importance of the representation of deep convection for modeled dust-generating winds over West Africa during summer. Geophysical Research Letters. 38(16).

[16] Pope, R., Marsham, J., Knippertz, P., et al., 2016. Identifying errors in dust models from data assimilation. Geophysical Research Letters. 43(17), 9270-9279.

[17] Hohenegger, C., Schlemmer, L., Silvers, L., 2015. Coupling of convection and circulation at various resolutions. Tellus A: Dynamic Meteorology and Oceanography. 67(1), 26678.

[18] Prein, A.F., Langhans, W., Fosser, G., et al., 2015. A review on regional convection-permitting climate modeling : Demonstrations, prospects, and challenges. Reviews of Geophysics. 53(2), 323-361.

[19] Crook, J., Klein, C., Folwell, S., et al., 2019. Assessment of the representation of West African storm lifecycles in convection-permitting simulations. Earth and Space Science. 6(5), 818-835.

[20] Stratton, R.A., Senior, C.A., Vosper, S.B., et al., 2018. A pan-African convection-permitting regional climate simulation with the Met Office Unified Model : CP4-Africa. Journal of Climate. 31(9), 3485-3508.

[21] Jackson, L.S., Keane, R.J., Finney, D.L., et al., 2019. Regional differences in the response of rainfall to convectively coupled Kelvin waves over tropical Africa. Journal of Climate. 32(23), 8143-8165.

[22] Trzeciak, T.M., Garcia-Carreras, L., Marsham, J.H., 2017. Cross-Saharan transport of water vapor via recycled cold pool outflows from moist convection. Geophysical Research Letters. 44(3), 1554-1563.

[23] Brindley, H., Knippertz, P., Ryder, C., et al., 2012. A critical evaluation of the ability of SEVIRI thermal IR RGB rendering to identify dust events. Part A: Theoretical analysis. Geophysical Research Letters. 117, D07201.

[24] Sayer, A., Munchak, L., Hsu, N., et al., 2014. MODIS Collection 6 aerosol products : Comparison between Aqua's e-Deep Blue, Dark Target, and "merged" data sets, and usage recommendations. Journal of Geophysical Research: Atmospheres. 119(24), 13-965.

[25] Clarisse, L., Coheur, P.F., Prata, F., et al., 2013. A unified approach to infrared aerosol remote sensing and type specification. Atmospheric Chemistry and Physics. 13(4), 2195-2221.

[26] Hsu, N., Jeong, M., Bettenhausen, C., et al., 2013. Enhanced Deep Blue aerosol retrieval algorithm : The second generation. Journal of

Geophysical Research: Atmospheres. 118(16), 9296-9315.

[27] Sayer, A., Hsu, N., Lee, J., et al., 2018. Satellite Ocean Aerosol Retrieval (SOAR) algorithm extension to S-NPP VIIRS as part of the "Deep Blue" aerosol project. Journal of Geophysical Research: Atmospheres. 123(1), 380-400.

[28] Wei, G., Lü, H., Crow, W.T., et al., 2018. Comprehensive evaluation of GPM-IMERG, CMORPH, and TMPA precipitation products with gauged rainfall over mainland China. Advances in Meteorology. 3024190.

[29] Hersbach, H., Bell, B., Berrisford, P., et al., 2020. The ERA5 global reanalysis. Quarterly Journal of the Royal Meteorological Society. 146(730), 1999-2049.

[30] Grell, G.A., Peckham, S.E., Schmitz, R., et al., 2005. Fully coupled "online" chemistry within the WRF model. Atmospheric Environment. 39(37), 6957-6975.

[31] Ginoux, P., Chin, M., Tegen, I., et al., 2001. Sources and distributions of dust aerosols simulated with the GOCART model. Journal of Geophysical Research: Atmospheres. 106(D17), 20255-20273.

[32] Hong, S.Y., Noh, Y., Dudhia, J., 2006. A new vertical diffusion package with an explicit treatment of entrainment processes. Monthly Weather Review. 134(9), 2318-2341.

[33] Chen, F., Dudhia, J., 2001. Coupling an advanced land surface-hydrology model with the Penn State—NCAR MM5 modeling system. Part I: Model implementation and sensitivity. Monthly Weather Review. 129(4), 569-585.

[34] Jiménez, P.A., Dudhia, J., González-Rouco, J.F., et al., 2012. A revised scheme for the WRF surface layer formulation. Monthly Weather Review. 140(3), 898-918.

[35] Iacono, M.J., Delamere, J.S., Mlawer, E.J., et al., 2008. Radiative forcing by long-lived greenhouse gases : Calculations with the AER radiative transfer models. Journal of Geophysical Research: Atmospheres. 113(D13).

[36] Mlawer, E.J., Taubman, S.J., Brown, P.D., et al., 1997. Radiative transfer for inhomogeneous atmospheres : RRTM, a validated correlated-k model for the longwave. Journal of Geophysical Research: Atmospheres. 102(D14), 16663-16682.

[37] Grell, G.A., Dévényi, D., 2002. A generalized approach to parameterizing convection combining ensemble and data assimilation techniques. Geophysical Research Letters. 29(14), 381-384.

[38] Hong, S.Y., Dudhia, J., Chen, S.H., 2004. A revised approach to ice microphysical processes for the bulk parameterization of clouds and precipitation. Monthly Weather Review. 132(1), 103-120.

[39] Jenkins, G.S., Gueye, M., 2018. WRF 1960-2014 winter season simulations of particulate matter in the Sahel : Implications for air quality and respiratory health. GeoHealth. 2(8), 248-260.

[40] Khan, B., Stenchikov, G., Weinzierl, B., et al., 2015. Dust plume formation in the free troposphere and aerosol size distribution during the Saharan mineral dust experiment in North Africa. Tellus B: Chemical and Physical Meteorology. 67(1), 27170.

[41] Ukhov, A., Mostamandi, S., da Silva, A., et al., 2020. Assessment of natural and anthropogenic aerosol air pollution in the Middle East using MERRA-2, CAMS data assimilation products, and high-resolution WRF-Chem model simulations. Atmospheric Chemistry and Physics. 20(15), 9281-9310.

[42] Senghor, H., Roberts, A.J., Dieng, A.L., et al., 2021. Transport and deposition of Saharan dust observed from satellite images and ground measurements. Journal of Atmospheric Science Research. 4(2), 1-11.

[43] Allen, C.J., Washington, R., Engelstaedter, S., 2013. Dust emission and transport mechanisms in the central Sahara : Fennec ground-based observations from Bordj Badji Mokhtar, June 2011. Journal of Geophysical Research: Atmospheres. 118(12), 6212-6232.

[44] Washington, R., Bouet, C., Cautenet, G., et al.,

2009. Dust as a tipping element : The Bodélé Depression, Chad. Proceedings of the National Academy of Sciences. 106(49), 20564-20571.

[45] Alonso-Pérez, S., Cuevas, E., Querol, X., et al., 2012. African dust source regions for observed dust outbreaks over the subtropical Eastern North Atlantic region, above 25 N. Journal of Arid Environments. 78, 100-109.

[46] Westphal, D.L., Toon, O.B., Carlson, T.N., 1987. A two-dimensional numerical investigation of the dynamics and microphysics of Saharan dust storms. Journal of Geophysical Research: Atmospheres. 92(D3), 3027-3049.

[47] Kousky, V.E., 1988. Pentad outgoing longwave radiation climatology for the South American sector. Revista Brasileira de Meteorologia. 3(1), 217-231.

[48] Mortier, A., Goloub, P., Derimian, Y., et al., 2016. Climatology of aerosol properties and clear-sky shortwave radiative effects using Lidar and Sun photometer observations in the Dakar site. Journal of Geophysical Research: Atmospheres. 121(11), 6489-6510.

BILINGUAL PUBLISHING GROUP

Journal of Atmospheric Science Research
https://journals.bilpubgroup.com/index.php/jasr

ARTICLE

Co-designed Practical Use of Probabilistic Climate Advisories among Smallholder Farmers: A Balance between Confidence and Caution

***Mary Mwangi*[1*], *Evans Kituyi*[2], *Gilbert Ouma*[2]**

[1] *South Eastern Kenya University, Kitui, 90200, Kenya*
[2] *Institute of Climate Change and Adaptation, University of Nairobi, Nairobi, 00625, Kenya*

ABSTRACT

Especially for smallholder farmers with limited land and financial resources, farming in arid and semi-arid lands (ASALs), where season-to-season rainfall fluctuation dictates production, is a risky business. Through participatory approaches, this study compares deterministic and probabilistic interpretations of climate forecasts and their use by smallholder farmers through a crop-growing season. The study revealed that deterministic advisories are good for smallholder farmers only when formulated from forecasts with higher accuracy than the historical climatological distribution. Otherwise, they cause farm loss in terms of labor and inputs. On the other hand, probabilistic advisories help farmers spread the risk to cater to all the uncertainty and in so doing bring out a balance between confidence and caution. However, farmers must be supported with enough sensitization to comprehend forecast probability, translate it into probabilistic advisories and use that to plan and manage farm activities. The findings support the hypothesis providing packaged climate products in transparent probabilistic terms in place of deterministic form can overcome inherent credibility challenges. The study's conclusion highlights important takeaways and new understandings of the advantage of using probabilistic advisories among resource-poor smallholder farmers.

Keywords: Smallholder farmers; Deterministic advisories; Probabilistic advisories

1. Introduction

Climate information access and use have been proven to help vulnerable communities such as smallholder farmers to better manage climate risks and maximize the opportunities posed by the same.

*CORRESPONDING AUTHOR:
Mary Mwangi, South Eastern Kenya University, Kitui, 90200, Kenya; Email: wmwangi@seku.ac.ke

ARTICLE INFO
Received: 02 March 2023 | Revised: 12 April 2023 | Accepted: 14 April 2023 | Published Online: 19 April 2023
DOI: https://doi.org/10.30564/jasr.v6i2.5511

CITATION
Mwangi, M., Kituyi, E., Ouma, G., 2023. Co-designed Practical Use of Probabilistic Climate Advisories among Smallholder Farmers: A Balance between Confidence and Caution. Journal of Atmospheric Science Research. 6(2): 75-82. DOI: https://doi.org/10.30564/jasr.v6i2.5511

COPYRIGHT
Copyright © 2023 by the author(s). Published by Bilingual Publishing Group. This is an open access article under the Creative Commons Attribution-NonCommercial 4.0 International (CC BY-NC 4.0) License. (https://creativecommons.org/licenses/by-nc/4.0/).

Technological advancement in the collecting, processing and communicating climate information services has led to improved availability of climate information services. However, uptake of these services among the resource-poor smallholder farmers especially in the dryland regions of Sub-Saharan Africa is still low [1,2]. The credibility issues associated with climate services are among the many inhibitors of improved uptake [1,2].

Forecasters can only provide probabilistic forecasts rather than saying with certainty whether a certain region will receive wet or dry conditions during a particular time scale, for instance, a crop growing season. However, meteorological services providers especially in Sub Saharan Africa do not communicate forecasts in their full probabilistic form but rather translate them into deterministic terms based on the highest tercile probability [3] (Tercile probabilities are the forecast probabilities that the rainfall amount in a particular season will be in the lower 33.3% of the climatology hence dry, the middle 33.3%, hence normal rainfall, or the upper 33.3%, hence wet season). They do this under the impression that providing users with information about forecast probability will confuse them. In this line of thought, deterministic interpretation of the forecasts is then used to formulate deterministic advisories. For instance, if the season forecast says there is a 45%, 30%, and 25% probability of having above-normal, normal and below-normal rainfall respectively, the communicated forecast will be the one with the highest probability of occurrence and in this case, above-normal rainfall. From this forecast, a deterministic advisory is issued advising the farmers to plant seed varieties appropriate for above normal rainfall. This is a deterministic advisory based on a probabilistic forecast. This approach works perfectly well when there is a minimal deviation between the forecast and the observed. Otherwise, if the rainfall event during the season does not unfold exactly as predicted, the providers carry the blame for faulty predictions and farmers' trust in the forecast starts to dwindle. Hence there is a loss of credibility resulting in very poor uptake of climate information services.

In the context of attempts to improve climate information services adoption, this research article provides an overview of the practical use of probabilistic advisories. On the basis of participatory approach methods, this research engaged 327 smallholder farmers through a crop-growing season with the use of a probabilistic derived advisories. As would be expected, revealing forecast uncertainty and considering the same in the formulation of advisories has the potential to uphold the credibility of climate services and hence lead to improved adoption of these services. The results also indicate that trained farmers can understand forecast inherent limitations especially in terms of uncertainty, which disapproves the line of thought that revealing forecast uncertainty confuses the users.

Addressing the issue of credibility is essential to comprehend the value of climate and weather forecasts in support of agricultural decision-making. This constraint can result from past inaccurate forecasts, which can easily occur from forecasts that are communicated in deterministic form and from which a deterministic advisories are formulated. Climate application research has underscored the danger of interpreting climate predictions deterministically [1,4-7]. While communicating forecasts in probabilistic form may be difficult, these authors contend that forecasts should be communicated in full probabilistic form. Past research has suggested that climate service users especially smallholder farmers have difficulties understanding forecast probability especially because the producers do not present and explain them well [7-9] and hence it may be better to disseminate a deterministic version instead. Recent proponents argue that if farmers' ability to understand and use probabilistic forecasts is enhanced, they are able to understand the forecast's limitations and this increases their trust in the forecasts [10-13].

This article's focus is on seasonal climate forecast users (smallholder farmers in an arid and semi-arid region in Kenya), who face a myriad of pressures ranging from land degradation, increasing climate variability, land fragmentation and market forces, and who must make wise decisions to be self-suffi-

cient with respect to household food security [14-16]. With technological advancement, climatologists are able to forecast seasonal rainfall and disseminate it to smallholder farmers in Sub Saharan Africa. However, these forecasts are highly uncertain, and forecasters do not report this uncertainty for fear that they will confuse the users [17-21]. Using experimental methodology with smallholder farmers in Kitui County, one of the drylands of Kenya, the research examines whether reporting forecast uncertainty can help to improve forecast credibility among resource-poor smallholder farmers. In this regard, the study sought to know whether more forecast credibility would lead to increased levels of adoption of forecasts at the farm level.

2. Methodology

2.1 Sampling procedure

The mixed farming climatic zones within the county include low midland 5 (LM5), low midland 4 (LM4), and upper midland 4 (UM4). A sampling frame that was stratified according to the wards' position in the mixed agricultural climatic zones yielded the identification of three wards. The wards were specifically chosen due to their location in the mixed farming climate zones as follows Kyangwithia westward (which occupies 93% of the LM5 climatic zone and 7% of the LM4 climatic zone), Matinyani ward (which occupies 100% of the UM4 climatic zone), and Kwa-Vonza ward (which occupies 73% of the LM5, and 6% of the LM4). County wards located outside the mixed farming climatic zones were left out. The village names in each of the three wards were arranged in alphabetical order to guarantee a random selection of villages. Every fourth village was chosen to ensure that associated biases would not affect the systematic selection. The results of this sampling were as shown in **Table 1**. One farmer group was specifically identified in each of the chosen villages on the premise that it owned a group farm and had at least 15 active members. As a result, three farmer groups were created as study units. The farm groups are group owned and farming is done the same as on individual farms.

Table 1. Villages, wards and livelihood zones.

Agro-Climatological Zone	**UM4**	**LM4**	**LM5**
Wards	Kyangwithya west	Matinyani	Kwa-Vonza
Villages	Mbusyani,	Kathuma,	Kawongo / Kathome
	Mulutu,	Kauma,	Makusya,
	Ndumoni	Kavuvuu,	Mikuyuni,
	Tungutu**	Kitumbi**	Kyosini**
		Kyambusya,	Muvitha / Kathemboni
		Kyondoni,	Ndunguni,
		Maseki,	Nyaanyaa,
		Musosya,	
		Nzakame,	

** indicates the study units.

2.2 Stakeholder engagement and capacity building

The study worked with the smallholder farmers to identify the local stakeholders they partner with in relation to climate services. The identified stakeholders included local agricultural extension officers and seed suppliers. Pre-seasonal meetings were used to involve stakeholders and help them better understand the terminology used in climate services, establish their roles in providing climate services to farmers, and assist in the effective use of probabilistic seasonal forecasts. Via an iterative process, the stakeholders were involved in the October November December (OND) 2021 season. The first stage of interaction centered on enhancing stakeholders' climate understanding, using seasonal forecast data at the farm level, and highlighting the probabilistic nature of projections. The second phase concentrated on enhancing the stakeholders' abilities to evaluate probabilistic forecast data in terms of farm management choices. The timelines for the research activities during the season were as shown in **Figure 1**.

2.3 The provision and use of climate services (probabilistic forecasts combined with advisories)

On the 11th day of September 2021, the initial suites of climate services were introduced to the study sites. The source was the Kenya Meteorological Department. The default tercile probabilities, or probability of the below-normal, normal, and above-normal categories, of expected seasonal rainfall totals supplemented with commencement and cessation dates, were used as the structure of the downscaled seasonal forecast for the study. The demonstration farms consisted of three group farms. The group farms were in distant wards across the county. The main aim behind the involvement of the farm groups was to reinforce the usability of climate information through demonstration effects. It was envisaged that the demonstration would lead the skeptical farmers to adopt the use of climate information after witnessing proof of its effectiveness. In other words, the use of transparent probabilistic forecasts will reinforce trust in the forecasts.

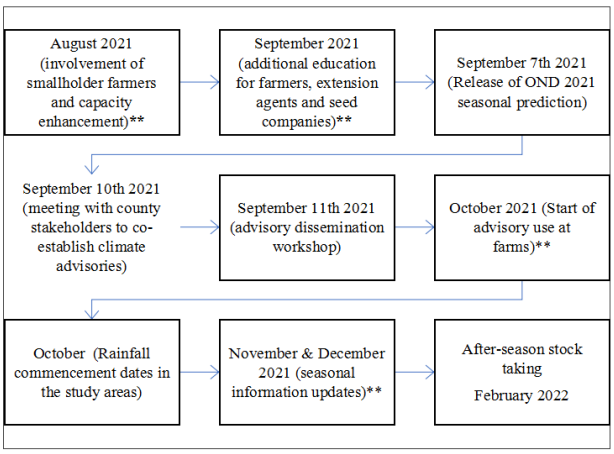

Figure 1. Timelines for OND 2021 activities.

** indicates activities that were carried out iteratively.

In the three demonstration farms, farming activities were directed by a tercile probability forecast. To increase the legitimacy of the process, and to aid social learning (in as far as farm-level use of probabilistic forecast is concerned), discussions and exchange of thoughts were encouraged among the participants in order to brainstorm on the best way to interpret and implement forecast probabilities. As a result of these inclusive deliberations, a scheme to interpret and put into use forecast probabilities at the farm level was co-designed. All the stakeholders agreed that each demonstration farm should be divided into three parts since the forecast probability terciles were three. In this way, the percentages assigned to each probable group were used in the co-designed plan to determine how much acreage to allot to each category. In addition, appropriate seed varieties were also selected for each probability category. For instance, if the forecast gave a 50%, 30% and 20% probability of above normal rains, normal and below normal rains respectively; then 50% of the demonstration land was allocated seed varieties suitable for above normal rain, 30% of the demonstration land was allocated seed varieties suitable for normal rain, and 20% of the demonstration land was allocated seed varieties suitable for below normal rains.

This division of land, for each of the demonstration farms, was done by the respective participating farmers in each farm. The extension staff and seed suppliers assisted the farmers in the selection of appropriate seed varieties for each tercile probability to account for the entire projected uncertainty range. Farmers were urged to use their judgment to segment each study site into three pieces, each of which was equal to the various percentage probability groups, rather than engaging in long quantitative calculations. As the season continued, stakeholders were regularly updated with seasonal information in dekadal weather reports via phone calls or brief text messages. After receiving farmers' comments during the research, the delivery of climate services was changed as necessary.

2.4 After-season evaluation

In order to gather farmers' opinions on the overall results of the selected probability forecast interpretation system as well as the efficiency of the delivery of climate services, a post-season evaluation was carried out after the conclusion of the crop growing season. Focus group conversations with

participating farmers were used to accomplish this. Of specific interest, group discussions sought to participate farmers' views on whether: 1) the farm subdivision and the subsequent planting of appropriate cultivars on each subdivision as indicated by the tercile probabilities supported farmers' climate risk management, 2) the scheme enabled spreading of climate risk compared to banking on the deterministic forecast, which is based on the highest tercile forecast probability and which, at times can be wrong and 3) this bottom-up approach of forecast probability interpretation brings a balance between caution and confidence in the use climate services at the farm level. In addition to the focus group discussions, the research also attempted to estimate crop yields in each group farm subdivision in the three study sites. This was done using the test weight pre-estimation method.

3. Results and discussions

On the group farms, farming operations were directed by estimated probabilities for OND 2021. This was released with a three-week lead period, allowing for advanced planning. As was indicated in Section 2.3, farmers divided the demonstration farms into three parts to cover all the tercile probabilities. On each sub-division they planted appropriate seeds for the respective probability tercile. **Table 2** presents a summary of the three group farms, the forecast probability that was issued for each of these group farms, the proportioning of the group farms and the appropriate seed varieties that were planted on each farm sub-division.

In **Table 2**, *Pioneer P28*, *Duma 43*, *DH 02*, *DK8031* and sungura are maize seed varieties while *Nyayo*, *Kat X 56* and *Kayelo* are bean seed varieties suitable for different seasonal rainfall amounts as shown in the table.

After-season evaluation results

Focus group conversations with participating farmers suggested that for the first time, farmers had received seasonal forecasts in probability form and understood how to translate them into farm decisions. The discussions also pointed out that the use of different seed varieties as dictated by probability terciles worked as a mechanism for crop diversification, which enabled the farmers spread the climate risk. The group farms' distribution to account for terciles in all likelihood brought some harmony between caution and certainty, (that is, a balance between reducing risks and increasing returns) unlike before when farmers indicated to have been used to frequent climate-related losses. The individual farms, on the other hand, were planted according to the prediction group with the highest likelihood.

Table 2. Chosen seed varietals sowed on each farm segment to account for all probable forecast groups.

Group farm	Forecast probability		Partitioning of the group farms to distribute the risk
Kanzoya	A	50%	Sow 50% of the acreage with *Pioneer P28* Sow 30% of the acreage with *Duma 43* Sow 20% of the acreage with *DH02*
	N	30%	
	B	20%	
Mucerere	A	50%	Sow 50% of the acreage with *Nyayo* Sow 30% of the acreage with *Kat X 56* Sow 20% of the acreage with *Kayelo*
	N	30%	
	B	20%	
Seven-up	A	30%	Sow 30% of the acreage with *Nyayo* and *DK8031* Sow 50% of the acreage with *Kayelo* and *Sungura* Sow 20% of the acreage with *DH02* and *Katumbuka*
	N	50%	
	B	20%	

Pioneer P28, Duma 43, DH02, DK8031 and *Sungura* are maize see varieties and *Nyayo, Kat X 56, Kayelo,* and *Katumbuka* are bean seed varieties. All suitable for Kenyan drylands.

As an illustration, the Kanzoya farm group location, whose climatic services were derived from the above-normal prediction category, experienced average rainfall during this season. As a result of using seed kinds adapted for above-average precipitation, individual farmers in this location did not harvest much from their crops. However the Kanzoya group farm did not suffer a complete loss since farmers had divided the farm into three sections to accommodate the three probability groupings. Because of this, they received a bumper crop of the Duma 43 variety of maize from the group farm's 30% share.

The narrative from the focus group discussions concurred with the quantitative yield estimates, which are presented in **Figure 2**. In line with the communicated forecast, the Mucerere agricultural group experienced above-average rainfall. Participating farmers in this area received a bountiful harvest from their individual farms and from 50% of their collective farms. The Seven-up farm group's participating farmers, however, did not reap much from their individual farms because they had planted seed kinds for normal to above normal conditions in accordance with the stated prognosis, but the actual rainfall received was below average. Yet, their group farm did not completely lose out because 20% of the farm produced an excellent crop of DH02 maize, a seed variety suitable for below-average rains.

The group farm demonstration helped farmers understand the role of probability in forecasts and how they may use it to share the risk, despite the concerns surrounding forecast skills. Because of this, the farmers were able to maintain a healthy mix of caution and assurance throughout the season. According to the majority of farmers, all farmers in the county should have access to climate services because they will all reap similar benefits. Farmers cited the following requirements as necessary in order to make all farmers, train farmers to adopt climate services: Increase accessibility, educate farmers to comprehend and use the services, and transparently communicate forecast probability. These results suggest that improvements could be made to current forecast delivery practices as far as the format is concerned in Kenya.

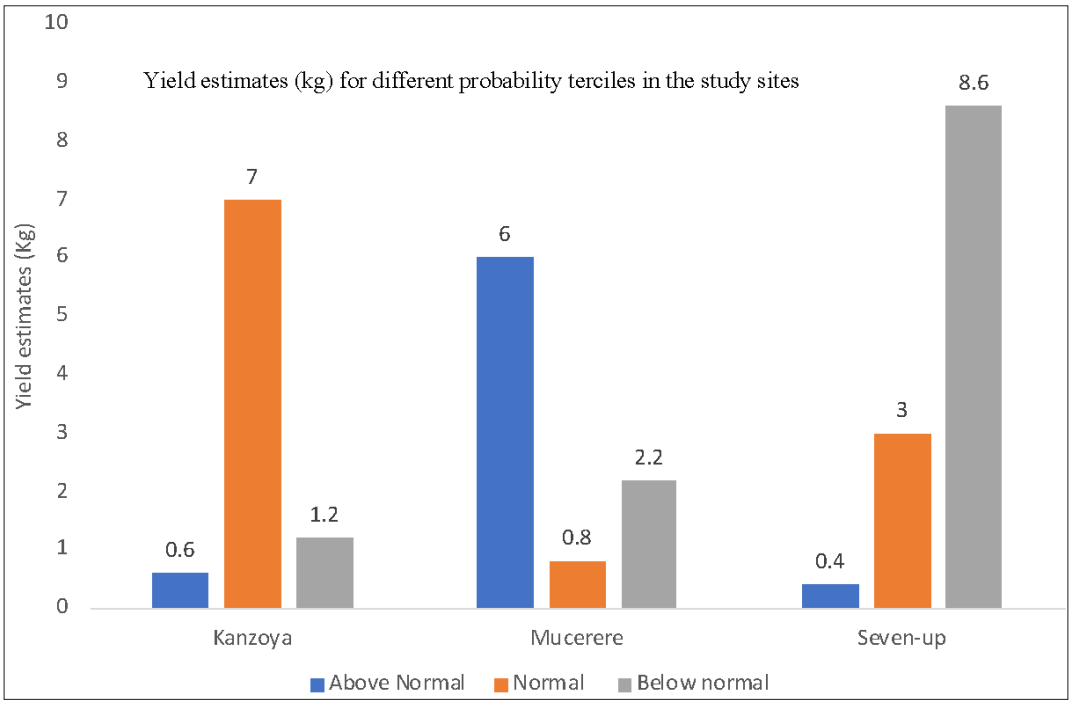

Figure 2. Yield estimates (kg) for the different cultivars indicated in Table 2 in different study sites.

4. Conclusions

This article set out to advance climate information services adoption by understanding how the interpretation of raw seasonal forecasts into probabilistic advisories can help bring a balance between caution and confidence among resource-poor smallholder farmers. To this end, the practical engagement of smallholder farmers provided insight into the importance of revealing forecast uncertainty and considering the same in the formulation of advisories (probabilistic advisories), which uphold the credibility of climate services and hence improved adoption.

Author Contributions

Mary Mwangi: Conceptualization, Investigation, Writing—First draft; **Evans Kituyi:** Visualization, Supervision; **Gilbert Ouma:** Visualization, Supervision.

Conflicts of Interest

The authors declare no conflicts of interest.

Acknowledgments

The main author gratefully acknowledges the co-authors: Dr. Evans Kituyi and Dr. Gilbert Ouma.

References

[1] Ouedraogo, I., Diouf, N.S., Ouédraogo, M., et al., 2018. Closing the gap between climate information producers and users: Assessment of needs and uptake in Senegal. Climate. 6(1), 13.

[2] Hansen, J., Bradley-Cook, J., Apotsos, A., et al., 2020. Making Climate Services Work for Africa's Farmers at Scale. Learning Agenda on Climate Services in Sub-Saharan Africa Spotlight Series 5. Washington DC: Climatelinks.

[3] de Andrade, F.M., Young, M.P., MacLeod, D., et al., 2021. Subseasonal precipitation prediction for Africa: Forecast evaluation and sources of predictability. Weather and Forecasting. 36(1), 265-284.

[4] Suarez, P., Patt, A.G., 2004. Cognition, caution, and credibility: The risks of climate forecast application. Risk Decision and Policy. 9(1), 75-89.

[5] Ziervogel, G., 2004. Targeting seasonal climate forecasts for integration into household level decisions: The case of smallholder farmers in Lesotho. Geographical Journal. 170(1), 6-21.

[6] Hansen, J.W., Vaughan, C., Kagabo, D.M., et al., 2019. Climate services can support African farmers' context-specific adaptation needs at scale. Frontiers in Sustainable Food Systems. 3, 21.

[7] Blundo-Canto, G., Andrieu, N., Adam, N.S., et al., 2021. Scaling weather and climate services for agriculture in Senegal: Evaluating systemic but overlooked effects. Climate Services. 22, 100216.

[8] Dinku, T., Block, P., Sharoff, J., et al., 2014. Bridging critical gaps in climate services and applications in Africa. Earth Perspectives. 1, 1-13.

[9] Tall, A., Coulibaly, J.Y., Diop, M., 2018. Do climate services make a difference? A review of evaluation methodologies and practices to assess the value of climate information services for farmers: Implications for Africa. Climate Services. 11, 1-12.

[10] Patt, A.G., 2009. Learning to crawl: How to use seasonal climate forecasts to build adaptive capacity. Adapting to climate change: Thresholds, values, governance. Cambridge University Press: Cambridge. pp. 79-95.

[11] O'Brien, K., Leichenko, R., Kelkar, U., et al., 2004. Mapping vulnerability to multiple stressors: Climate change and globalization in India. Global Environmental Change. 14, 303e313.

[12] Williams, D.S., Costa, M.M., Kovalevsky, D., et al., 2020. A method of assessing user capacities for effective climate services. Climate Services. 19, 100180.

[13] Dayamba, D.S., Ky-Dembele, C., Bayala, J., et al., 2018. Assessment of the use of Participatory Integrated Climate Services for Agriculture (PICSA) approach by farmers to manage climate

risk in Mali and Senegal. Climate Services. 12, 27-35.

[14] Ketiem, P., Makeni, P.M., Maranga, E.K., et al., 2017. Integration of climate change information into drylands crop production practices for enhanced food security: A case study of Lower Tana Basin in Kenya. African Journal of Agricultural Research. 12(20), 1763-1771.

[15] Owuor, B., Eriksen, S., Mauta, W., 2005. Adapting to climate change in a dryland mountain environment in Kenya. Mountain Research and Development. 25(4), 310-315.

[16] Gachathi, F.N., Eriksen, S., 2011. Gums and resins: The potential for supporting sustainable adaptation in Kenya's drylands. Climate and Development. 3(1), 59-70.

[17] Doblas-Reyes, F.J., García-Serrano, J., Lienert, F., et al., 2013. Seasonal climate predictability and forecasting: Status and prospects. Wiley Interdisciplinary Reviews: Climate Change. 4(4), 245-268.

[18] Klemm, T., McPherson, R.A., 2017. The development of seasonal climate forecasting for agricultural producers. Agricultural and Forest Meteorology. 232, 384-399.

[19] Mason, S.J., Stephenson, D.B., 2008. How do we know whether seasonal climate forecasts are any good? Seasonal climate: Forecasting and managing risk. Springer: Netherlands. pp. 259-289.

[20] Coelho, C.A., Costa, S.M., 2010. Challenges for integrating seasonal climate forecasts in user applications. Current Opinion in Environmental Sustainability. 2(5-6), 317-325.

[21] Weisheimer, A., Palmer, T.N., 2014. On the reliability of seasonal climate forecasts. Journal of the Royal Society Interface. 11(96), 20131162.

BILINGUAL PUBLISHING GROUP

Tel:+65 65881289

E-mail: contact@bilpublishing.com

Website:https://journals.bilpubgroup.com

2630-5119

02

9 772630 511232